

UCLA

UCLA Electronic Theses and Dissertations

Title

Investigation of background sources and search for neutrinoless double-beta decay in CUORE

Permalink

<https://escholarship.org/uc/item/8822k8wb>

Author

Alfonso, Krystal

Publication Date

2022

Peer reviewed|Thesis/dissertation

UNIVERSITY OF CALIFORNIA

Los Angeles

Investigation of background sources and
search for neutrinoless double-beta decay in CUORE

A dissertation submitted in partial satisfaction
of the requirements for the degree
Doctor of Philosophy in Physics

by

Krystal Rica Alfonso

2022

© Copyright by
Krystal Rica Alfonso
2022

ABSTRACT OF THE DISSERTATION

Investigation of background sources and
search for neutrinoless double-beta decay in CUORE

by

Krystal Rica Alfonso

Doctor of Philosophy in Physics

University of California, Los Angeles, 2022

Professor Huan Z. Huang, Chair

The Cryogenic Underground Observatory for Rare Events (CUORE) experiment at Gran Sasso National Laboratory in Italy searches for neutrinoless double-beta ($0\nu\beta\beta$) decay of ^{130}Te . The experimental sensitivity relies heavily on the background rate in the $0\nu\beta\beta$ decay region of interest (ROI). In CUORE, the dominant source of background in the ROI are degraded alpha particles originating from contaminated surfaces facing the detector.

This dissertation focuses on the work toward developing a detailed background model of the CUORE physics data in the $\sim 3\text{ MeV} - 7\text{ MeV}$ energy region, in order to identify and constrain the alpha background contribution to the ROI. A subset of the CUORE physics data collected between March 2019 and November 2020, corresponding to $433.3\text{ kg}\cdot\text{yr}$ exposure TeO_2 , was used to identify the background sources contributing to the alpha energy region. Multiplicity information, based on the number of CUORE crystals that detect energy depositions within a given space-time window, was used to distinguish bulk and surface contaminations. Monte Carlo simulations of the energy spectra of the identified background sources were used to constrain the characteristic depths of the surface contaminations used in the background model. This detailed study of the background alpha spectrum shape complements to previous background source investigations that used very coarse spectrum binning and allowed us to examine features of the detector energy response that depend on the depth of the surface contaminations.

The dissertation of Krystal Rica Alfonso is approved.

Thomas M. O'Donnell

Zhongbo Kang

Graciela B. Gelmini

Huan Z. Huang, Committee Chair

University of California, Los Angeles

2022

To my family

TABLE OF CONTENTS

1	Introduction	1
1.1	Neutrino oscillation	1
1.2	Double-beta decay	4
1.3	Sensitivity to neutrinoless double-beta decay	6
1.4	Neutrinoless double-beta decay experiments	6
2	CUORE Detector	9
2.1	Introduction	9
2.2	Crystal bolometric technique	11
2.3	Electronics	14
2.4	Cryostat	17
2.5	Inactive material selection and radiopurity controls	18
2.6	Radiation shielding	19
2.7	Working point measurement	20
3	CUORE data production	24
3.1	Introduction	24
3.2	Offline reprocessing	26
3.3	Online processing	33
3.4	CUORE data	36
4	Background model	41
4.1	Introduction	41
4.2	Alpha background spectra	43

4.3	Simulations	45
4.3.1	qshields	46
4.3.2	g4cuore	50
4.4	Bayesian model	56
4.4.1	Determination of contamination depths	59
4.5	Background fit of the alpha energy region	66
4.5.1	Fit results	68
4.5.2	Activities	68
4.5.3	Comparison with the CUORE-0 background model	70
4.5.4	Background index	71
4.6	Discussion	73
5	Conclusions	77
	Appendix A Tables	78
	Acronyms	79
	References	81

LIST OF FIGURES

1.1	Figure from [3]. On the left, $m_1 < m_3$ corresponds to <i>normal hierarchy</i> and on the right, $m_3 < m_1$ corresponds to <i>inverted hierarchy</i>	3
1.2	Conditions for double-beta decay. The lower parabola corresponds to even-even nuclei while the upper parabola corresponds to odd-odd nuclei. The filled circles on the lower parabola correspond to atomic numbers $Z \pm 2$; they cannot single beta-decay to the isotopes on the upper parabola because of their higher nuclear mass, so instead double-beta decay occurs to the element corresponding to atomic number Z	4
1.3	Feynman diagrams of $\beta\beta$ decay.	5
1.4	Q-values and natural isotopic abundances of double-beta decay isotopes.	7
1.5	Effective Majorana mass ($m_{\beta\beta}$) as a function of the lightest neutrino mass based on neutrino oscillation measurements. The horizontal bands correspond to the current leading limits from neutrinoless double-beta decay experiments.	8
2.1	Detailed renderings of the CUORE detector.	10
2.2	CUORE cryostat.	11
2.3	Evolution of TeO ₂ bolometric experiments.	12
2.4	Left: Bolometer schematic where T_o is the temperature of the heat sink, G is the thermal conductance of the thermal link between the heat sink and absorber, C is the heat capacity of the absorber, and R is the resistance of the sensor. Right: Signal measured by sensor labeled with thermal parameters where τ corresponds to the decay time constant of the thermal signal.	12
2.5	CUORE bolometer. Bolometer component labels are on the left and corresponding CUORE bolometer part labels are on the right.	13

2.6	Schematic of the CUORE electronics. The electronics are stored above the cryostat at room temperature. A Faraday cage houses the electronics boards interfacing with the resistors on the crystal.	15
2.7	Photo of external shielding.	20
2.8	Schematic of the NTD biasing circuit.	21
2.9	Figure from [26]. Example of a load curve.	22
2.10	Figure from [26]. Characteristic curves for working point determination of one bolometer.	23
3.1	Signal event example. The red marker indicates the trigger position.	25
3.2	An example of an average pulse in the time domain.	27
3.3	An example of an average noise power spectrum in the frequency domain.	28
3.4	HeaterTGS baseline stabilization example using two consecutive runs. The red line corresponds to the linear fit function over the range.	30
3.5	HeaterTGS stabilized amplitude example using two consecutive runs.	31
3.6	CalibrationTGS baseline stabilization example. The red line corresponds to the quadratic fit function over the range.	32
3.7	Comparison of blinded and unblinded spectrum in the affected energy range.	33
3.8	Schematic of internal DCS source string locations.	34
3.9	Schematic of external DCS source string locations. The red dots indicate the source string locations.	35

3.10	Figure from [26]. CUORE resistance stability at 11.8 mK. Each element in the plot corresponds to a single working point measurement. The data corresponds to the distribution of the channel-dependent relative variation of the R_{NTD} values defined as $(R_{NTD} - R_{NTD}^{ref})/R_{NTD}^{ref}$ where R_{NTD}^{ref} was chosen from a measurement taken in August 2019. The circle corresponds to the mean of the distribution and the horizontal line corresponds to the median. The solid box around the mean indicates the width of 50% of the distribution of the data. The dashed lines extending vertically from the boxes indicate the width of 95% of the data distribution.	36
3.11	CUORE exposure. Extended flat regions indicate periods of system maintenance and upgrades.	37
3.12	CUORE physics spectrum from DS3606 – DS3615 with corresponding calibration spectrum normalized to the 2615 keV gamma line.	39
3.13	Result of using cuts on the CUORE physics spectrum corresponding to DS3601 – DS3615. Base Cuts are based on the analysis sequences and only pass events that contain one signal pulse, AC (anti-coincidence) corresponds to the $0\nu\beta\beta$ decay multiplicity cut, and PSD corresponds to pulse shape discrimination cuts. The vertical line labeled $Q_{\beta\beta}$ corresponds to the Q-value of ^{130}Te double-beta decay.	40

4.1	Schematic of alpha decays that contribute to the alpha energy region. Location of alpha decay is denoted by the alpha particle, alpha energy deposition location is denoted by the solid, black arrow, and nuclear recoil energy deposition location is denoted by the dashed, grey arrow. 1 corresponds to crystal bulk contamination: both the alpha particle and recoil nucleus deposit their energies in the same crystal resulting in an M1 event. 2 corresponds to crystal surface contamination: the recoil nucleus (alpha particle) deposits its energy in the source crystal and the alpha particle (recoil nucleus) escapes and deposits its energy in a different crystal resulting in a pair of M2 events and a corresponding M2Sum event. 3 corresponds to copper surface contamination: the nuclear recoil energy is not detected as it is deposited in the copper frame and the alpha particle escapes and deposits its energy in a crystal resulting in an M1 event.	44
4.2	Simulations of the possible detected alpha decay contaminations and their contributions to the different multiplicity spectra. a) corresponds to the M1 spectrum. b) corresponds to the M2 spectrum. c) corresponds to the M2Sum spectrum. . .	45
4.3	Schematic of CUORE's 19 towers reflecting the different crystal geometries. The relative column positions are denoted by the solid black lines representing the tower corners from a top-down perspective. Five crystal geometries are highlighted: inner crystals, lateral crystals, top crystals, bottom crystals, and top/bottom edge crystals. The inner crystals are mainly exposed to the other crystals and the tower structures. In addition to the detector structure, the lateral crystals are exposed to the 10 mK copper tiles; the top crystals are exposed to the top copper plate; the bottom crystals are exposed to the bottom copper plate; and the edge crystals are exposed to the 10 mK copper tiles and the top/bottom copper plate.	46
4.4	Comparison of alpha background spectra from different crystal geometries. . . .	47
4.5	Comparison of gamma background spectra from different crystal geometries. . .	47
4.6	M1 spectrum. The background source contributions to the indexed peaks are in Table 4.1.	48

4.7	M2 spectrum. The background source contributions to the indexed peaks are in Table 4.2.	50
4.8	M2Sum spectrum. The background source contributions to the indexed peaks are in Table 4.3.	52
4.9	Figure from [35]. Radioactive decay chains contributing to the background in the alpha region.	54
4.10	Simulated bulk contamination in the TeO ₂ crystals. The top figures corresponds to the different 2D distributions of the source positions in the qshields coordinate system; their projections along their horizontal axes are shown directly below. For uniform source distributions, the number of source points generated are proportional to the material thickness.	55
4.11	Simulated surface contaminations on the copper tower structure. The top figures corresponds to 2D distributions of the source positions in the qshields coordinate system; their projections along their horizontal axes are shown directly below. The figures on the left correspond to a characteristic depth of 100 μm and the figures on the right correspond to a characteristic depth of 1 μm . For shallower characteristic depths, more source points are generated closer to the surface. . .	56
4.12	Left: Wire-frame, top-down view of qshields geometry. Right: Wire-frame, high-angle view of qshields geometry.	57
4.13	The effect of quenching on ²²⁸ Ra simulations. a) corresponds to the M2 spectrum, b) corresponds to the M2Sum spectrum, and c) corresponds to the M1 spectrum. The red spectrum corresponds to no applied quenching and the blue spectrum corresponds to the quenching applied in this analysis.	59

4.14	Comparison of ^{238}U simulations with different recoil quenching applied. a) M2 spectrum with recoil quenching value of 0.94. b) M2 spectrum with recoil quenching value of 0.97. The lower quenching value suppresses the contribution to the higher energy alpha peak because the quenched recoil energy is below the 70 keV energy threshold. The higher quenching value recovers M2 events in the high energy alpha peak.	60
4.15	Resolution functions applied to surface and bulk contaminations in g4cuore. The data points come from fitting the peaks in the background energy spectra to a Gaussian function. Peaks corresponding to bulk contaminations generally have better energy resolution, so a different resolution function was applied to simulated bulk contamination events compared to surface events.	62
4.16	^{190}Pt contamination. a) corresponds to the M1 spectrum, b) corresponds to the M2 spectrum, and c) corresponds to the M2Sum spectrum.	63
4.17	^{232}Th contaminations. a) corresponds to the M1 spectrum, b) corresponds to the M2 spectrum, and c) corresponds to the M2Sum spectrum.	64
4.18	^{238}U contaminations. a) corresponds to the M1 spectrum, b) corresponds to the M2 spectrum, and c) corresponds to the M2Sum spectrum.	64
4.19	^{228}Ra and ^{226}Ra contaminations. a) corresponds to the M1 spectrum, b) corresponds to the M2 spectrum, and c) corresponds to the M2Sum spectrum.	65
4.20	^{230}Th and ^{210}Pb contaminations. a) corresponds to the M1 spectrum, b) corresponds to the M2 spectrum, and c) corresponds to the M2Sum spectrum.	67
4.21	Top: M1 reconstruction compared with data. Bottom: Ratio of data events and reconstructed events by bin. Gaps in data points correspond to energy regions omitted from the fit.	69
4.22	Top: M2 reconstruction compared with data. Bottom: Ratio of data events and reconstructed events by bin. Gaps in data points correspond to energy regions omitted from the fit.	70

4.23	Background contribution from all simulated alpha contaminations in the ROI. Only prominent sources are listed in the legend.	74
4.24	Background contribution from all simulated alpha contaminations in the CUPID ROI. Only prominent sources are listed in the legend.	75

LIST OF TABLES

3.1	Unblinded dataset summary. Dates may overlap due to shared calibration runs between datasets. ^{232}Th hybrid corresponds to internal and external calibration source strings. External hybrid corresponds to different sources used between initial and final calibration.	38
4.1	Source of characteristic peaks in the M1 spectrum [34].	49
4.2	Source of characteristic peaks in the M2 spectrum [34].	51
4.3	Source of characteristic peaks in the M2Sum spectrum [34].	53
4.4	Mass, volume, and surface area of simulated volume elements near or comprising the detector.	58
4.5	Implemented quenching factors.	61
4.6	Surface source activities.	71
4.7	Bulk source activities.	72
4.8	Surface contaminations in the TeO_2 crystals and Cu support structure based on CUORE-0 background model [38].	72
4.9	Bulk contaminations in the TeO_2 crystals based on CUORE-0 background model [38].	73
A.1	Dataset exposures after analysis cuts.	78

ACKNOWLEDGMENTS

I would like to thank my advisor, Professor Huan Huang, for his patience, understanding, and unwavering support. I don't know how I could possibly thank you enough for everything, but thank you for seeing me through to the end.

I would like to thank Professor Thomas (Tommy) O'Donnell for reminding me that making mistakes [and learning from them] is how we become experts. Thank you for your mentorship and for being a constant source of encouragement.

I would also like to thank Brian Zhu for being markedly unreserved and for always telling me what I need to hear.

I would like to acknowledge DEAR ISABEL. Drafting this dissertation as if I were writing one of our secondary school letters has been effective and therapeutic. Thank you Isabel for always telling me what I want to hear.

Last, but not least, I would like to thank my husband, Tom Lue, for being everything I didn't know I needed on this journey. Thank you for your persistence in sharing this unconventional life.

VITA

- 2008 Bachelor of Arts in Physics
University of California, Berkeley.
- 2017 Master of Science in Physics
University of California, Los Angeles.
- 2018–2019 Teaching Assistant
Department of Physics and Astronomy
University of California, Los Angeles.
- 2014–present Graduate Student Researcher
Department of Physics and Astronomy
University of California, Los Angeles.

PUBLICATIONS

- D. Q. Adams *et al.* (CUORE Collaboration). “*CUORE opens the door to tonne-scale cryogenics experiments,*” *Progress in Particle and Nuclear Physics* **122**, 103902 (2022).
- K. Alfonso *et al.* “*An automated system to define the optimal operating settings of cryogenic calorimeters,*” *Nucl. Instrum. Methods Phys. Res. A* **1008**, 165451 (2021).
- D. Q. Adams *et al.* (CUORE Collaboration). “*Measurement of the $2\nu\beta\beta$ Decay Half-Life of ^{130}Te with CUORE,*” *Phys. Rev. Lett.* **126**, 171801 (2021).
- D. Q. Adams *et al.* (CUORE Collaboration). “*Improved Limit on Neutrinoless Double-Beta Decay in Te-130 with CUORE,*” *Phys. Rev. Lett.* **124**, 122501 (2020).

C. Alduino *et al.* (CUORE Collaboration). “*Study of rare nuclear processes with CUORE,*” International Journal of Modern Physics A **33**, No. 09 (2018).

C. Alduino *et al.* (CUORE Collaboration). “*First Results from CUORE: A Search for Lepton Number Violation via $0\nu\beta\beta$ Decay of Te-130,*” Phys. Rev. Lett. **120**, 132501 (2018).

K. Alfonso *et al.* “*A high precision pulse generation and stabilization system for bolometric experiments,*” JINST **13**, P02029 (2018).

C. Alduino *et al.* (CUORE Collaboration). “*The projected background for the CUORE experiment,*” European Physical Journal C **77**, 543 (2017).

C. Alduino *et al.* (CUORE Collaboration). “*CUORE Sensitivity to $0\nu\beta\beta$ Decay,*” European Physical Journal C **77**, 532 (2017).

C. Alduino *et al.* (CUORE Collaboration). “*Measurement of the Two-Neutrino Double Beta Decay Half-life of Te-130 with the CUORE-0 Experiment,*” European Physical Journal C **77**, 13 (2017).

C. Alduino *et al.* (CUORE Collaboration). “*CUORE-0 detector: design, construction and operation,*” Journal of Instrumentation **11**, P07009 (2016).

C. Alduino *et al.* (CUORE Collaboration). “*Analysis Techniques for the Evaluation of the Neutrinoless Double- β Decay Lifetime in Te-130 with CUORE-0,*” Physical Review C **93**, 045503 (2016).

K. Alfonso *et al.* (CUORE Collaboration). “*Search for Neutrinoless Double-Beta Decay of ^{130}Te with CUORE-0,*” Phys. Rev. Lett. **115**, 102502 (2015).

CHAPTER 1

Introduction

1.1 Neutrino oscillation

Neutrino oscillation measurements have provided evidence of a non-vanishing neutrino rest mass. Since the current formulation of the Standard Model does not include massive neutrinos, the result of these measurements has exposed a gap in our foundational understanding of elementary particles. Consequently, the massive neutrino has become a beacon for transformative discoveries.

Neutrino oscillation occurs because the neutrino mass eigenstates, ν_i where $i = 1, 2, 3$, are not the same as their flavor eigenstates, ν_α where α denotes the lepton (e, μ, τ) with which the neutrino is created. Instead, the neutrino flavor eigenstates are related to the neutrino mass eigenstates by the Pontecorvo-Maki-Nakagawa-Sakata (PMNS) mixing matrix, U :

$$|\nu_\alpha\rangle = \sum_i U_{\alpha i}^* |\nu_i\rangle . \quad (1.1)$$

The PMNS matrix can be parameterized by 3 mixing angles ($\theta_{12}, \theta_{23}, \theta_{13}$), 1 CP-violating phase factor (δ), and 2 CP-violating Majorana phase factors (ϕ_1, ϕ_2):

$$U = \begin{pmatrix} 1 & 0 & 0 \\ 0 & c_{23} & s_{23} \\ 0 & -s_{23} & c_{23} \end{pmatrix} \cdot \begin{pmatrix} c_{13} & 0 & s_{13}e^{-i\delta} \\ 0 & 1 & 0 \\ -s_{13}e^{i\delta} & 0 & c_{13} \end{pmatrix} \cdot \begin{pmatrix} c_{21} & s_{12} & 0 \\ -s_{12} & c_{12} & 0 \\ 0 & 0 & 1 \end{pmatrix} \cdot \begin{pmatrix} e^{i\phi_1} & 0 & 0 \\ 0 & e^{i\phi_2} & 0 \\ 0 & 0 & 1 \end{pmatrix} , \quad (1.2)$$

where $s_{ij} = \sin \theta_{ij}$ and $c_{ij} = \cos \theta_{ij}$ ($i, j = 1, 2, 3$) [1]. The Majorana phase factors exist in the case that neutrinos are their own antiparticles, in which case they would be described as *Majorana particles* or Majorana in particle nature.

The phenomenology of neutrino oscillation can be illustrated considering only 2 neutrino flavors:

$$\begin{pmatrix} \nu_e \\ \nu_\mu \end{pmatrix} = \begin{pmatrix} \cos\theta & \sin\theta \\ -\sin\theta & \cos\theta \end{pmatrix} \begin{pmatrix} \nu_1 \\ \nu_2 \end{pmatrix}. \quad (1.3)$$

If at $t = 0$, the initial electron neutrino eigenstate and mass eigenstates are:

$$|\nu_e(0)\rangle = \cos\theta |\nu_1(0)\rangle + \sin\theta |\nu_2(0)\rangle, \quad (1.4)$$

$$|\nu_1(0)\rangle = \cos\theta |\nu_e(0)\rangle - \sin\theta |\nu_\mu(0)\rangle, \quad (1.5)$$

$$|\nu_2(0)\rangle = \sin\theta |\nu_e(0)\rangle + \cos\theta |\nu_\mu(0)\rangle, \quad (1.6)$$

at a later time, t , the electron neutrino eigenstate as a function of energy E_i is:

$$\begin{aligned} |\nu_e(t)\rangle &= \cos\theta e^{-iE_1 t} |\nu_1(0)\rangle + \sin\theta e^{-iE_2 t} |\nu_2(0)\rangle \\ &= (\cos^2\theta e^{-iE_1 t} + \sin^2\theta e^{-iE_2 t}) |\nu_e(0)\rangle + \sin\theta \cos\theta (e^{-iE_2 t} - e^{-iE_1 t}) |\nu_\mu(0)\rangle, \end{aligned} \quad (1.7)$$

where the energy is a function of momentum p and mass m_i : $E_i = \sqrt{p^2 + m_i^2} \simeq p \left(1 + \frac{m_i^2}{2p^2}\right)$, then the survival probability of the electron neutrino after traveling a distance L is:

$$\begin{aligned} P(\nu_e \rightarrow \nu_e) &= |\langle \nu_e(0) | \nu_e(t = L/c) \rangle|^2 \\ &= 1 - \sin^2(2\theta) \sin^2\left(\frac{\Delta m^2 L}{4E}\right), \end{aligned} \quad (1.8)$$

with $p \gg m$ and where $\Delta m^2 = m_2^2 - m_1^2$. From Equation 1.8, neutrino oscillation experiments are sensitive to the mixing angles and the difference in mass squared (Δm^2). Because of the nature of Δm^2 , these measurements cannot determine the *absolute mass scale*, nor mass hierarchy (sign of Δm^2), of the neutrino.

Using the 3-neutrino flavor formulation, neutrino oscillation experiments have measured most of the parameters of the PMNS matrix. Figure 1.1 illustrates the information obtained from the experiments: the mass-squared differences from solar and atmospheric neutrino oscillation measurements and the relative mixing of neutrino flavor eigenstates in each mass eigenstate. The left side corresponds to the case where $m_1 < m_3$ (normal hierarchy) and the right side corresponds to the case where $m_3 < m_1$ (inverted hierarchy). In both cases, the lightest mass is relative to an unknown absolute mass scale. Currently, long-baseline

and atmospheric neutrino oscillation experiments are including matter effects in their measurements to probe the neutrino mass hierarchy, while cosmological surveys of the CMB and large scale structure (LSS) and direct kinematic searches are constraining the absolute mass scale of the neutrino. From cosmological data, the Planck satellite constrains the sum of the three neutrino masses to $\Sigma m_i < 0.12 \text{ eV}$ [2]. From their measurement of the beta decay spectrum endpoint of tritium, KATRIN places an upper limit on the effective electron antineutrino mass of $m_\nu < 0.8 \text{ eV}$. The subsequent sections discuss *neutrinoless double-beta* ($0\nu\beta\beta$) decay, a process that may be used to probe not only these unknown characteristics of the neutrino, but also its particle nature.

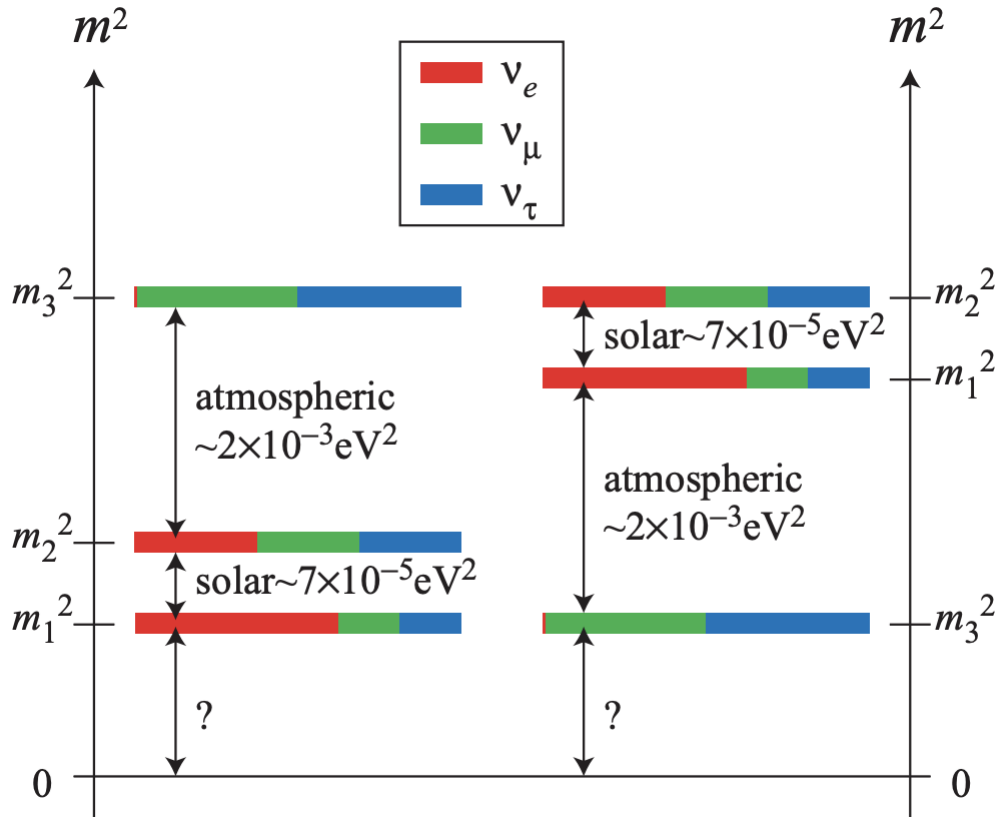


Figure 1.1: Figure from [3]. On the left, $m_1 < m_3$ corresponds to *normal hierarchy* and on the right, $m_3 < m_1$ corresponds to *inverted hierarchy*.

1.2 Double-beta decay

Double-beta decay is a rare process that can only occur in even-even nuclei when it is energetically favored in comparison to competing decay modes (see Figure 1.2). Two-neutrino double-beta ($2\nu\beta\beta$) decay, first proposed in 1935 by Maria Goeppert-Mayer, corresponds to the simultaneous decay of two neutrons in a nucleus to two protons with the emission of two electrons and two electron antineutrinos [4]:

$$(A, Z) \rightarrow (A, Z + 2) + 2e^- + 2\bar{\nu}_e . \quad (1.9)$$

The process has been observed and is allowed within the Standard Model (see Figure 1.3a), but as a second-order weak process, it is extremely rare; the half-lives for these decays exceed 10^{18} years [5].

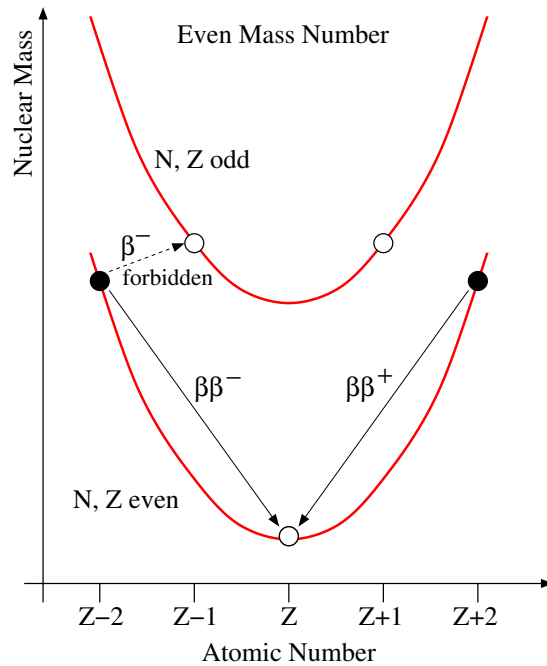


Figure 1.2: Conditions for double-beta decay. The lower parabola corresponds to even-even nuclei while the upper parabola corresponds to odd-odd nuclei. The filled circles on the lower parabola correspond to atomic numbers $Z \pm 2$; they cannot single beta-decay to the isotopes on the upper parabola because of their higher nuclear mass, so instead double-beta decay occurs to the element corresponding to atomic number Z .

In 1937, Ettore Majorana proposed the existence of fundamental, spin-1/2 particles whose particle and antiparticle are the same. Applying the nature of Majorana's particle to the antineutrinos in Goeppert-Mayer's $2\nu\beta\beta$ decay process, Wendell H. Furry proposed neutrinoless double-beta ($0\nu\beta\beta$) decay in 1939 [6]. Neutrinoless double-beta decay corresponds to the simultaneous decay of two neutrons in a nucleus to two protons with the emission of two electrons:

$$(A, Z) \rightarrow (A, Z + 2) + 2e^- . \quad (1.10)$$

If observed, this process would not only confirm the Majorana nature of the neutrino, but also prove lepton number is not conserved.

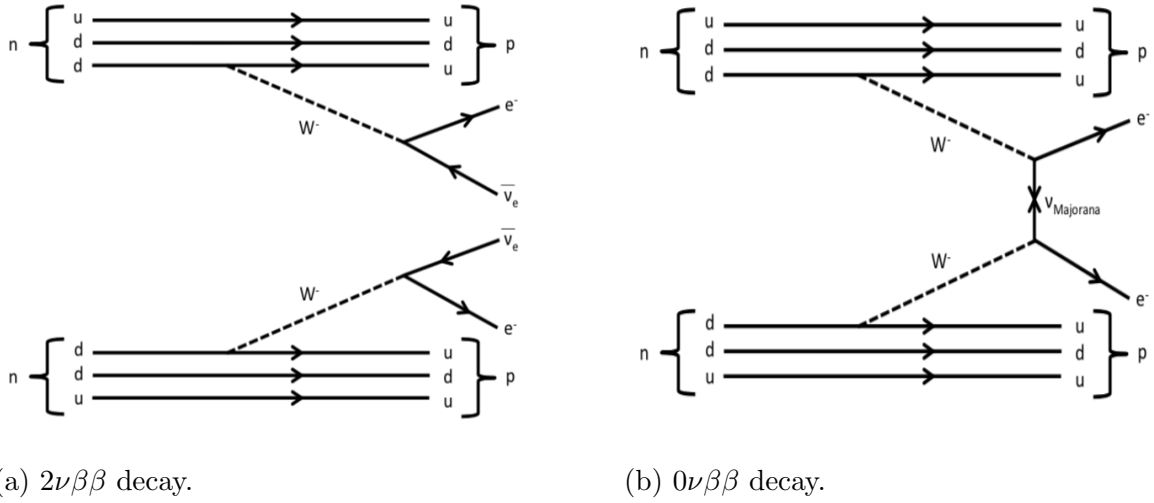


Figure 1.3: Feynman diagrams of $\beta\beta$ decay.

Assuming the process is mediated by light Majorana neutrino exchange, as depicted in Figure 1.3b, neutrinoless double-beta decay is also sensitive to the absolute mass scale and mass hierarchy of the neutrino since its half-life, $T_{1/2}^{0\nu}$ is related to the *effective Majorana mass*, $m_{\beta\beta}$:

$$\frac{1}{T_{1/2}^{0\nu}} = G^{0\nu} |M^{0\nu}|^2 |\langle m_{\beta\beta} \rangle|^2 , \quad (1.11)$$

where $G^{0\nu}$ is the phase space factor derived from kinematics, $M^{0\nu}$ is the nuclear matrix element derived from nuclear structure, and $m_{\beta\beta}$ is:

$$|\langle m_{\beta\beta} \rangle| = \left| \sum_{i=1}^3 U_{ei}^2 m_i \right| , \quad (1.12)$$

where U_{ei} are the PMNS mixing matrix elements and \bar{m}_i are the mass eigenvalues. Figure 1.5 shows the range of $m_{\beta\beta}$ as a function of possible values of the lightest neutrino mass ($m_{lightest}$) within the current experimental constraints of relevant parameters.

1.3 Sensitivity to neutrinoless double-beta decay

Observing neutrinoless double-beta decay and measuring its half-life would address some of the questions unanswered by neutrino oscillation. For a given $\beta\beta$ -emitter, experimental evidence of a nonzero $0\nu\beta\beta$ decay branching ratio would manifest as a monochromatic peak at the Q-value of its decay ($Q_{\beta\beta}$). From Equation 1.11, the absolute mass scale of the neutrino could be derived from the neutrinoless double-beta decay rate, which would correspond to the $Q_{\beta\beta}$ peak count rate. From this type of measurement, the experimental *sensitivity* to the neutrinoless double-beta decay half-life is parametrized as:

$$\text{Sensitivity} \propto a_I \sqrt{\frac{Mt}{b\Delta E}}, \quad (1.13)$$

where a_I is the isotopic abundance of the $\beta\beta$ -emitter, M is the total active mass of the detector, t is the livetime, b is the background rate per unit energy, per unit detector mass, and ΔE is the energy width of the region of interest (ROI), which is determined by the detector energy resolution at $Q_{\beta\beta}$.

From Equation 1.13, the experimental sensitivity can be optimized by exposing a large mass of $\beta\beta$ -emitter to a detector with high energy resolution and that is able to maintain stable, long-term operation. In this optimized scenario, the high energy resolution helps to reduce the background from $2\nu\beta\beta$ decay, which contributes to events near its endpoint energy, $Q_{\beta\beta}$. Background contributions to the ROI from environmental sources would need to be addressed with shielding, radiopurity controls, and cleaning procedures.

1.4 Neutrinoless double-beta decay experiments

The current neutrinoless double-beta decay experiments use a variety of double-beta decay sources, detector technology, and background mitigation techniques. Figure 1.4 illustrates

that there is no ideal choice of $\beta\beta$ -emitter since both a high Q-value, above most natural gamma-ray backgrounds, and a high isotopic abundance is desirable when optimizing sensitivity. The decision is further complicated when the $\beta\beta$ -emitter also acts as the detector material since its detector properties lead to additional considerations.

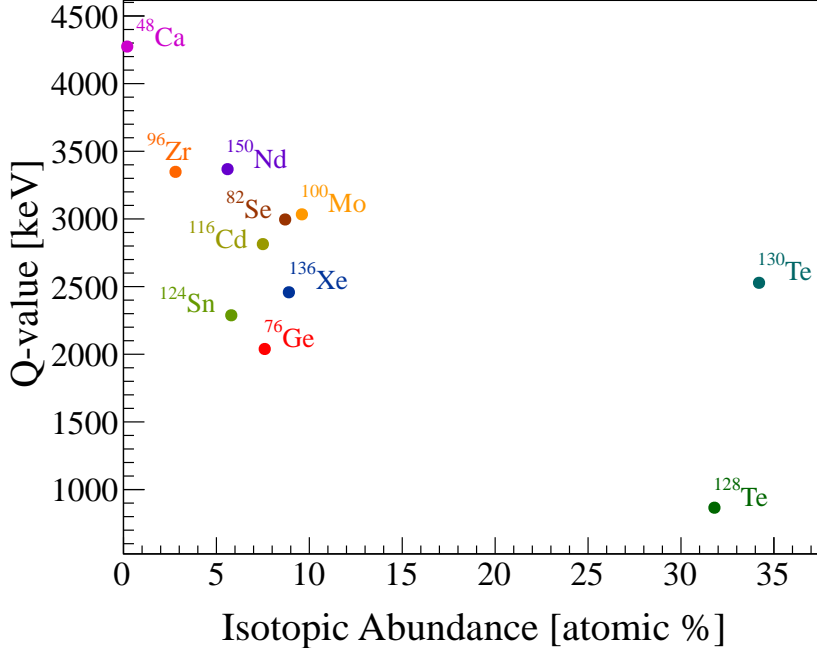


Figure 1.4: Q-values and natural isotopic abundances of double-beta decay isotopes.

Figure 1.5, discussed in Section 1.2, compares the leading $m_{\beta\beta}$ limits obtained from the CUORE (Te), GERDA (Ge), and KamLAND-Zen (Xe) experiments. The $m_{\beta\beta}$ limits obtained from CUPID-Mo (Mo) and CUPID-0 (Se), research and development experiments related to CUORE, are also shown. The range of effective Majorana mass from each measurement comes from the range of nuclear matrix elements. In general, difficulties in calculating the matrix elements impacts the ability to make inferences on the absolute mass scale. Each of these experiments uses a different approach in their search for neutrinoless double-beta decay. KamLAND-Zen, located in the Kamioka Mine in Gifu, Japan, uses enriched Xe-loaded liquid scintillator (Xe-LS) and photomultiplier tubes (PMTs) to search for $0\nu\beta\beta$ decay in ^{136}Xe . Additional liquid scintillator (LS) surrounding the Xe-LS is used as an active shield. Its experimental sensitivity benefits from its large active mass afforded by the scalability of

liquid scintillators, but its energy resolution ($\sigma \sim 7.3\%/\sqrt{\text{Energy (MeV)}}$) is also sacrificed as a result [7]. GERDA, located at Gran Sasso National Laboratory (LNGS) in L'Aquila, Italy, uses enriched high purity germanium (HPGe) detectors to search for $0\nu\beta\beta$ decay in ^{76}Ge . The HPGe detectors are suspended in a liquid argon (LAr) cryostat, which is surrounded by a water cerenkov detector that acts as an active shield. Although this type of detector is more difficult to scale, GERDA benefits from its energy resolution (2.6 keV FWHM at $Q_{\beta\beta}$) and pulse shape discrimination properties, which helped to lower its background index to 5.2×10^{-4} counts/(keV·kg·yr) [8]. CUORE searches for $0\nu\beta\beta$ decay in ^{130}Te and will be discussed in the remaining chapters of this thesis.

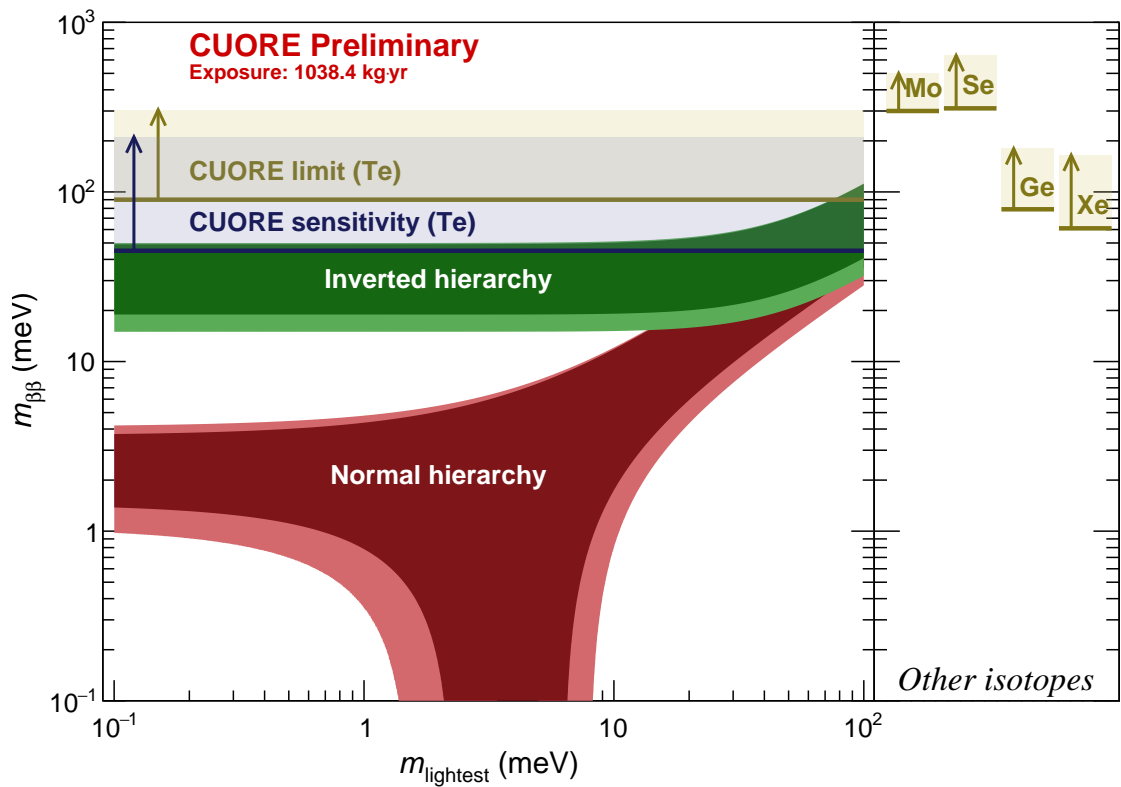


Figure 1.5: Effective Majorana mass ($m_{\beta\beta}$) as a function of the lightest neutrino mass based on neutrino oscillation measurements. The horizontal bands correspond to the current leading limits from neutrinoless double-beta decay experiments.

CHAPTER 2

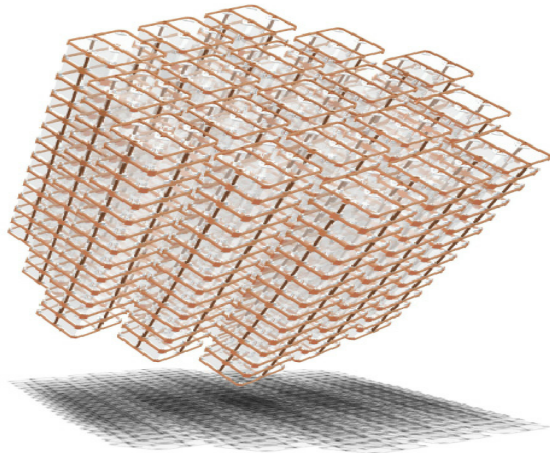
CUORE Detector

2.1 Introduction

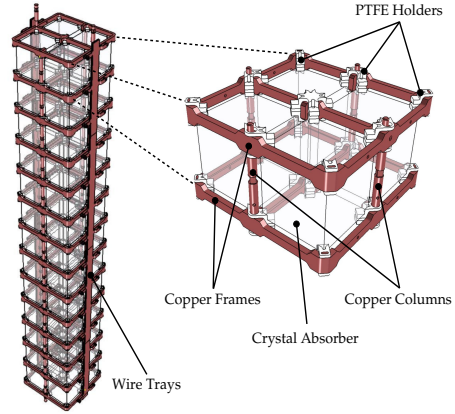
The Cryogenic Underground Observatory for Rare Events (CUORE) experiment is primarily designed to search for neutrinoless double-beta ($0\nu\beta\beta$) decay of ^{130}Te using low-temperature calorimetric detectors. The detection system is based on the *bolometric* technique, which uses a dielectric and diamagnetic crystal, at sufficiently low heat capacity, to measure a temperature increase in response to a small energy deposition. Since this technique imposes few requirements on the crystal material, CUORE was able to select the detector material, TeO_2 , based on the choice of $\beta\beta$ -emitter. CUORE chose ^{130}Te because its $Q_{\beta\beta}$ (2527.518 keV) is above most natural gamma-ray background and its natural isotopic abundance (34.167%) alleviates the need for costly enrichment procedures [9][10]. Operating at ~ 10 mK, the characteristic energy resolution of $Q_{\beta\beta}$ is (7.8 ± 0.5) keV [11].

The CUORE detector consists of 988 natural TeO_2 crystals arranged in a hexagonal array of 19 towers, as shown in Figure 2.1a. Each tower consists of a copper structure that supports 52 crystals arranged across 13 floors, with each floor consisting of a 2×2 crystal array as shown in Figure 2.1b. Polytetrafluoroethylene (PTFE) holders are placed between the corners of each $5 \times 5 \times 5$ cm³ crystal and the copper support structure. The detector provides a total ^{130}Te source mass of ~ 206 kg.

The CUORE detector is suspended inside the CUORE cryostat as shown in Figure 2.2. The cryostat consists of six nested copper vessels and 3 cooling systems that decrease the temperature of the innermost vessel, where the detector is held, to ~ 10 mK. The copper vessels act as thermal shields that divide the cryostat into different temperature stages: 300 K,



(a) Rendering of the CUORE detector.



(b) Figure from [12]. Rendering of a single CUORE tower and floor.

Figure 2.1: Detailed renderings of the CUORE detector.

40 K, 4 K, 600 mK, 50 mK, and 10 mK. Below room temperature, the vessel temperatures are maintained by thermal contact of their top plates with different stages of the cooling systems. The cryostat is also divided into two vacuum-tight chambers; the 300 K vessel encloses the *Outer Vacuum Chamber* (OVC) and the 4 K vessel encloses the *Inner Vacuum Chamber* (IVC). The OVC and IVC facilitate the use of helium exchange gas to thermalize the inner chambers during the initial phases of the cool down.

Figure 2.3 shows the evolution of TeO_2 bolometric experiments. The CUORE experiment leverages the research and development work of its predecessors, MiDBD (Milano Double Beta Decay), the pioneer of the bolometric technique for $0\nu\beta\beta$ decay searches, and Cuoricino. Both experiments shaped the final material selection and design considerations for CUORE. Studies of the Cuoricino background led CUORE to implement aggressive cleaning procedures and strict radiopurity controls on the detector and cryostat materials. As with its predecessors, CUORE is located at Gran Sasso National Laboratory (LNGS), an underground facility in L'Aquila, Italy. The location provides ~ 3600 m.w.e. overburden to reduce background from cosmic rays. In Hall A of LNGS, where CUORE is located, the muon flux is $3 \times 10^{-8} \mu/(\text{s}\cdot\text{cm}^2)$ and the neutron flux is $4 \times 10^{-6} \text{ n}/(\text{s}\cdot\text{cm}^2)$ [13][14]. The environmental background external to the CUORE detector is addressed with radiation shielding inside and

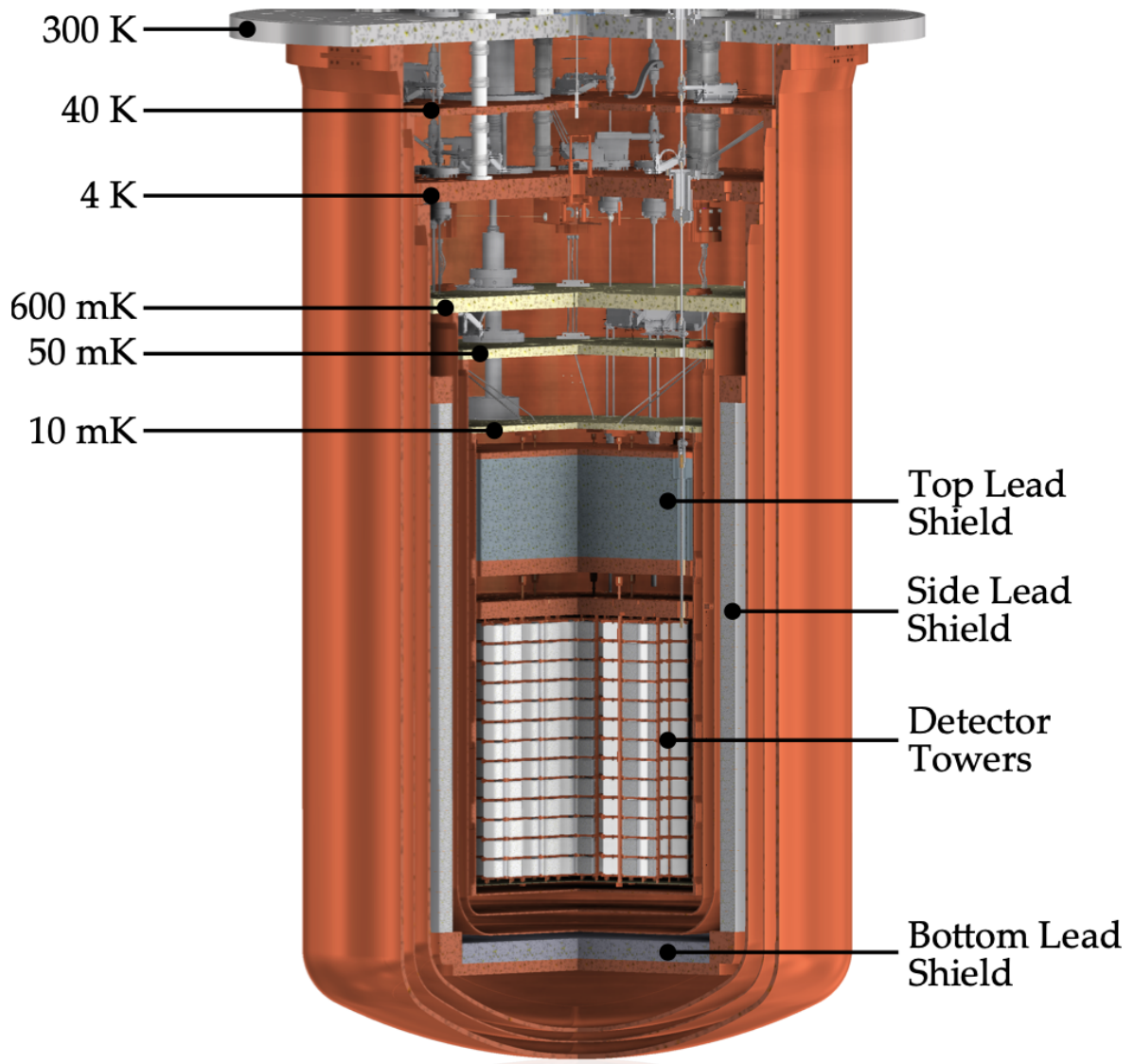


Figure 2.2: CUORE cryostat.

outside the CUORE cryostat. After one tonne-year exposure, CUORE measures an average background index of $(1.49 \pm 0.04) \times 10^{-2}$ counts/(keV·kg·yr) in the ROI [11].

2.2 Crystal bolometric technique

The purpose of a bolometer is to measure the particle-induced energy deposition based on the observed temperature change. As shown in Figure 2.4, a bolometer consists of an *absorber*

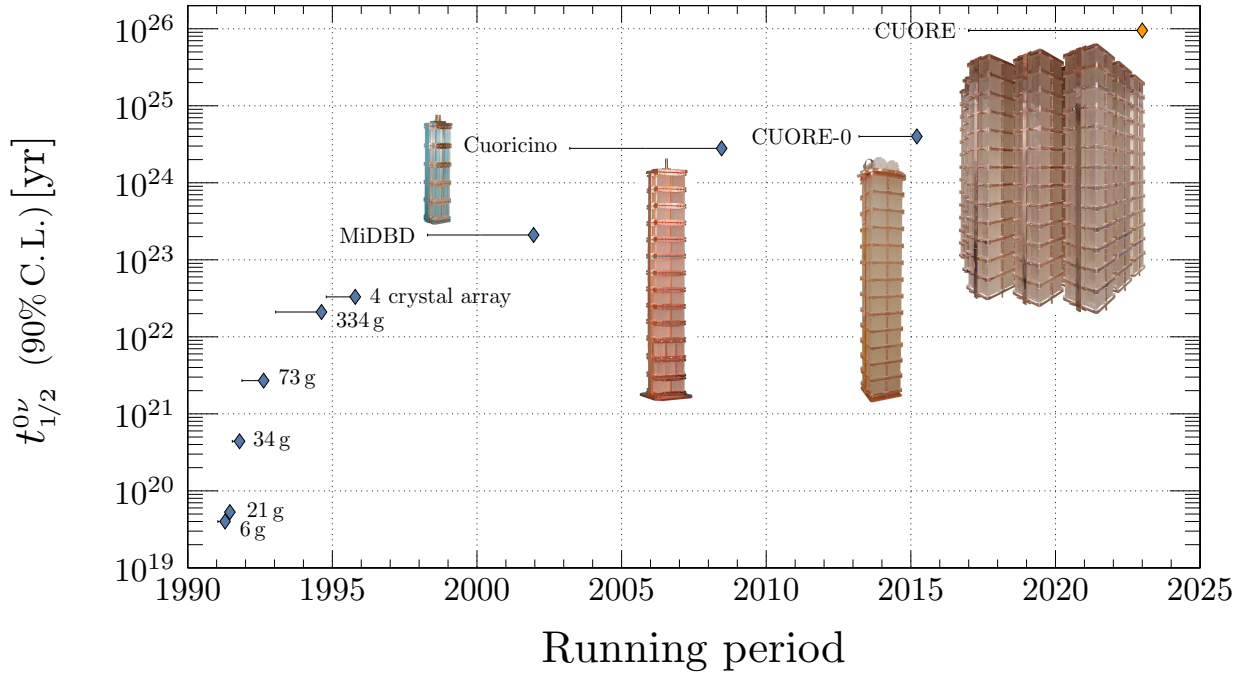


Figure 2.3: Evolution of TeO_2 bolometric experiments.

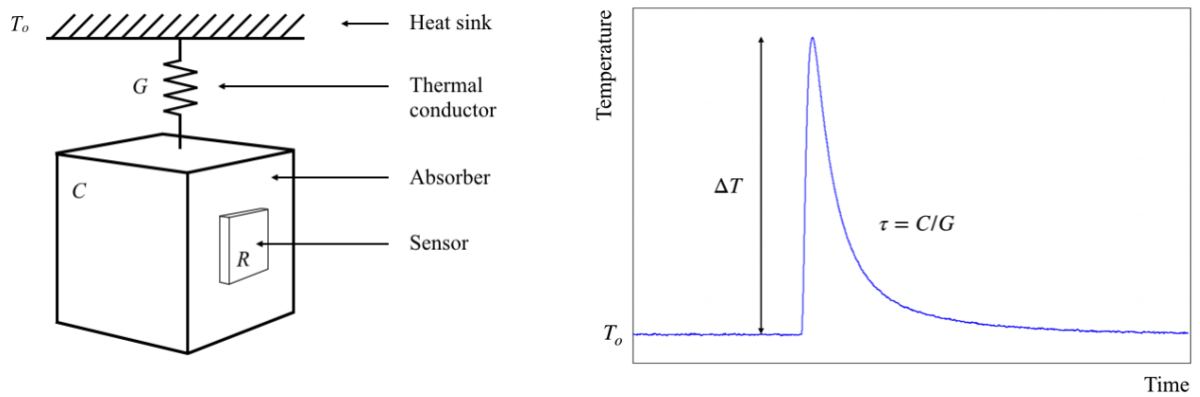


Figure 2.4: Left: Bolometer schematic where T_0 is the temperature of the heat sink, G is the thermal conductance of the thermal link between the heat sink and absorber, C is the heat capacity of the absorber, and R is the resistance of the sensor. Right: Signal measured by sensor labeled with thermal parameters where τ corresponds to the decay time constant of the thermal signal.

thermally coupled to a temperature *sensor* and a *heat sink*. The absorber converts detected energy depositions to heat that subsequently flows to the heat sink. As the heat flows

from the absorber, the sensor measures the resulting temperature change. The temperature change can be written in terms of the deposited energy (E), the heat capacity (C) of the absorber, the temperature (T_o) of the heat sink, and the thermal conductance (G) of the weak, thermal coupling between the absorber and the heat sink:

$$\Delta T(t) = \frac{E}{C} e^{-t/\tau} , \quad (2.1)$$

where $\tau = C/G$, the time decay constant of the thermal signal. Following the low-temperature limit of the Debye law,

$$C(T) \propto k_B \left(\frac{T}{\Theta_D} \right)^3 , \quad (2.2)$$

where C is the heat capacity, k_B is the Boltzmann constant, T is the temperature, and Θ_D is the material-dependent Debye temperature [15]. The intrinsic energy resolution scales with the operational parameters as:

$$\sqrt{\langle \Delta E^2 \rangle} \propto k_B T \left(\frac{T}{\Theta_D} \right)^{3/2} , \quad (2.3)$$

which is negligible at low temperatures compared to other sources of noise.

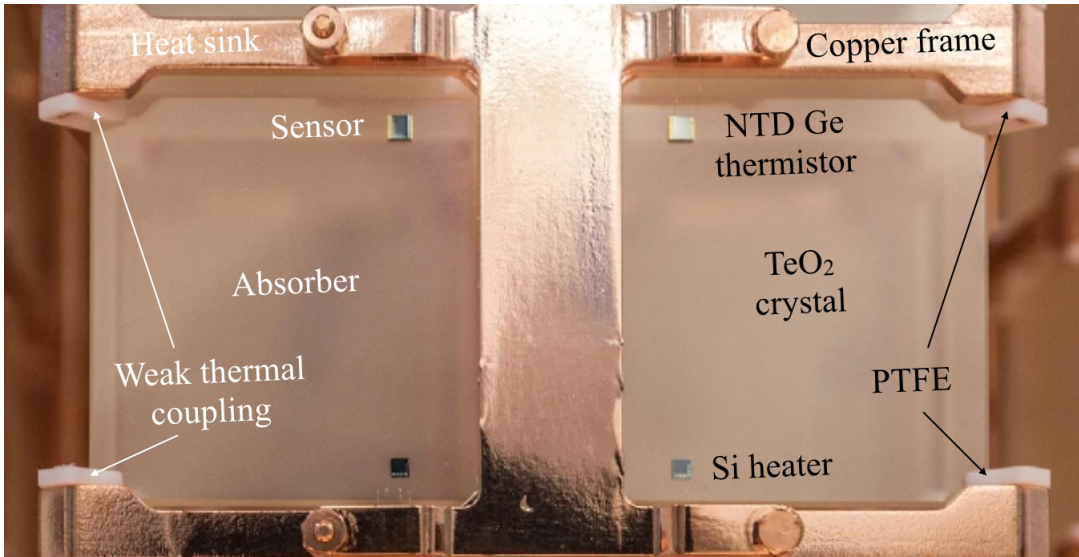


Figure 2.5: CUORE bolometer. Bolometer component labels are on the left and corresponding CUORE bolometer part labels are on the right.

A CUORE bolometer is shown in Figure 2.5. In a CUORE bolometer, the TeO₂ crystal acts as the absorber, the semiconductor thermistor acts as the sensor, the PTFE holders act

as the weak, thermal conductors, and the copper support structure acts as the heat sink. Semiconductor thermistors are characterized by their *logarithmic sensitivity* (η):

$$\eta = \left| \frac{d \log R(T)}{d \log T} \right|, \quad (2.4)$$

where $R(T)$ is the thermistor resistance at temperature T . CUORE uses neutron-transmutation-doped germanium (NTD Ge) thermistors as sensors. The NTD Ge resistances (R) are characterized by:

$$R(T) = R_0 e^{\sqrt{(T_0/T)}}, \quad (2.5)$$

where T is the temperature, T_0 is a parameter that depends on the NTD doping concentration, and R_0 is a parameter that depends on the NTD doping concentration and NTD geometry. The CUORE thermistors were designed to have similar parameter values as in Cuoricino with $T_0 \sim 4 \text{ K}$ and $R_0 \sim 1 \text{ } \Omega$. For further details, see [12].

2.3 Electronics

The CUORE electronics consists of the front-end board, anti-aliasing filter board, pulser board, power supply regulation, high-stability voltage references, and data acquisition system (DAQ). The CUORE electronics boards were designed to be remotely programmable to address the number of CUORE bolometers and their broad spread of characteristics. The electronics settings are optimized for each bolometer to achieve the best signal to noise ratio (see Section 2.7). A schematic of the CUORE electronics is shown in Figure 2.6.

The front-end board interfaces with the NTD thermistor to supply the bias current and measure and amplify the voltage change across it. The front-end board uses a two-stage amplification system consisting of a differential voltage-sensitive preamplifier (DVP) and a programmable gain amplifier (PGA). The DVP is used to suppress cross-talk and common-mode disturbances and the PGA is used to accommodate the spread of energy conversion gain ($100 \text{ } \mu\text{V/MeV} - 400 \text{ } \mu\text{V/MeV}$) of the detectors. The gain and offset are chosen to exploit the dynamic range of the DAQ. Each front-end board has six channels and each channel accommodates one bolometer.

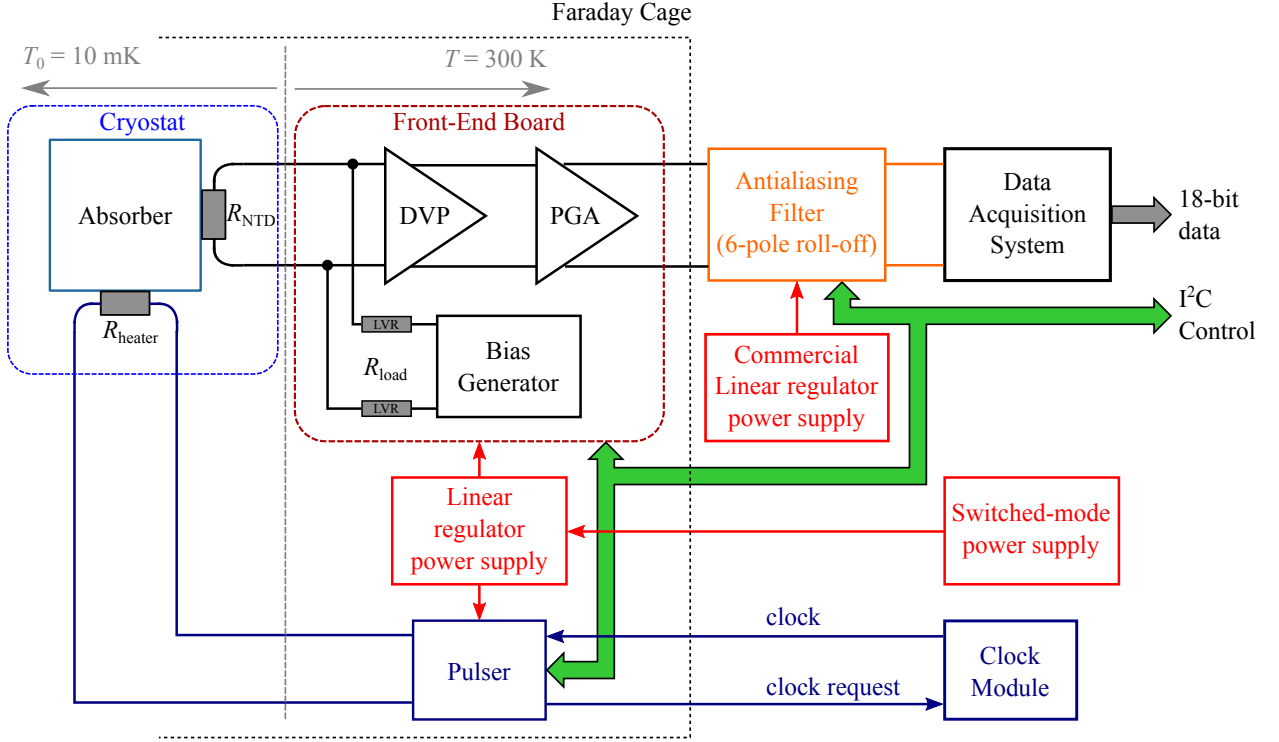


Figure 2.6: Schematic of the CUORE electronics. The electronics are stored above the cryostat at room temperature. A Faraday cage houses the electronics boards interfacing with the resistors on the crystal.

The front-end board outputs the amplified voltage signal to the anti-aliasing filter board. In CUORE, we use a 6-pole Bessel-Thomson low-pass filter with a roll-off of 120 dB/decade to preserve the input signal shape. Each filter board has 12 channels and each channel accommodates one front-end channel. Each filter board channel can impose four possible cut-off frequencies: 15 Hz, 35 Hz, 100 Hz, or 120 Hz.

The pulser board interfaces with the Si heater resistor attached to the crystal to deliver voltage pulses that induce Joule heating in the resistor. CUORE uses the pulser board to deliver periodic square voltage pulses, of fixed amplitude and width, so that the heater-induced signals measured by the NTD thermistor can be used for thermal gain monitoring. Each pulser board has four channels and each channel drives heaters that are connected in parallel and affixed to a column of 13 bolometers. For each pulser board channel, the amplitude and width of the square pulse are configurable.

The power supply chain includes an AC-to-DC converter (AC/DC), DC-to-DC converter (DC/DC), power supply filter, and linear power supply (LPS). The commercial (TDK-Lambda) AC/DC converts 230 V AC to 48 V DC, which the DC/DC converts to ± 6.5 V analog and 5 V digital. The filter, between the DC/DC and dual LPS, reduces the noise and protects the front-end board. Since the DC/DC is located outside the Faraday room, the length-dependent inductance of the cable ($\sim 10 \mu\text{H}$) enables a large amount of energy to be stored in the event of an accidental short circuit; the capacitance and overall design of the filter was chosen to limit the voltage rise that would result from the energy released from this type of occurrence. The LPS acts as a high precision voltage regulator that delivers ± 5 V analog after converting the filtered analog voltage from the DC/DC. An underplane board distributes the power from the dual LPS to one crate of front-end boards; each crate houses 13 front-end boards. The underplane board is also used to merge the output of every two front-end boards to output to the anti-aliasing filter boards. A power supply filter is not required between the DC/DC and anti-aliasing filter boards since they are in close proximity.

The UCLA group was responsible for the quality assurance of the CUORE electronics system. In 2014, I was involved with testing the front-end and pulser boards. In 2015, I was involved in testing the underplanes. In testing the functionality of 180 front-end boards, we tested the power voltages, the gain of the preamplifier and PGA, the compensation voltage, bias voltage, load resistors, and ICP circuit. We found nearly 70 boards had to be reworked. The majority of problems were related to the custom load resistors; 66 load resistors had to be replaced. In testing the functionality of 23 pulser boards, we used an environmental chamber to test the pulse width at 20°C , 30°C , 40°C and drifts of the pulse width, pulse amplitude, and gain between $20^\circ\text{C} - 30^\circ\text{C}$, $30^\circ\text{C} - 40^\circ\text{C}$, and $20^\circ\text{C} - 40^\circ\text{C}$. During our inspection, we identified two boards with substantial drifts in gain and amplitude and three boards with substantial drifts in pulse width. For the testing of the underplanes, my primary task was to confirm their functionality to shut off in the case of over- and under-voltages. For each underplane, only two channels were used, one from each half of the underplane since hardware was limited, and since each half of the underplane shares the same source. For the test, my Matlab code prompted the commercial power supplies to cycle through

a preset combination of voltages. At each test point, Matlab read back the voltages and current consumption from the power supplies, then prompted a multimeter to measure the input voltages to the front-end board. My test confirmed that the input voltages to the front-end board go to zero if any of the voltages (positive analog, negative analog, or digital) was less than 3V or greater than 6V; for voltages within range, the measurements of the input voltages to the front-end boards were the same as the test point commercial power supply voltages.

2.4 Cryostat

As discussed in Section 2.2, the CUORE bolometers must be operated at a sufficiently low temperature (~ 10 mK). The CUORE cryostat uses three cooling systems to bring the CUORE detector to operating temperature: the *Fast Cooling System* (FCS), the *Pulse Tube* (PT) system, and the *Dilution Unit* (DU).

The FCS is an external cryostat that is cooled by 3 commercial Gifford-McMahon cryorefrigerators [16]. The high cooling power of the cryorefrigerators allows for reasonable cooling time (~ 10 days) of the initial phase from 300 K to 50 K. In order to reach 50 K, the FCS cools and pumps helium gas to the IVC. When 50 K is reached, most of the gas is evacuated, while the remaining gas acts as an exchange gas until ~ 10 mK.

The second cooling system consists of 5 commercial PT refrigerators that replace the need for liquid helium [17]. We chose this cryogen-free approach to reduce the cost and downtime of the system otherwise associated with using the cryogen liquid. Because of their lower cooling power, the PTs are activated only after the IVC reaches ~ 200 K. After ~ 50 K, the FCS is no longer needed and is switched off and the PTs continue to cool down to their base temperature of ~ 4 K without the FCS. The PTs are able to achieve this temperature with a two-stage design. The base temperature of the first stage is ~ 40 K and is in thermal contact with the 40 K plate. The base temperature of the second stage is ~ 4 K and is in thermal contact with the 4 K plate.

The final cooling system is a custom DU refrigerator [18]. In the CUORE cryostat, the

Mixing Chamber is in thermal contact with the 10 mK plate; the *Still* is in thermal contact with the 600 mK plate; and the *Heat Exchangers*, between the Still and the Mixing Chamber, is in thermal contact with the 50 mK plate. When the DU is activated, it initially circulates a $^3\text{He}/^4\text{He}$ gas mixture. The incoming mixture is cooled to below 0.87 K in stages, first through thermalization with the PT-cooled plates, then through a condenser followed by a Joule-Thomson constriction valve, and lastly through heat exchangers. Below 0.87 K, the liquefied mixture separates into a concentrated ^3He phase and a dilute phase that mostly consists of ^4He . Because of the relative density of the two phases, the dilute phase rests at the bottom of the DU, in the Mixing Chamber. Also in the Mixing Chamber, above the dilute phase, is the concentrated phase. The final cool down to ~ 10 mK occurs at the boundary of the two phases through continuous evaporation of ^3He from the concentrated phase into the dilute phase. The evaporation occurs and is sustained by continuously distilling ^3He from the dilute phase, which disturbs the equilibrium between the two phases. This distillation occurs in the Still, where the dilute phase is heated to ~ 600 mK – 800 mK to increase the vapor pressure and a pump is applied. At ~ 600 mK, the pump mostly removes the ^3He gas from the Still because of its relatively high vapor pressure compared to ^4He and returns the gas to the DU. Osmosis of ^3He from the Mixing Chamber to the Still occurs because of the concentration gradient caused by the removal of ^3He in the Still. The flow rate, controlled by the heat applied to the Still, determines the temperature of the Mixing Chamber. For further details, see [19].

2.5 Inactive material selection and radiopurity controls

From Cuoricino, we expect degraded alphas from ^{238}U and ^{232}Th surface contamination of the copper structures near the detector to be the largest source of background in the ROI [20]. In CUORE, the copper structures closest to the detector include the copper support tower and the 10 mK vessel. In this section, we discuss the selection and cleaning procedures of the inactive materials near the detector. For details on the crystal production, see [21].

In CUORE, we use a high-purity Electrolytic Tough Pitch (ETP1) copper alloy manufac-

tured by Aurubis under the proprietary name NOSV [22]. NOSV copper was chosen for its low bulk radioactivity ($\leq 2.0 \times 10^{-6}$ Bq/kg ^{232}Th , $\leq 6.5 \times 10^{-5}$ Bq/kg ^{238}U), an important property for rare event searches; low hydrogen content, an important property in cryogenic applications; and high thermal conductivity, an important property of heat sinks in bolometer applications [23]. A cleaning procedure (TECM) consisting of precleaning, tumbling, electropolishing, chemical etching, and magnetron-plasma etching, packaging, and storage was developed to reduce the surface contamination of the copper parts before tower assembly and installment [24]. As part of the procedure, before each erosion process, the copper parts are cleaned in an ultrasonic bath and rinsed to remove any residuals from the previous step. The procedure erodes ~ 100 μm of copper from the surface. To reduce the background from the 10 mK vessel, thin NOSV copper tiles were cleaned with the TECM procedure and used to line the inside of the vessel. The PTFE holders are the next largest inactive structures near the detector. They were chosen for their low bulk radioactivity ($\leq 6.1 \times 10^{-6}$ Bq/kg ^{232}Th , $\leq 2.2 \times 10^{-5}$ Bq/kg ^{238}U) and their thermal properties; the PTFE holders are used to compensate for thermal contraction between the crystals and copper support tower and to impede heat flow to the copper support tower following a detected energy deposition [23]. The PTFE surfaces were cleaned with soap and ultra-pure nitric acid. The tower assembly procedure was designed to prevent recontamination of the detector parts. For further details, see [12].

2.6 Radiation shielding

As shown in Figure 2.2, lead shielding is placed inside the cryostat to shield the detector from background sources originating from the cryostat structures. This internal lead shielding consists of both modern and Roman lead [25]. Above the detector, at 50 mK, the top lead shield consists of 30 cm-thick modern lead. At the 4 K stage, 6 cm-thick Roman lead is below and on the sides of the detector. The sub-Kelvin copper vessels and plates shield the detector from background sources originating from the lead. TECM-cleaned, malleable NOSV copper tiles are used to line the inside of the 10 mK cryostat vessel to shield the

detectors from alpha radiation from the innermost vessel.

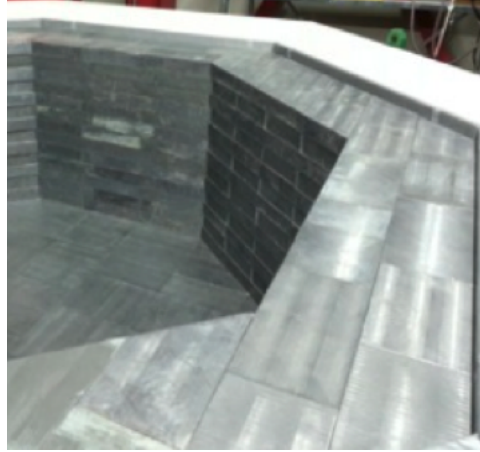


Figure 2.7: Photo of external shielding.

Three layers of radiation shielding are outside the 300 K cryostat vessel. The outermost external shield, made of 18 cm-thick polyethylene (PE), thermalizes fast neutrons. Adjacent to the PE are 2 cm-thick boric-acid panels, which capture the thermal neutrons thereby reducing the flux impinging on the detector. The base of the neutron shielding is made of 20 cm-thick borated polyethylene. The innermost external shield is 25 cm-thick modern lead that attenuates gamma rays from the sides and below the detector. A photo of the external shielding is shown in Figure 2.7.

2.7 Working point measurement

The optimal bias current, or optimal *working point*, for each bolometer is unique and must be determined experimentally. A schematic of the biasing circuit for the NTD is shown in Figure 2.8. The voltage applied to the biasing circuit, or bias voltage (V_{bias}), is

$$V_{bias} = I \cdot (R_L + R_{NTD}) , \quad (2.6)$$

where I is the bias current, R_L is the load resistance, and R_{NTD} is the thermistor resistance given by Equation 2.5. With $R_L \gg R_{NTD}$, the bias current is approximately constant and the voltage across the thermistor (V_{NTD}) is

$$V_{NTD} = I \cdot R_{NTD} . \quad (2.7)$$

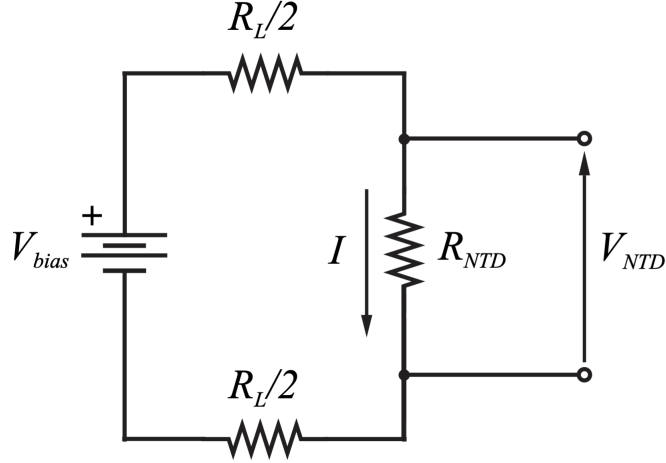


Figure 2.8: Schematic of the NTD biasing circuit.

From Equation 2.4 and 2.7, the maximum NTD voltage variation (ΔV) is related to its maximum temperature variation (ΔT):

$$\frac{\Delta V}{V_{NTD}} = \eta \frac{\Delta T}{T}, \quad (2.8)$$

where T is the instantaneous temperature of the NTD and η is the logarithmic sensitivity. This temperature is affected by the power (P) dissipated by the current through the thermistor:

$$T = T_o + \frac{P}{G}, \quad (2.9)$$

where T_o is the temperature of the heat sink, $P = I \cdot R_{NTD}^2$, and G is the thermal conductance between the NTD and heat sink. From Equation 2.8 and 2.9, this power dissipation limits the NTD voltage variation when P/G is comparable to T_o . This behavior is known as *electrothermal feedback* and is demonstrated by the *load curve* in Figure 2.9. The load curve, or I-V curve of a semiconductor thermistor, at a given T_o is linear for low bias current. When the current is sufficiently high, electrothermal feedback causes the load curve to become nonlinear and limits signal amplitude given by the NTD voltage variation in Equation 2.8. Figure 2.9 identifies the optimal working point as the bias that maximizes the signal amplitude. In this case, the optimal bias is given by the *load line* that intersects the point in the load curve that corresponds to the maximum signal amplitude. The load line is given

by the bias voltage (Equation 2.6) in terms of the NTD voltage (Equation 2.7):

$$V_{NTD} = V_{bias} - I \cdot R_L . \quad (2.10)$$

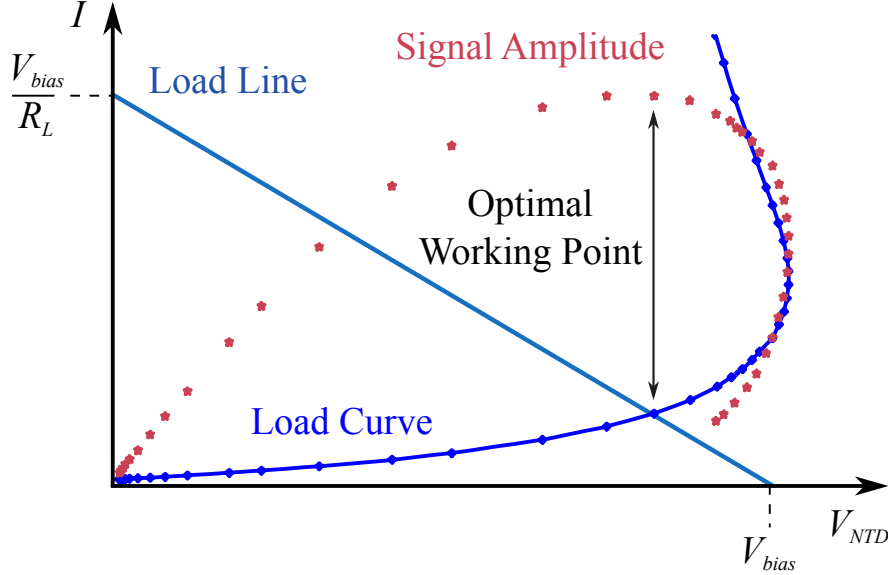


Figure 2.9: Figure from [26]. Example of a load curve.

In CUORE, instead of the signal amplitude, we use the signal-to-noise ratio (SNR) to select the optimal working point. We perform the *working point measurement* to construct the SNR characteristic curve as a function of the bias voltage for this purpose. For the SNR at a given bias voltage, we measure the “signal” as the amplitude of the average pulse constructed from heater-induced pulses, where the amplitude is the maximum displacement from its baseline, and we measure the “noise” as the integral of a frequency-weighted average noise power spectrum constructed from measurements of V_{NTD} corresponding to periods without any particle- or heater-induced pulses. An example of an SNR characteristic curve and related characteristic curves are shown in Figure 2.10. When selecting the optimal working point, we exclude bias voltages that induce oscillations in V_{NTD} from electrothermal feedback. This *unstable region* is determined beforehand with dedicated load curve measurements, so the optimal working point considers both the quality of the pulse shape and the SNR. For further details, see [27].

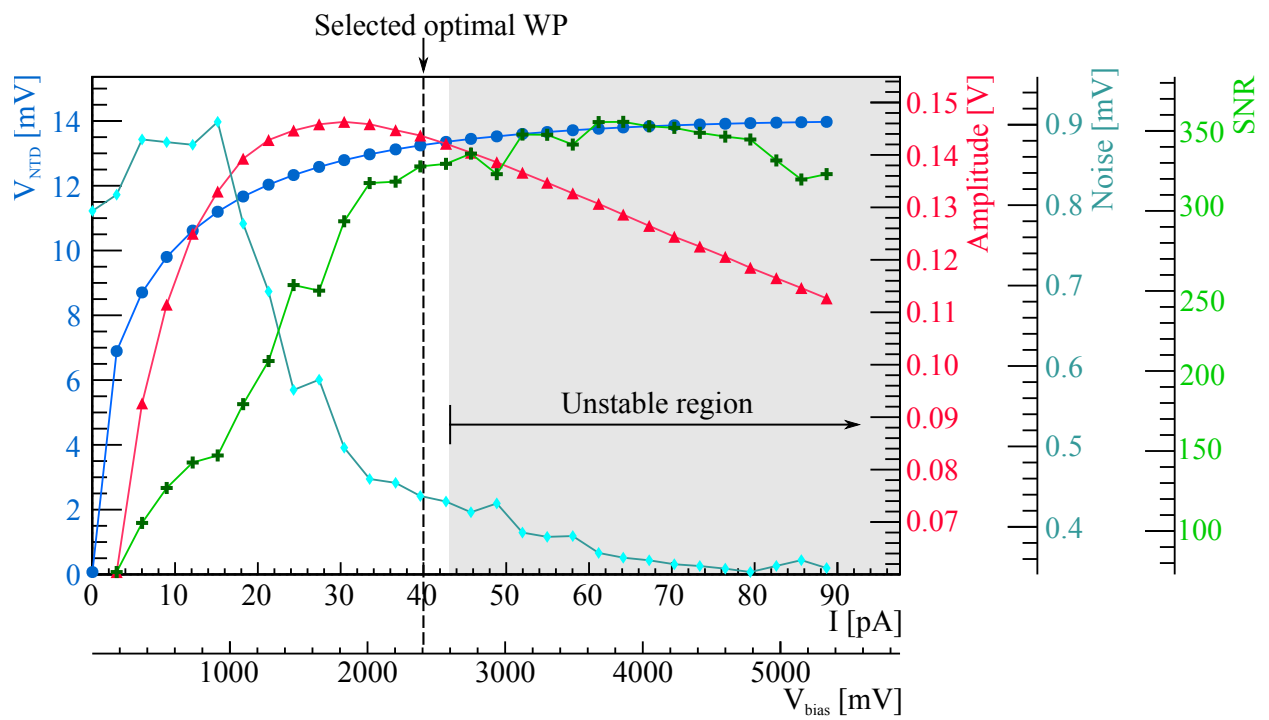


Figure 2.10: Figure from [26]. Characteristic curves for working point determination of one bolometer.

CHAPTER 3

CUORE data production

3.1 Introduction

As discussed in Chapter 2, the CUORE electronics convert the temperature rise in a CUORE TeO₂ crystal to a voltage representative of the energy deposited in the crystal. This chapter discusses the analysis procedures to convert the measured voltages to the energy spectra used to produce the CUORE results.

CUORE data is collected as continuous voltage waveforms in ~ 24 -hour-long intervals or *runs*. Before the data collection begins, each run is preassigned a run type: calibration, background, or working point.

- *Calibration runs* are ~ 24 hours long and are taken while radioactive calibration source strings are deployed around the detectors. The measurements are used to calibrate pulse amplitudes to energy.
- *Background runs* are ~ 24 hours long and are taken while the calibration strings are extracted. The measurements are used for rare event searches.
- *Working point runs* are ~ 3 hours long and are taken while the calibration strings are extracted. The measurements are used to determine and monitor the stability of the NTD thermistor resistance values.

During or after the data collection, software trigger algorithms flag three types of *events*: signal, noise, and pulser.

- *Signal events* contain identified pulses.

- *Noise events* coincide with periodic triggers that are representative of random noise.
- *Pulsar events* coincide with the periodic heat pulse injections delivered through the Si Joule heater.

Each event corresponds to a 10-second window including a 3-second pretrigger. The event type is used to flag the type of analysis required.

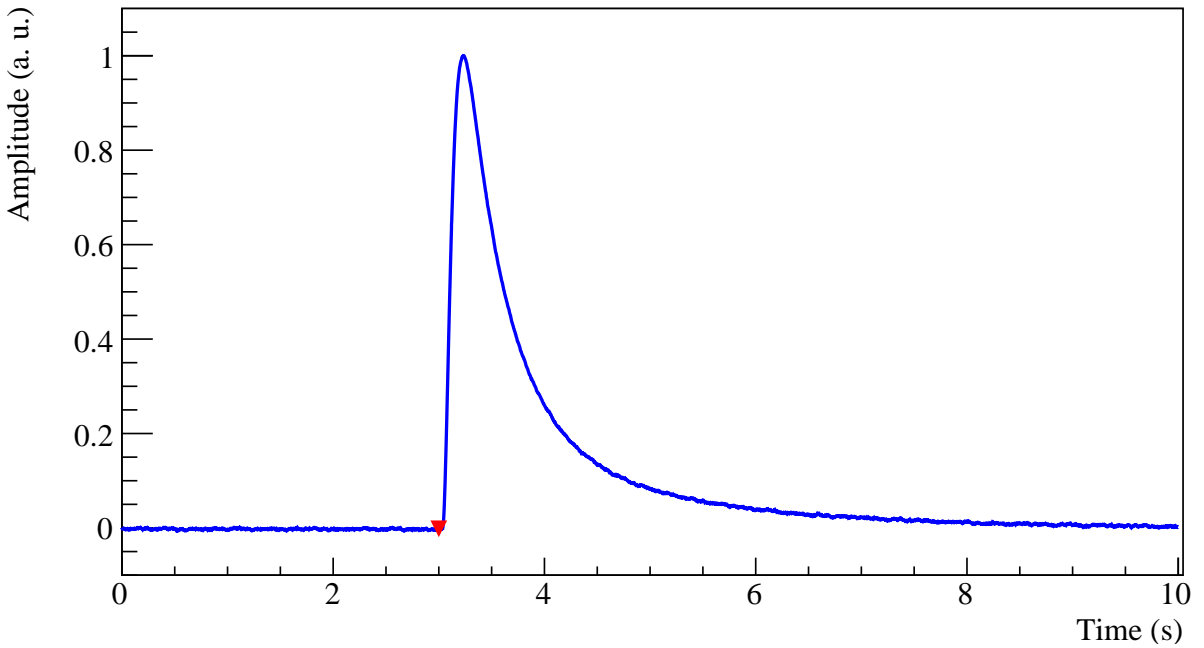


Figure 3.1: Signal event example. The red marker indicates the trigger position.

The data production procedure is performed over a *dataset*, a collection of runs taken in the following sequence: ~ 4 days of initial calibration runs, $\sim 1 - 1.5$ months of background runs with weekly working point runs, and ~ 4 days of final calibration runs. Adjacent datasets typically share intermediate calibration runs to improve the duty cycle.

During the collection of the dataset, after each run has ended and before any data production can begin, *bad intervals* are flagged to exclude periods of unstable or sub-optimal data-taking. After the bad intervals are flagged, the data undergo *online processing*, a minimal data production procedure meant to provide daily feedback on the data quality to the detector operators. When the dataset is complete, the data are retriggered and undergo

the *offline reprocessing* procedure that is used to produce the physics data for high-level analysis.

3.2 Offline reprocessing

Before the offline reprocessing is performed, the data are retriggered using the *optimum trigger* (OT). For the OT, the data are filtered to reduce noise before running the pulse finding algorithm. Compared to the derivative trigger algorithm that is used in the online processing, the OT suppresses spurious energy depositions thereby reducing the amplitude threshold for identifying pulses. The OT algorithm is discussed in detail in [28]. In this section, I will discuss the analyses performed during the offline reprocessing.

Preprocess is the first analysis sequence; it computes basic information associated with each event to inform later steps of the analysis. For each event, information on the baseline, using either 75% of the pretrigger or the full acquisition window, is computed. This information includes its mean value; its slope and intercept from a linear regression fit; the baseline RMS, which corresponds to the root mean square of the residuals from the fit; and the baseline flat RMS, which corresponds to the root mean square of the data points in the baseline from the mean. The number of pulses and pulse peak positions in each event window are found by differentiation. Although multiple pulses can be present in the same event window, each event corresponds to a primary trigger. The maximum amplitude, which corresponds to the displacement from the baseline average, and its position associated with this trigger are identified and used to determine other basic pulse shape parameters including the rise time, corresponding to the time between 10% and 90% of the maximum value along the rise of the pulse; decay time, corresponding to the time between 90% and 30% of the maximum value along the decay of the pulse; and slow decay time, corresponding to the time between 30% and 10% of the maximum value along the decay of the pulse.

Optimum filter (OF) amplitude A better estimation of the pulse amplitude is obtained using an optimum filter [29]. The OF operates in the frequency domain to determine the weight of each Fourier component based on their signal-to-noise ratio (SNR). The ampli-

tude sequence first constructs the OF for each channel by evaluating the frequency-dependent SNR from the Fourier transform of the channel's average pulse, representative of the ideal signal, and the average noise power spectrum. The sequence then applies the OF to each event to determine its OF amplitude. The *average pulse* (AP) and *average noise power spectrum* (ANPS) sequences precede the amplitude sequence. The AP sequence identifies and averages high-quality signal events from calibration runs corresponding to the 2615 keV gamma line from ^{208}Tl . Events with a maximum amplitude exceeding a specified multiple of the baseline rms, no additional pulses in the event window, and relatively flat baseline slope are included in the average. An example of an average pulse is shown in Figure 3.2. The ANPS sequence identifies and averages high-quality noise events from background runs. These events have no pulses in the event window and a relatively flat full-window baseline slope. Before averaging, the events are baseline subtracted according to the mean value of the full window before transforming the samples to frequency space using the Welch window to mitigate spectral leakage. An example of an average noise power spectrum is shown in Figure 3.3.

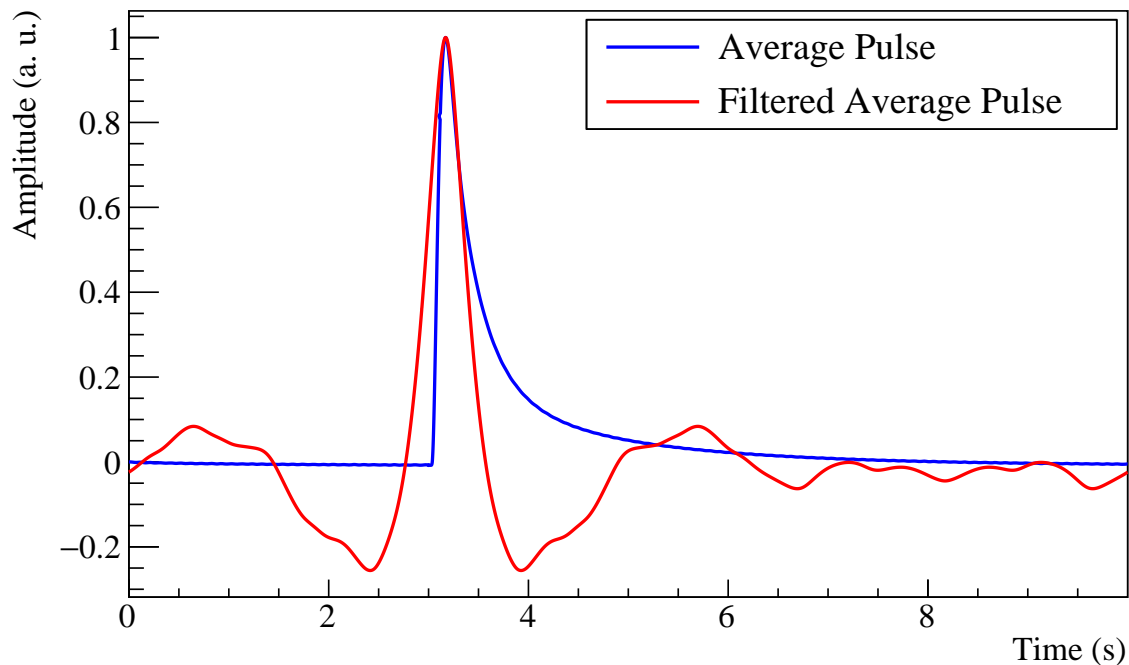


Figure 3.2: An example of an average pulse in the time domain.

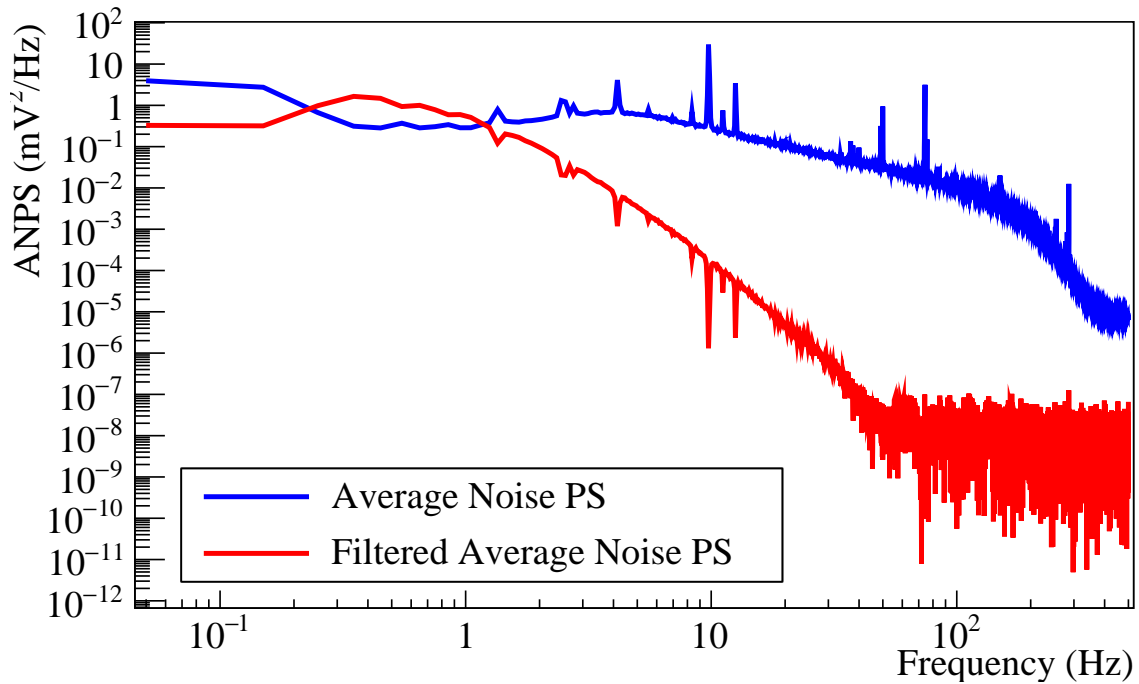


Figure 3.3: An example of an average noise power spectrum in the frequency domain.

Thermal gain stabilization (TGS) Thermal drifts in the detector can cause a physical energy deposition to be reconstructed at different values. By correcting for this drift, we improve our energy resolution and sensitivity. We use two methods to correct for thermal drifts: *heaterTGS* and *calibrationTGS*. In both methods, events of the same energy, or nearly similar energies, are used to determine the temperature-dependent gain in the amplitude.

Using the baseline as a proxy for temperature, the relationship between amplitude (a_H) and baseline (b) for a particular physical energy (E_H) is shown in Figure 3.4. The thermal gain, $G(b)$ relates the measured amplitude for a given baseline to the physical energy:

$$a_H(b) = G(b) \cdot E_H \quad (3.1)$$

Assuming the gain is the same for an arbitrary pulse with amplitude, a and physical energy, E :

$$a(b) = G(b) \cdot E \quad (3.2)$$

then,

$$\frac{E}{a(b)} = \frac{E_H}{a_H} \quad (3.3)$$

and the physical energy of the arbitrary pulse is:

$$E = a(b) \cdot \frac{E_H}{a_H(b)} . \quad (3.4)$$

But until the energy calibration is performed, a stabilized amplitude, a_s independent of the baseline is defined in arbitrary units as:

$$a_s(a.u.) \equiv E \cdot \frac{5000}{E_H} \equiv 5000 \cdot \frac{a(b)}{a_H(b)} \quad (3.5)$$

where the factor of 5000 is arbitrary. Applying Equation 3.5 to the data in Figure 3.4, we have Figure 3.5 which provides a narrowly distributed stabilized amplitude regardless of baseline, the desired behavior of a physical energy. For channels with functioning heaters, heaterTGS is performed for each run using pulser events as the reference events with the same energy. The analysis algorithm identifies baseline intervals where $a_H(b)$ is empirically linear and fits each range to a linear function. These linear functions are used to correct the amplitudes from the same run. calibrationTGS is performed on each channel for the entire dataset using signal events corresponding to the ^{208}Tl 2615 keV gamma line from the initial and final calibration runs as the reference events. Unlike heaterTGS, the trend of $a_H(b^*)$ is empirically quadratic over the dataset (see Figure 3.6) and depends on the offset-subtracted baseline (b^*) [30]. The offset comes from the weekly working point run measurements discussed in Section 3.3. For calibrationTGS stabilized amplitudes, we use an arbitrary factor of 2615 a.u. instead of 5000 a.u. used for heaterTGS stabilized amplitudes:

$$a_s(a.u.) \equiv 2615 \cdot \frac{a(b^*)}{a_H(b^*)} \quad (3.6)$$

Energy calibration Converting the stabilized amplitudes to energy units is necessary to interpret the physics measurements, so energy calibration coefficients are determined for each channel from each set of stabilization amplitudes. Using signal events from calibration runs to construct each stabilized amplitude spectrum, peak positions corresponding to the characteristic gamma lines of the deployed calibration source strings are found and fit to a

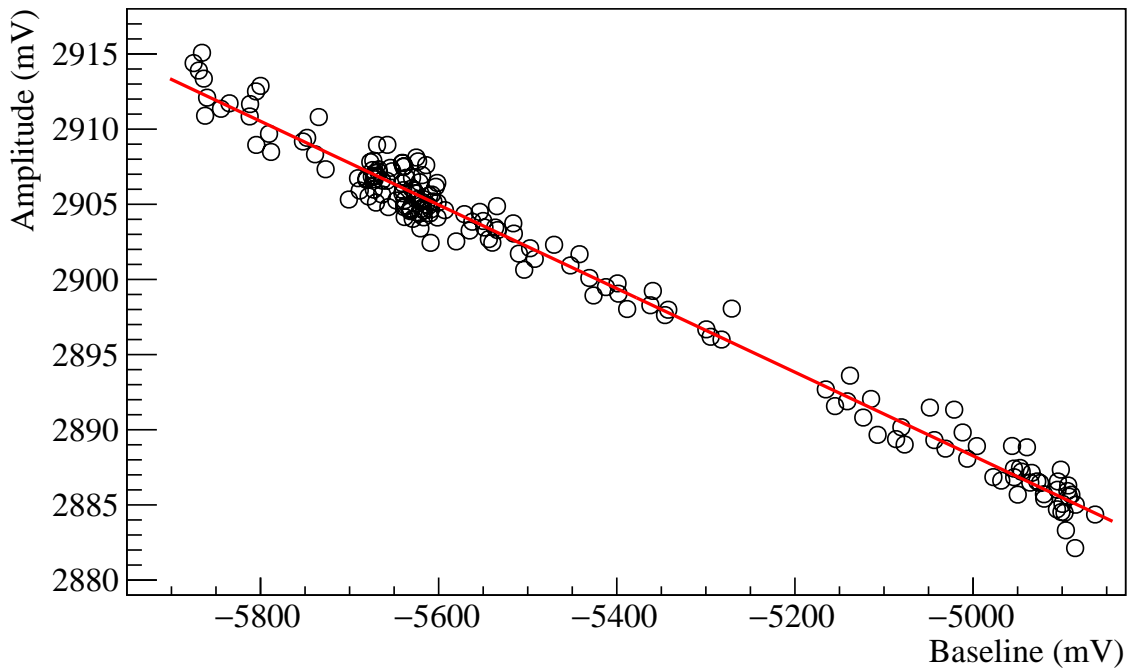


Figure 3.4: HeaterTGS baseline stabilization example using two consecutive runs. The red line corresponds to the linear fit function over the range.

quadratic function with a fixed intercept at zero. Then for all events and runs, the energy calibrations are applied to the corresponding stabilized amplitudes. After applying the energy calibrations to all events and runs, for each channel, the heaterTGS and calibrationTGS calibration spectra are compared to select the best energy estimator. The best estimator is selected based on the position accuracy and resolution of the energy peaks. In general, the heaterTGS energy estimator was found to be more robust for events across the dataset and is selected by default unless the estimator yields miscalibrated peaks or significantly worse energy resolution compared to the calibrationTGS energy estimator.

Coincidences Energy depositions from neutrinoless double-beta decay are expected to be single-site or multiplicity 1 (M1) events, where only one crystal measures the full energy of the decay. So we identify and reject multi-site or *coincidence* events to reduce the background in our neutrinoless double-beta decay search. The differences in intrinsic rise times across different detectors can lead to time delays between physically coincident events;

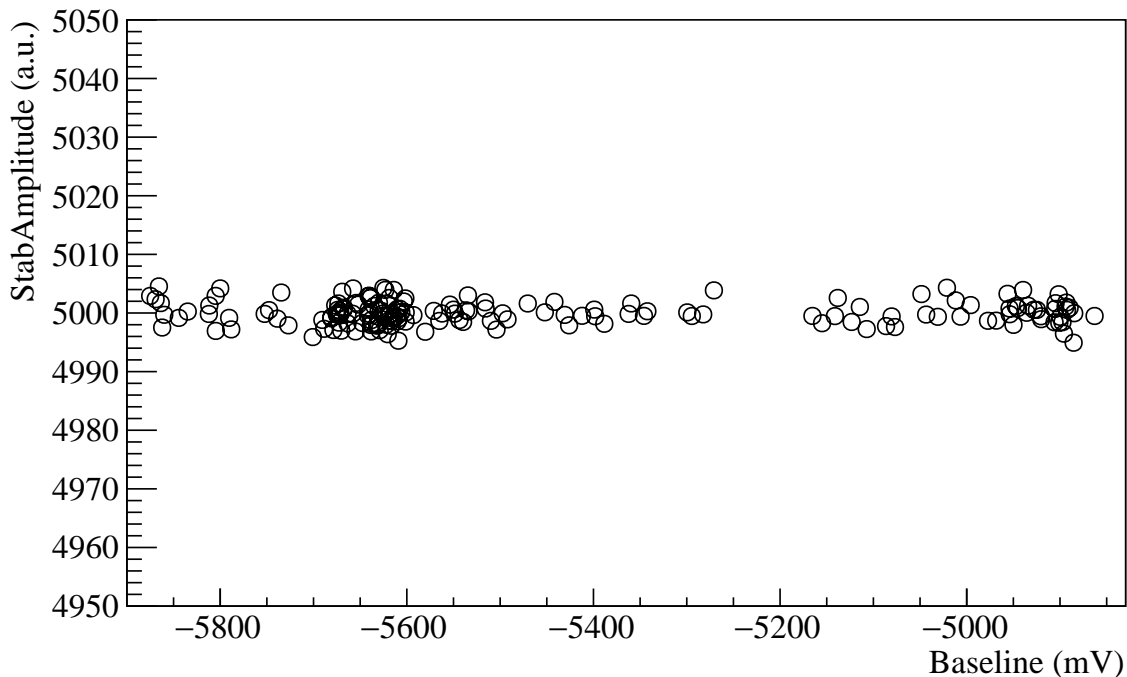


Figure 3.5: HeaterTGS stabilized amplitude example using two consecutive runs.

the coincidence analysis sequence is used to measure and correct for these delays. This sequence uses both the periodic heater pulses and preliminary multiplicity 2 (M2) events, where two bolometers are triggered, with total energy ~ 2615 keV from calibration runs to measure the time delay between crystals. After correcting or synchronizing the signal event times, the *coincidence time window* used to assign multiplicity to signal events can be reduced, which helps suppress random coincidence of events. This sequence then identifies coincidence signal events based on a coincidence time window and low-energy threshold. For the neutrinoless double-beta decay analysis, coincidence events are defined as events within a coincidence time window of ± 5 ms, where each event exceeds a low-energy threshold of 40 keV. For the two-neutrino double-beta decay analysis, the coincidence time window is ± 30 ms, the low-energy threshold is 70 keV, and an additional distance cut of 150 mm is used to reduce the random coincidences allowed by the larger coincidence time window.

Pulse shape discrimination (PSD) Many of the previous analysis sequences assume a pulse shape similar to the average pulse built into the OF in each event window, so

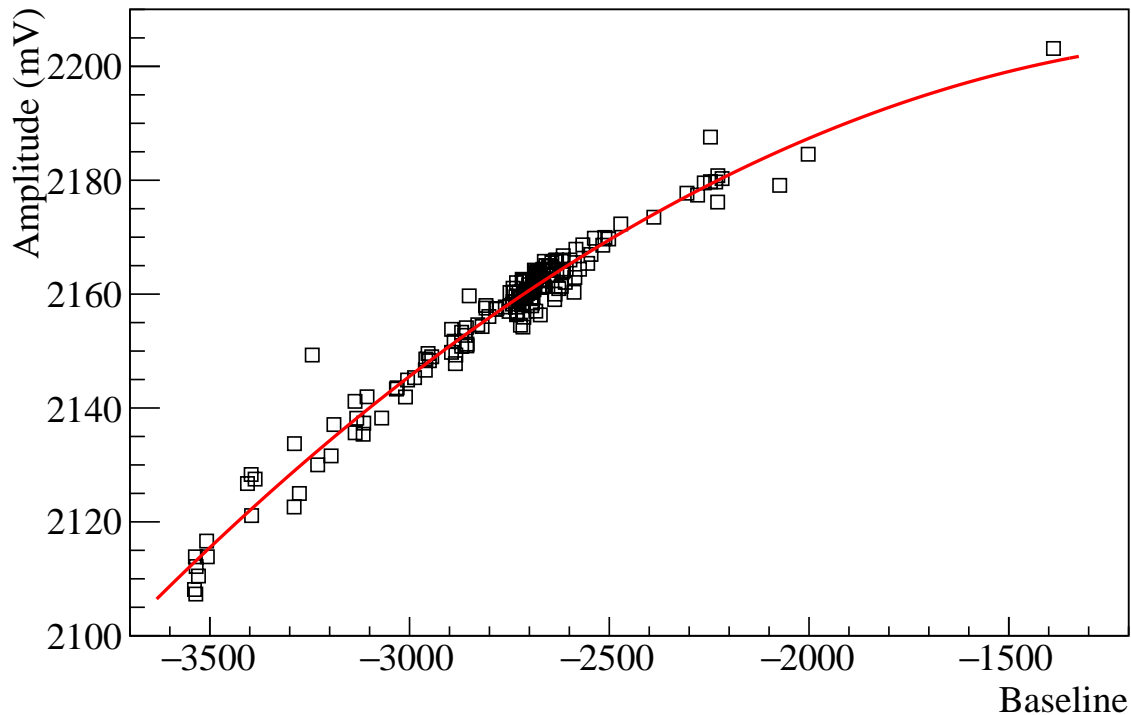


Figure 3.6: CalibrationTGS baseline stabilization example. The red line corresponds to the quadratic fit function over the range.

deviations in the pulse shape can lead to poor energy reconstructions that contribute to the background. Our PSD sequence uses Principal Component Analysis (PCA) to identify features in the pulse that can be used for discrimination [31]. These features are channel-dependent, but the leading principal component typically reflects the average pulse shape of the channel. For this reason, this sequence reconstructs each pulse based on the principal components of the corresponding channel’s average pulse and calculates the error between the reconstructed pulse and actual pulse to use for pulse shape discrimination. For further details, see [32].

Blinding For the $0\nu\beta\beta$ analysis, the ROI is blinded to avoid knowledge of the ROI data biasing the analysis procedure. The blinding algorithm transfers a random fraction of events between the ^{208}Tl 2615 keV peak and the ROI (see Figure 3.7).

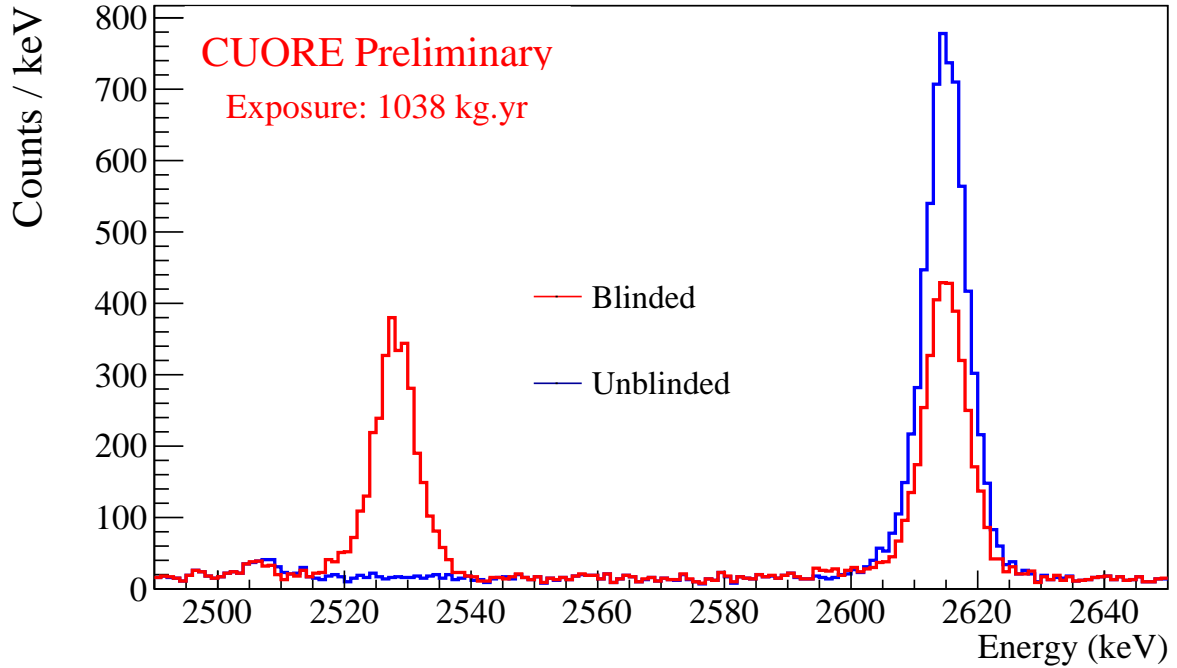


Figure 3.7: Comparison of blinded and unblinded spectrum in the affected energy range.

3.3 Online processing

In order to monitor the data quality, the online processing procedure consists of a modified subset of the offline reprocessing procedure. The analyses for the online processing only include: preprocess, OF amplitude, heaterTGS stabilization, heaterTGS calibration, and blinding. Because of the required turnaround time, the OF amplitude, stabilization, and calibration analysis sequences differ from the offline reprocessing. For the OF amplitude, only the initial calibration runs are used to construct the AP and only ~ 3 days of background runs are used to construct the ANPS. calibrationTGS cannot be performed because it requires the initial and final calibration runs, so only the heaterTGS method is performed for stabilization and calibration, and the calibration coefficients are determined from the initial calibration only.

During the online processing, radioactive source strings are deployed during the calibration runs. The number of calibration runs are determined by a threshold on the statistics

of the calibration peaks. In 2017, the first year of data-taking, CUORE used an internal detector calibration system (DCS) which provided high statistics because of the proximity of the source strings to the detectors. The source strings consisted of thoriated tungsten wires distributed along the length of the CUORE detector; they were designed to provide an average ^{208}Tl peak rate of ~ 100 mHz per bolometer. Figure 3.8 shows the locations of the calibration source strings in the internal DCS configuration. For further details, see [33]. In 2018, external calibration source strings were placed outside the 300 K vessel during calibration runs. Figure 3.9 shows the locations of the calibration source strings in the external detector calibration system (EDCS) configuration. Compared to the internal DCS, the EDCS allowed for quicker deployment and extraction and avoided warming the detector. The external source strings also used higher activity thorium sources compared to the internal DCS in order to penetrate the vessels and internal lead shielding. After installment of the EDCS, a combination of internal and external calibration source strings were used during calibration runs. At the end of 2018, the external calibration strings were modified to include ^{60}Co and were used exclusively. In this final configuration, the EDCS provided an average event rate of 125 mHz per bolometer.

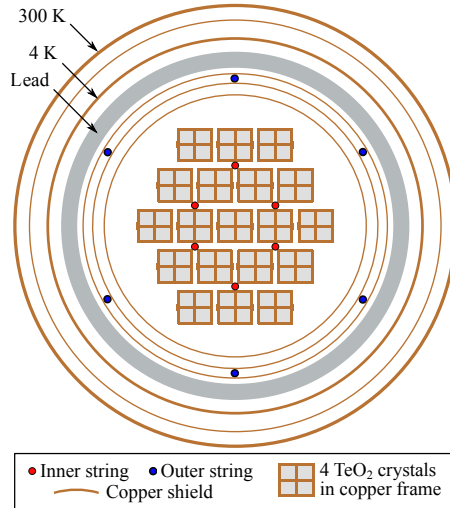


Figure 3.8: Schematic of internal DCS source string locations.

During the data collection, working point runs are used to measure the NTD resistances in order to monitor the detector temperature and stability. For these measurements, we

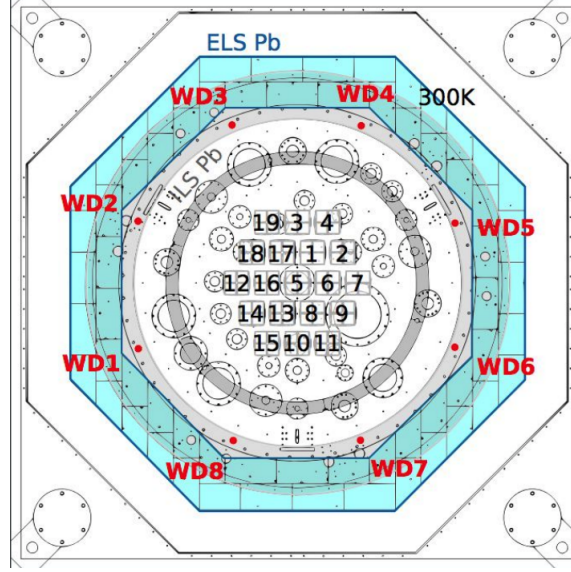


Figure 3.9: Schematic of external DCS source string locations. The red dots indicate the source string locations.

configure each bolometer to have the same amplifier gain and offset and measure the NTD resistance as the ratio of the NTD voltage and current. The NTD voltage is measured as:

$$V_{NTD} = \frac{V_{bsl}^+ - V_{bsl}^-}{2 \cdot G^*}, \quad (3.7)$$

where V_{bsl}^\pm corresponds to the average baseline constructed from fitting the full-event window of noise events for the bias polarity indicated by the superscript, and $G^* = 145 \text{ V/V}$ is amplifier gain. With Equation 2.6, the NTD resistance is

$$R_{NTD} = \frac{R_L}{V_{bias}/V_{NTD} - 1}, \quad (3.8)$$

where R_L and V_{bias} are the measured load resistance and bias voltage, respectively. During the resistance measurement, we also measure the offset (V_{offset}) to use in the calibrationTGS sequence:

$$V_{offset} = V_{bsl} + G \cdot V_{NTD}. \quad (3.9)$$

For the offset measurement, the average baseline (V_{bsl}), the gain (G), and bias voltage (V_{bias}) are configured to the optimized values used during background measurements.

In 2019, I was responsible for analyzing the working point measurements and helped

develop many of the analysis tools to monitor the NTD resistance stability. Figure 3.10 summarizes the stability of the resistances over 2 years of operation at 11.8 mK.

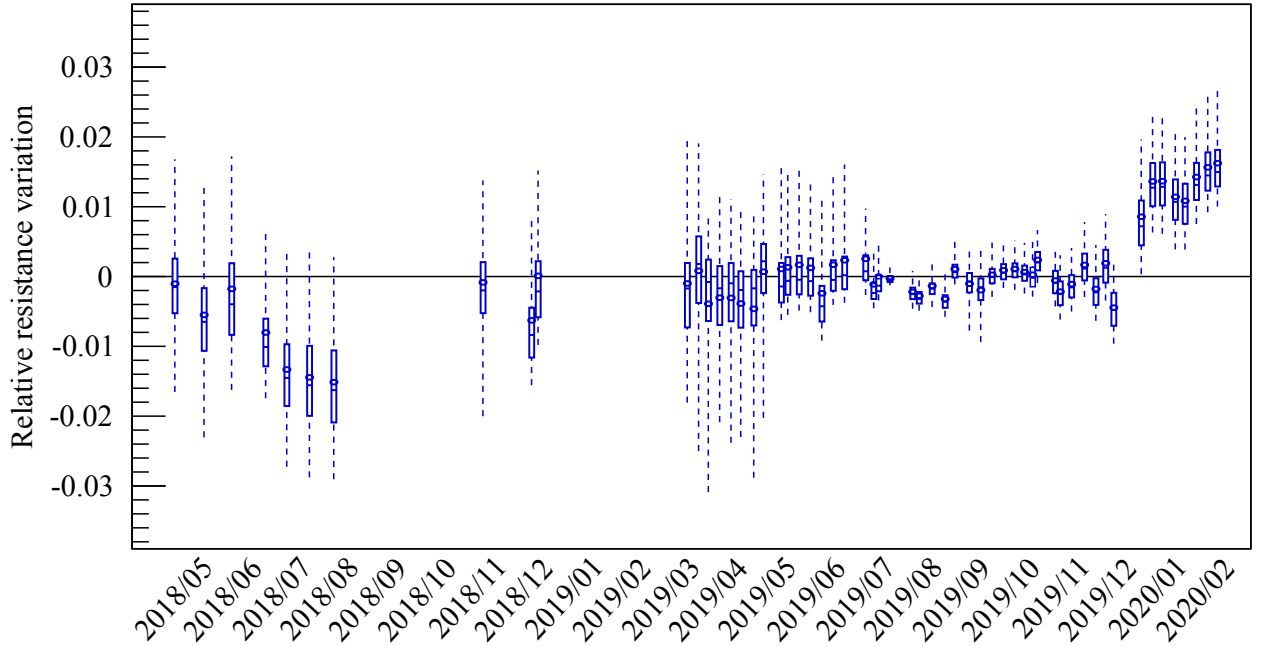


Figure 3.10: Figure from [26]. CUORE resistance stability at 11.8 mK. Each element in the plot corresponds to a single working point measurement. The data corresponds to the distribution of the channel-dependent relative variation of the R_{NTD} values defined as $(R_{NTD} - R_{NTD}^{ref})/R_{NTD}^{ref}$ where R_{NTD}^{ref} was chosen from a measurement taken in August 2019. The circle corresponds to the mean of the distribution and the horizontal line corresponds to the median. The solid box around the mean indicates the width of 50% of the distribution of the data. The dashed lines extending vertically from the boxes indicate the width of 95% of the data distribution.

3.4 CUORE data

CUORE achieved a base temperature of 7.5 mK and acquired its first pulses in January 2017. Figure 3.11 shows the accumulated exposure since physics data collection began in May 2017. Notable changes in the system configuration include the change of base temperature from 15 mK to 11.8 mK and the change of calibration source strings and their positions. A summary

of the unblinded datasets is given in Table 3.1. Figure 3.12 shows the CUORE physics spectrum with $0\nu\beta\beta$ decay analysis cuts and normalized calibration spectrum from DS3606 – DS3615. Figure 3.13 shows the $0\nu\beta\beta$ physics spectrum after the various analysis cuts.

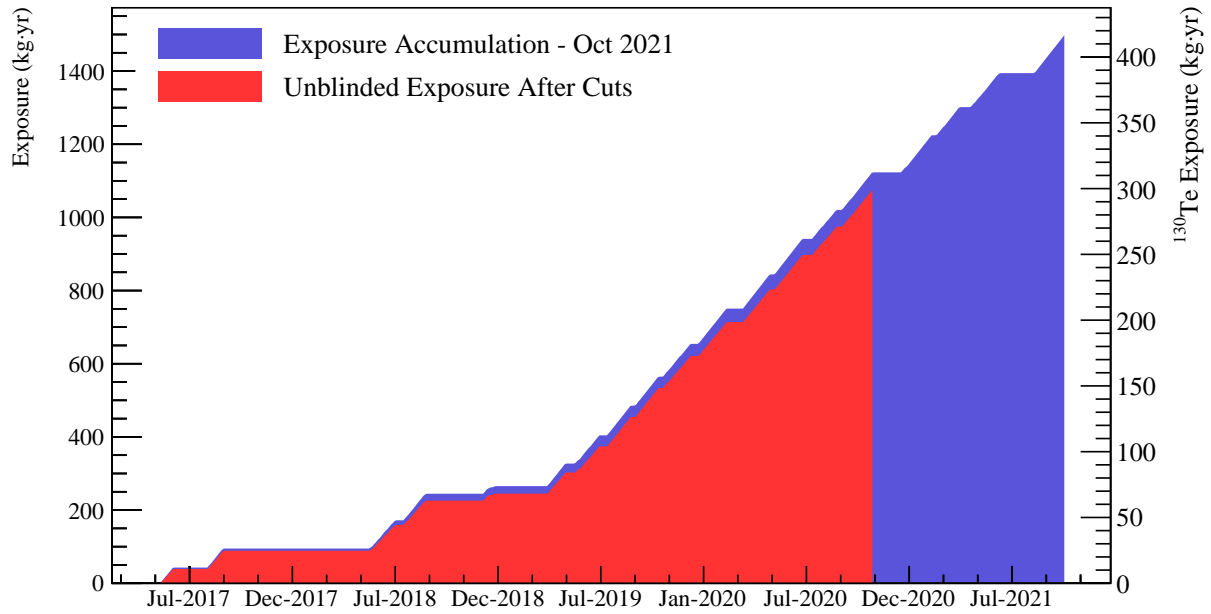


Figure 3.11: CUORE exposure. Extended flat regions indicate periods of system maintenance and upgrades.

Table 3.1: Unblinded dataset summary. Dates may overlap due to shared calibration runs between datasets. ^{232}Th hybrid corresponds to internal and external calibration source strings. External hybrid corresponds to different sources used between initial and final calibration.

Dataset	Start Date	End Date	Temperature (mK)	DCS Configuration
3601	May 05, 2017	Jun 11, 2017	15.0	Internal ^{232}Th
3602	Jul 30, 2017	Sep 12, 2017	15.0	Internal ^{232}Th
3603	Apr 21, 2018	Jul 17, 2018	11.8	^{232}Th hybrid
3604	Jul 11, 2018	Aug 30, 2018	11.8	^{232}Th hybrid
3605	Nov 29, 2018	Dec 27, 2018	11.8	External hybrid
3606	Mar 23, 2019	May 19, 2019	11.8	$^{232}\text{Th}+^{60}\text{Co}$
3607	May 02, 2019	Jul 05, 2019	11.8	$^{232}\text{Th}+^{60}\text{Co}$
3608	Jul 11, 2019	Sep 02, 2019	11.8	$^{232}\text{Th}+^{60}\text{Co}$
3609	Aug 28, 2019	Oct 21, 2019	11.8	$^{232}\text{Th}+^{60}\text{Co}$
3610	Oct 16, 2019	Dec 16, 2019	11.8	$^{232}\text{Th}+^{60}\text{Co}$
3611	Dec 11, 2019	Feb 17, 2020	11.8	$^{232}\text{Th}+^{60}\text{Co}$
3612	Mar 06, 2020	May 04, 2020	11.8	$^{232}\text{Th}+^{60}\text{Co}$
3613	Apr 29, 2020	Jul 01, 2020	11.8	$^{232}\text{Th}+^{60}\text{Co}$
3614	Jul 09, 2020	Sep 02, 2020	11.8	$^{232}\text{Th}+^{60}\text{Co}$
3615	Aug 28, 2020	Nov 02, 2020	11.8	$^{232}\text{Th}+^{60}\text{Co}$

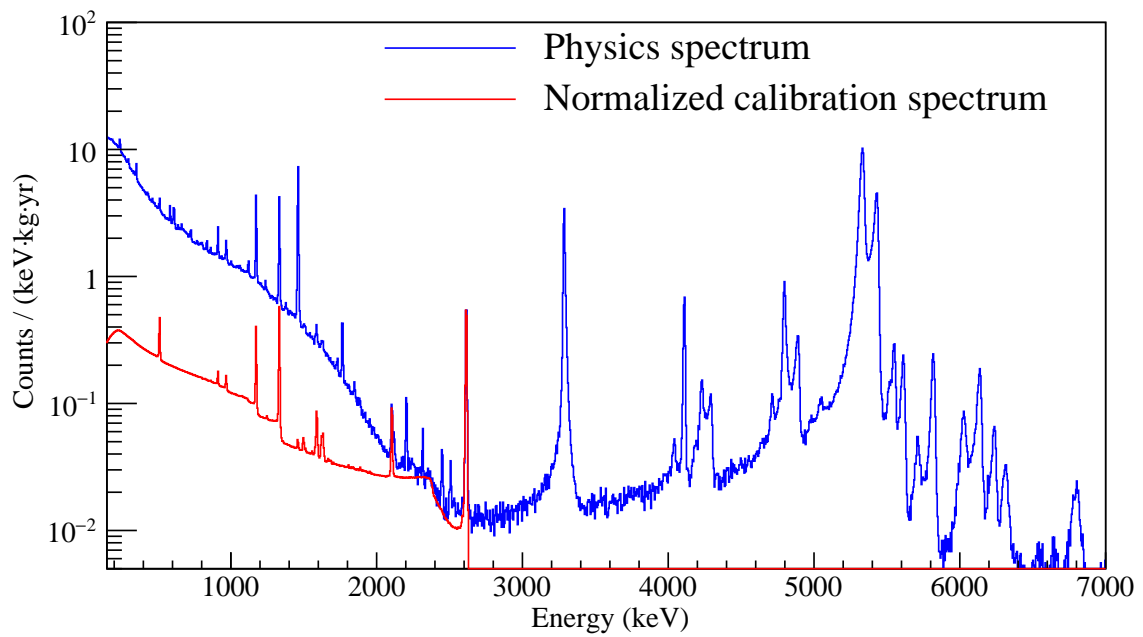


Figure 3.12: CUORE physics spectrum from DS3606 – DS3615 with corresponding calibration spectrum normalized to the 2615 keV gamma line.

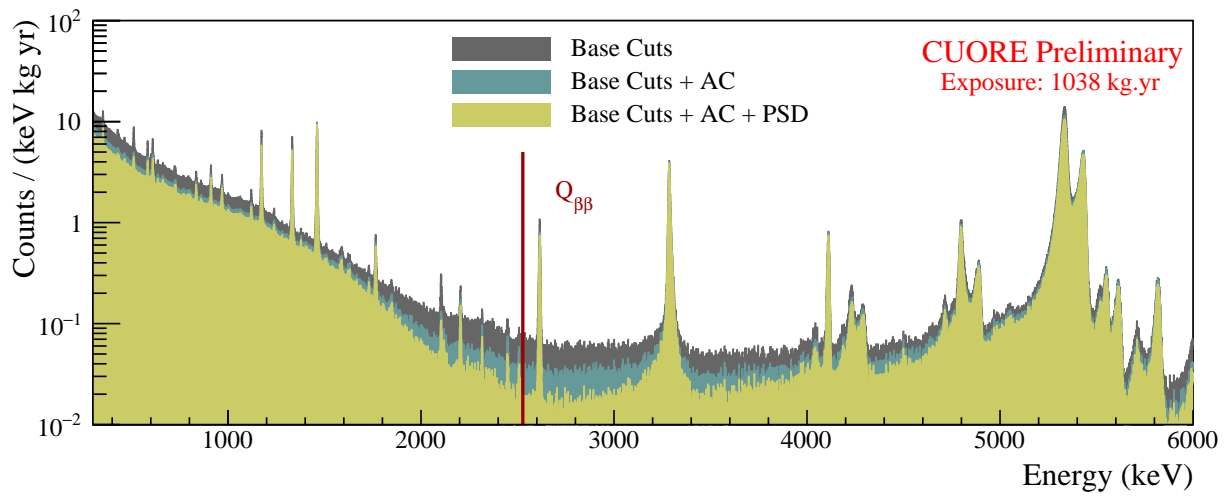


Figure 3.13: Result of using cuts on the CUORE physics spectrum corresponding to DS3601 – DS3615. Base Cuts are based on the analysis sequences and only pass events that contain one signal pulse, AC (anti-coincidence) corresponds to the $0\nu\beta\beta$ decay multiplicity cut, and PSD corresponds to pulse shape discrimination cuts. The vertical line labeled $Q_{\beta\beta}$ corresponds to the Q-value of ^{130}Te double-beta decay.

CHAPTER 4

Background model

4.1 Introduction

Our expected experimental sensitivity relies heavily on the background rate in the $0\nu\beta\beta$ decay ROI, 2490 keV – 2575 keV. The main contribution to the background in the $0\nu\beta\beta$ decay ROI are degraded alpha events, partial energy depositions from ~ 3 MeV – 10 MeV alpha particles measured in our detector. In this chapter, we discuss the background model we are developing to describe our physics data in the *alpha energy region*. This energy region corresponds to background almost exclusively from alpha decays in the decay chains of the long-lived ^{238}U and ^{232}Th . As discussed in Chapter 1, these naturally occurring, long-lived background sources are essentially unavoidable, but can be controlled with mitigation techniques such as materials screening and selection for radiopurity, ultra-clean materials handling, and shielding. CUPID, a proposed upgrade of CUORE, will be able to improve our sensitivity by discriminating alpha events, however the environmental background will still be present to produce the associated gamma and beta background events in our data. For this reason, we study the alpha background in CUORE to develop a way to identify and constrain this pervasive source of background.

Studying the alpha background is further motivated by its unique property to distinguish background source locations. The short range of the alpha particle (~ 10 μm in TeO_2 and ~ 15 μm in copper for 5 MeV α particles) restricts the possible locations of alpha background sources in that we can only detect alpha decay radiation from: deep inside the crystal (crystal *bulk contamination*), the surface of the crystal (crystal *surface contamination*), and the surfaces of structures directly facing the crystals. The alpha background locations can be

distinguished by considering the alpha decay process and event multiplicities. In the alpha decay process:



the parent nucleus, X with mass number A and atomic number Z , decays via alpha emission to the recoil nucleus, Y . From Equation 4.1, both M1 and M2 events can be detected since two particles are emitted from the decay. The energies of the two particles are characteristic of the alpha decay and its Q-value and can be used to identify the parent nucleus and its location. Considering only the alpha energy region:

- The peaks in the **M1** spectrum correspond to either the full energy (Q-value) of an alpha decay deep inside the crystal (see alpha decay **1** in Figure 4.1) or the energy of the alpha particle, emitted from an alpha decay on the surface of a crystal or a nearby structure (see alpha decay **3** in Figure 4.1). In the case of the alpha peak, the nuclear recoil goes undetected or the energy it deposits in a neighboring crystal is below the low-energy threshold.
- The peaks in the **M2** spectrum correspond to the energy of an alpha particle emitted from alpha decay on the crystal surface (see alpha decays **2** in Figure 4.1). In this case, the nuclear recoil energy is also detected with energy greater than the low-energy threshold, but in a different crystal.
- The peaks in the **M2Sum** spectrum correspond to the full energy (Q-value) of an alpha decay as the sum of the alpha particle energy and nuclear recoil energy deposited in two different crystals from alpha decay on the surface of one of the crystals (see alpha decays **2** in Figure 4.1).

The detailed shape of the structures in the alpha background is used to infer the contamination depth. In Figure 4.2, simulations of various ${}^{210}\text{Po}$ contamination locations and depths are shown as an example. Contaminations in and on the TeO_2 crystal and on the surface of the copper tower support structure all contribute to M1 in panel (a). In M1, the low-energy alpha tail structure corresponds to copper surface contaminations and the shape

of this low-energy tail is used to constrain the depth of the copper contamination. The two-peak structures in M1 correspond to shallow crystal surface contamination. The alpha peak on the left corresponds to energy depositions from the alpha particle only and the Q-value peak on the right corresponds to energy depositions from both the alpha particle and nuclear recoil in the same crystal. The ratio of Q-value peak and alpha peak events in this structure is used to constrain the depth of the shallow crystal surface contamination. The single peak structure in M1 corresponds to deep surface or bulk crystal contamination. The shape of the peak does not change with depth, so M1 cannot differentiate deep depth sources from bulk contamination. Only contaminations on the TeO₂ crystal surface contribute to the M2 and M2Sum spectra in panels (b) and (c), respectively. Peaks in both spectra correspond to crystal surface contamination. In the M2 spectrum, a peak corresponds to shallow surface contamination and a low-energy tail structure corresponds to deep surface crystal contamination. The shape of the low-energy tail in M2 is used to constrain the depth of deep crystal surface contamination, which could not be determined from M1. According to the simulations, the shape of the alpha (summed) peak does not change with depth in M2 (M2Sum), so the spectrum does not provide depth information for shallow crystal surface contamination (any surface contamination). This detailed behavior is used to guide the construction of our background model discussed in Section 4.4.

4.2 Alpha background spectra

Only DS3606 – DS3615 are used in this analysis; datasets taken before 2019 were omitted to exclude the effect of detector configuration differences on the energy reconstruction and shape of the physics spectrum. We further limited our investigation of the alpha background sources to the crystals and tower structures by excluding the outermost crystals (see Figure 4.3), although the alpha background spectra corresponding to the different crystal geometries do not change significantly (see Figure 4.4). For comparison, the spectra from the gamma-dominated energy region corresponding to the different crystal geometries are shown in Figure 4.5. In this section, we identify the characteristic alpha decay peaks in our physics

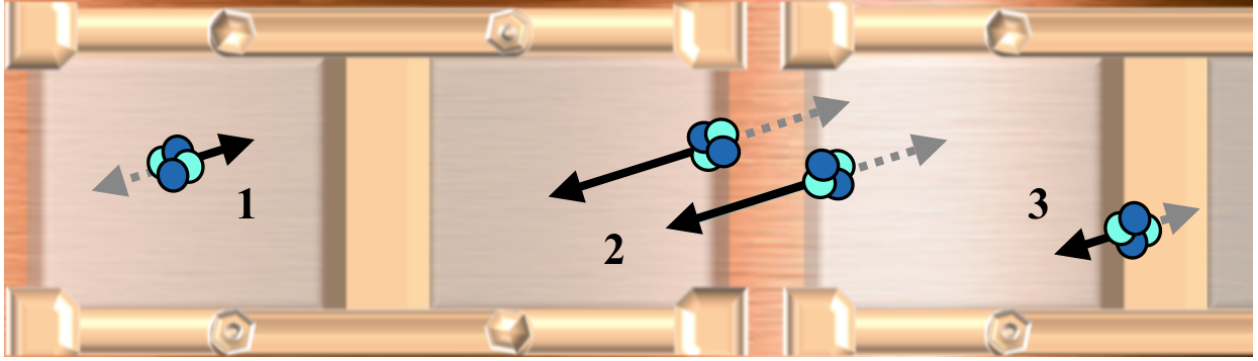


Figure 4.1: Schematic of alpha decays that contribute to the alpha energy region. Location of alpha decay is denoted by the alpha particle, alpha energy deposition location is denoted by the solid, black arrow, and nuclear recoil energy deposition location is denoted by the dashed, grey arrow. **1** corresponds to crystal bulk contamination: both the alpha particle and recoil nucleus deposit their energies in the same crystal resulting in an M1 event. **2** corresponds to crystal surface contamination: the recoil nucleus (alpha particle) deposits its energy in the source crystal and the alpha particle (recoil nucleus) escapes and deposits its energy in a different crystal resulting in a pair of M2 events and a corresponding M2Sum event. **3** corresponds to copper surface contamination: the nuclear recoil energy is not detected as it is deposited in the copper frame and the alpha particle escapes and deposits its energy in a crystal resulting in an M1 event.

data; the corresponding background sources were included in our model.

The spectra in Figure 4.6 – Figure 4.8 correspond to the M1, M2 and M2Sum spectra used in this analysis. The characteristic peaks of these background sources are identified in Table 4.1 – Table 4.3 where the Peak Index in the first column corresponds to the index labels in the figures. From the spectra, the long-lived ^{238}U and ^{232}Th decay chains are the main sources of background in the alpha energy region, with ^{190}Pt being the only exception. Unlike the contamination from the radioactive decay chains that occur naturally, the ^{190}Pt contamination likely comes from the platinum crucibles used in the crystal growth process. Background sources contributing to crystal surface contaminations are identified by the peaks in the M2 and M2Sum spectra, but detailed simulations are required to disentangle their contamination depths, as well as crystal bulk and copper tower surface contaminations from

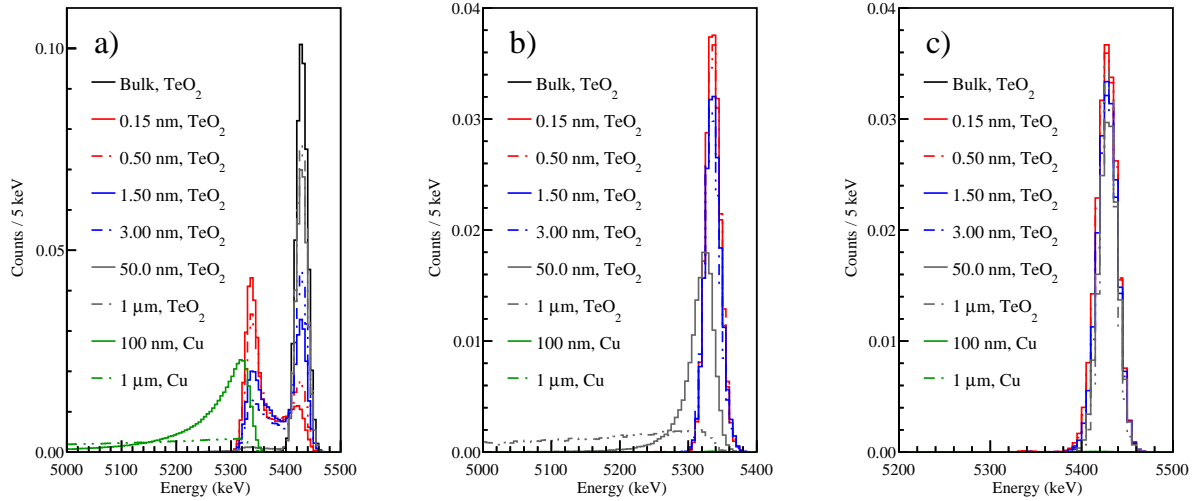


Figure 4.2: Simulations of the possible detected alpha decay contaminations and their contributions to the different multiplicity spectra. a) corresponds to the M1 spectrum. b) corresponds to the M2 spectrum. c) corresponds to the M2Sum spectrum.

the M1 spectrum.

The isotopes in the ^{238}U and ^{232}Th decay chains are shown in Figure 4.9 along with their decay modes and half-lives. Some characteristic peaks from the alpha decays of these decay chains are absent from the spectra. The peaks from ^{212}Po and ^{214}Po are outside the energy range with reasonable statistics and are excluded in the figures. The Q-value peaks of ^{216}Po and ^{220}Rn are absent in the M1 spectrum due to the short half-life of ^{216}Po to ^{220}Rn that results in a pile-up event.

4.3 Simulations

In this section, we discuss our simulations of radioactive contaminations in our detector and the detector response.

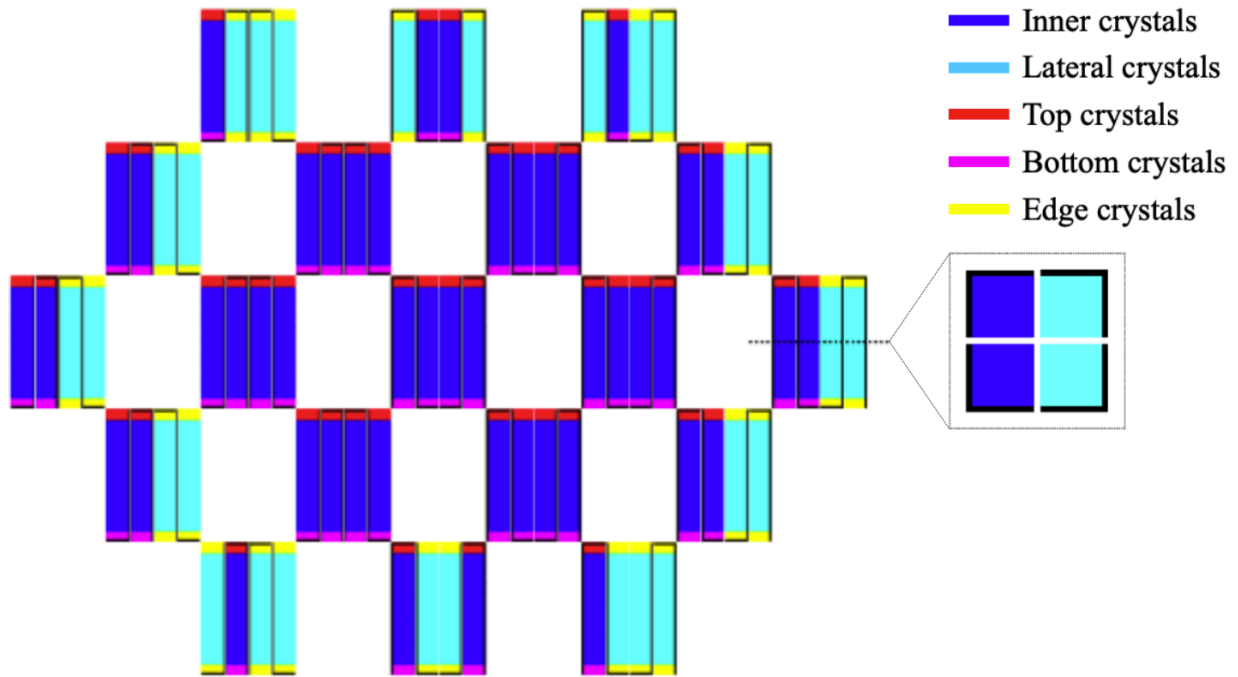


Figure 4.3: Schematic of CUORE’s 19 towers reflecting the different crystal geometries. The relative column positions are denoted by the solid black lines representing the tower corners from a top-down perspective. Five crystal geometries are highlighted: inner crystals, lateral crystals, top crystals, bottom crystals, and top/bottom edge crystals. The inner crystals are mainly exposed to the other crystals and the tower structures. In addition to the detector structure, the lateral crystals are exposed to the 10 mK copper tiles; the top crystals are exposed to the top copper plate; the bottom crystals are exposed to the bottom copper plate; and the edge crystals are exposed to the 10 mK copper tiles and the top/bottom copper plate.

4.3.1 qshields

The CUORE simulation code, *qshields*, is based on the Geant4 toolkit, version 10.05 [36]. *qshields* includes a model of all the major structures of CUORE, including its 19 towers of TeO_2 crystals, multiple copper cryostat vessels, and various shielding with enough detail to represent the effects of the particle interactions within the system. The model geometry of CUORE is shown in Figure 4.12. Volumes of the same material and function are combined into *elements*. Elements that are directly exposed to the TeO_2 crystals are listed in Table

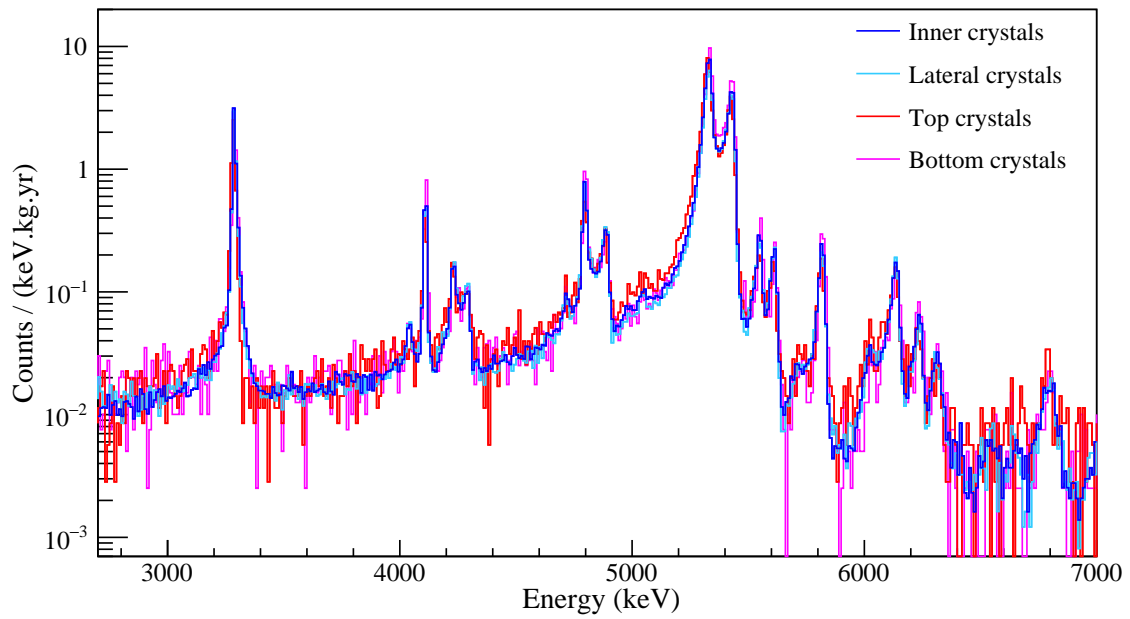


Figure 4.4: Comparison of alpha background spectra from different crystal geometries.

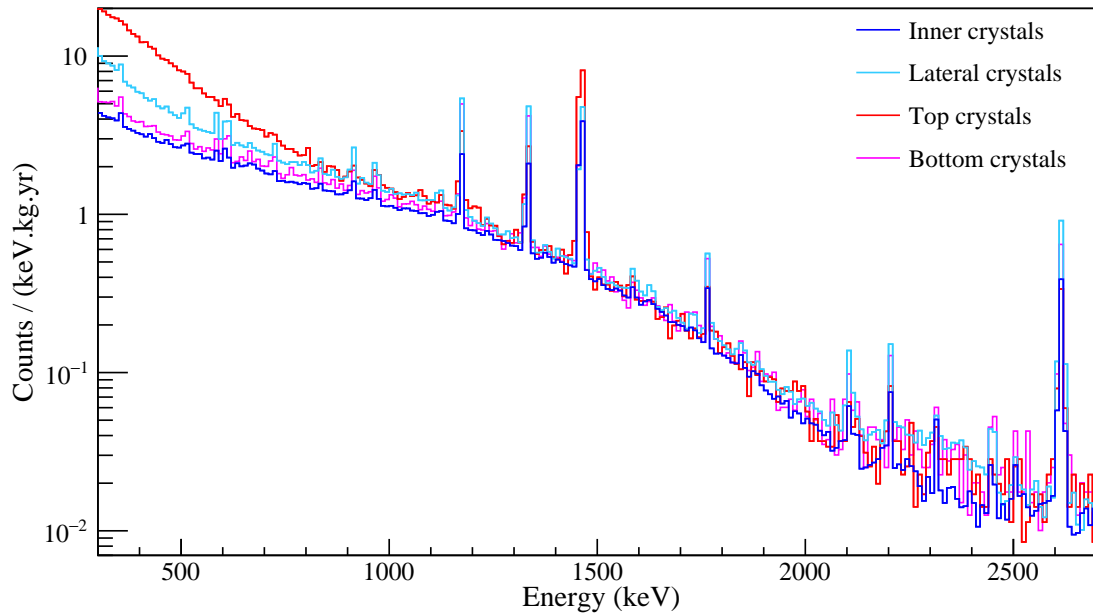


Figure 4.5: Comparison of gamma background spectra from different crystal geometries.

4.4 with their qshields volumes, surface areas, and masses.

In a typical qshields simulation, a radioactive source, an element, and a contamination

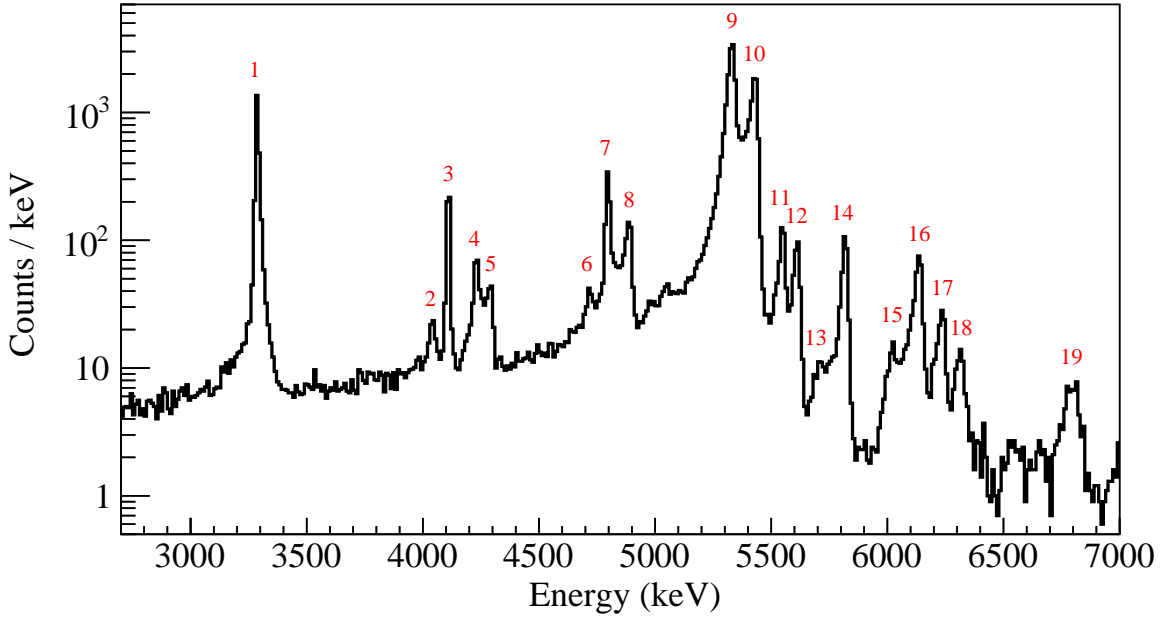


Figure 4.6: M1 spectrum. The background source contributions to the indexed peaks are in Table 4.1.

type are specified. The radioactive source can be a particle with a user-specified energy spectrum or a user-defined decay chain. The *contamination type* determines the source distribution in the element and can be specified as either bulk or surface. When the bulk option is specified, the source position is sampled from a uniform distribution across the full volume of the element. The source position distribution of bulk contamination in the TeO₂ crystals is shown as an example in Figure 4.10. When the surface contamination option is specified, the source position distribution is an exponential profile with a user-specified characteristic depth. The source position distribution of surface contaminations on the copper tower structure is shown as an example in Figure 4.11.

qshields also requires the number of source particles or decay chains to simulate. With this information, qshields can generate and transport the source particles and any secondaries through the model. If a particle loses energy through interactions in the crystals, the deposited energy, assigned crystal number, and relative time between energy depositions belonging to the same source particle (or decay chain) are stored as a Monte Carlo (MC)

Table 4.1: Source of characteristic peaks in the M1 spectrum [34].

Peak Index	Source(s)	Decay Chain	Nominal Energy (keV)
1	^{190}Pt Q-value	–	3249
2	^{232}Th Alpha	^{232}Th	4012.3
3	^{232}Th Q-value	^{232}Th	4081.6
4	^{238}U Alpha	^{238}U	4198
5	^{238}U Q-value	^{238}U	4269.7
6	^{230}Th Alpha	^{238}U	4687.0
	^{230}Th Q-value	^{238}U	4770.0
7	^{234}U Alpha	^{238}U	4774.6
	^{226}Ra Alpha	^{238}U	4784.34
	^{234}U Q-value	^{238}U	4859.8
8	^{226}Ra Q-value	^{238}U	4870.62
9	^{210}Po Alpha	^{238}U	5304.33
10	^{210}Po Q-value	^{238}U	5407.45
	^{222}Rn Alpha	^{238}U	5489.48
11	^{228}Th Q-value	^{232}Th	5520.08
12	^{222}Rn Q-value	^{238}U	5590.4
13	^{224}Ra Alpha	^{232}Th	5685.37
14	^{224}Ra Q-value	^{232}Th	5788.87
15	^{218}Po Alpha	^{238}U	6002.35
	^{212}Bi Alpha	^{232}Th	6050.78
16	^{218}Po Q-value	^{238}U	6114.68
18	^{212}Bi Q-value	^{232}Th	6207.26
18	^{220}Rn Alpha	^{232}Th	6288.08
19	^{216}Po Alpha	^{232}Th	6778.3

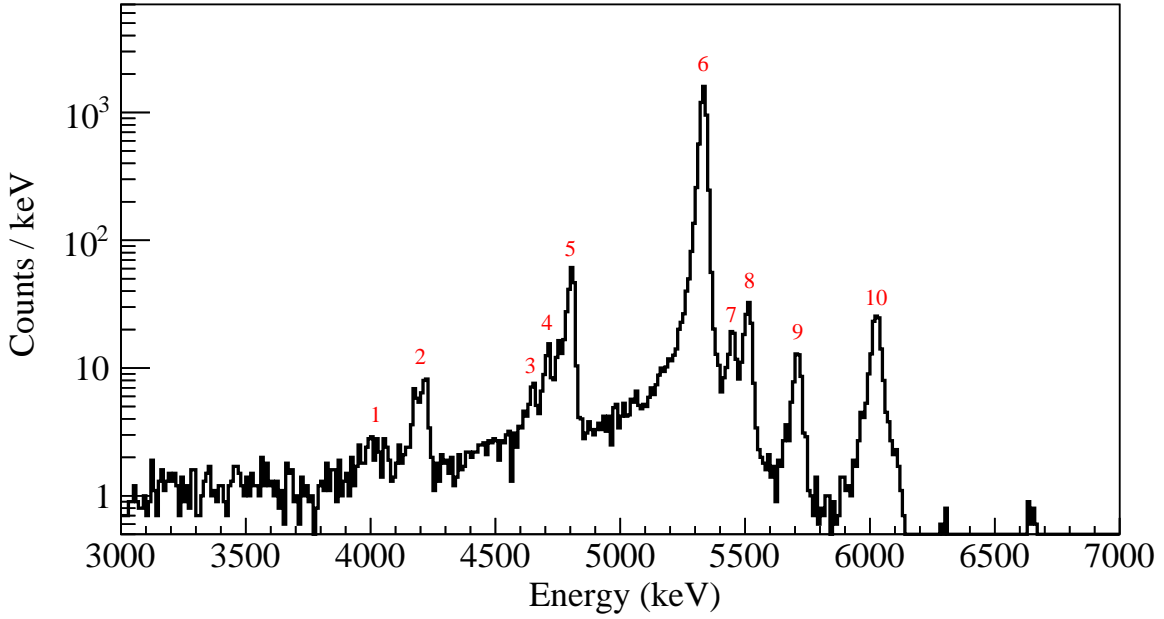


Figure 4.7: M2 spectrum. The background source contributions to the indexed peaks are in Table 4.2.

simulated event. For simulated decay chains, when the relative time between decays exceed a user-defined threshold, the position of the daughter is resampled based on the contamination type. Resampling the source position circumvents the unlikely scenario that a full decay chain is measured within a given dataset.

4.3.2 g4cuore

An auxiliary C++ code, `g4cuore`, convolves the ideal MC events with intrinsic and analysis-based detector parameters. The intrinsic detector parameters include the particle-dependent quenching factors and energy and temporal resolutions. The timing characteristics of the detector is simulated by applying a 5 ms integration window, corresponding to the temporal resolution of the bolometer, and a 0.75 s trigger dead time. Implementation of the energy reconstruction detector parameters are discussed in Sections 4.3.2.1 and 4.3.2.2. The analysis-based parameters are described in Chapter 3 as analysis cuts. In this analysis, `g4cuore` implements the low-energy threshold (70 keV), the coincidence time (30 ms), the distance

Table 4.2: Source of characteristic peaks in the M2 spectrum [34].

Peak Index	Source(s)	Decay Chain	Nominal Energy (keV)
1	^{232}Th Alpha	^{232}Th	3947.2
	^{232}Th Alpha	^{232}Th	4012.3
2	^{238}U Alpha	^{238}U	4198
3	^{226}Ra Alpha	^{238}U	4601
	^{230}Th Alpha	^{238}U	4620.5
4	^{230}Th Alpha	^{238}U	4687.0
5	^{234}U Alpha	^{238}U	4722.4
	^{234}U Alpha	^{238}U	4774.6
	^{226}Ra Alpha	^{238}U	4784.34
6	^{210}Po Alpha	^{238}U	5304.33
7	^{228}Th Alpha	^{232}Th	5423.15
8	^{222}Rn Alpha	^{238}U	5489.48
9	^{224}Ra Alpha	^{232}Th	5685.37
10	^{218}Po Alpha	^{238}U	6002.35
	^{212}Bi Alpha	^{232}Th	6050.78
	^{212}Bi Alpha	^{232}Th	6089.88

threshold (150 mm), pile-up (3 s pre-trigger, 7 s post-trigger), and geometric cuts (inner crystal). In addition, dataset-dependent cuts are applied by assigning one of the datasets to each MC event. The relative number of events assigned to each dataset is based on the relative exposure of the datasets. With the dataset assigned, a PCA cut is applied based on the dataset-dependent PCA efficiency. The only other dataset-dependent cut applied is the cut on the channels that did not pass any part of the analysis sequence; dataset-channels that were cut during the analysis were also removed from the simulation.

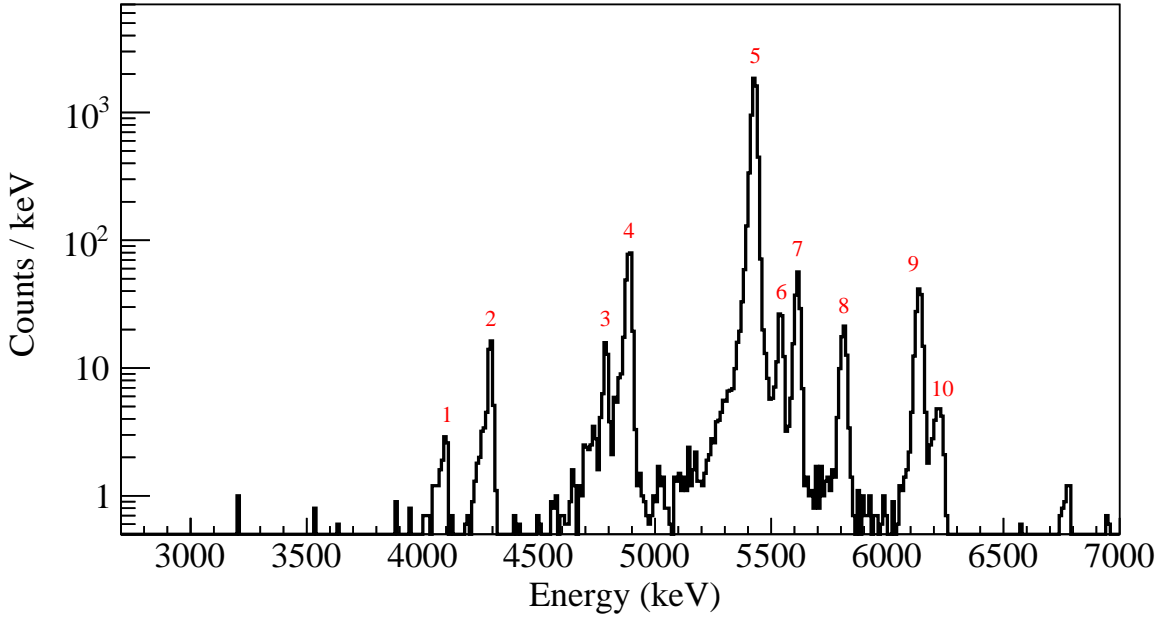


Figure 4.8: M2Sum spectrum. The background source contributions to the indexed peaks are in Table 4.3.

4.3.2.1 Energy quenching

The measured peak positions in the alpha energy region are reconstructed at higher energies compared to their nominal values in our TeO_2 bolometers. We describe this difference in response between gamma and alpha energy depositions as *quenching*. Quenching may be in part caused by our calibration scheme since we only use gamma lines for energy reconstruction (see Section 3.2). Although the energy quenching mechanism is not yet understood, a particle-dependent *quenching factor* is applied to the MC event energy to simulate the detector response.

The quenching factor is a multiplicative factor equal to the ratio of the measured energy and nominal energy of a decay. Figure 4.13 shows the effect of applying appropriate quenching factors to simulations of surface and bulk contaminations of the simulated $^{228}\text{Ra} - ^{208}\text{Pb}$ sub-decay chain. The quenching factors corresponding to surface contaminations were obtained by considering the peak positions in the M2 and M2Sum spectra. The peaks in the M2 spectrum correspond to the alpha energies of the decay only, so they were used first to

Table 4.3: Source of characteristic peaks in the M2Sum spectrum [34].

Peak Index	Source(s)	Decay Chain	Nominal Energy (keV)
1	^{232}Th Q-value	^{232}Th	4081.6
2	^{238}U Q-value	^{238}U	4269.7
3	^{230}Th Q-value	^{238}U	4770.0
4	^{234}U Q-value	^{238}U	4859.8
	^{226}Ra Q-value	^{238}U	4870.62
5	^{210}Po Q-value	^{238}U	5407.45
6	^{228}Th Q-value	^{232}Th	5520.08
7	^{222}Rn Q-value	^{238}U	5590.4
8	^{224}Ra Q-value	^{232}Th	5788.87
9	^{218}Po Q-value	^{238}U	6114.68
10	^{212}Bi Q-value	^{232}Th	6207.26

determine the alpha particle quenching factor. We found that using this quenching factor for both the alpha particles and recoil nuclei did not reproduce the positions of the Q-value peak in the M1 spectrum nor the corresponding summed peak in the M2Sum spectrum, so we used the M2Sum spectrum to determine the quenching factor for the nuclear recoils. The peaks in the M2Sum spectrum correspond to the sum of the energies of the alpha particles and recoiling nuclei from the decay, so the quenching factor for the recoil particles was determined from the M2Sum peaks after applying the alpha particle quenching factor obtained using the M2 spectrum. Using the quenching factors found from surface contaminations, we found the peak positions of bulk contaminations were not properly reproduced, so the quenching factors corresponding to bulk contaminations were obtained by considering the Q-value peak positions in the M1 spectrum. For crystal bulk contaminations, the same quenching factor is used for both the alpha particle and recoil nucleus since the particle-dependent energy depositions cannot be distinguished from the data.

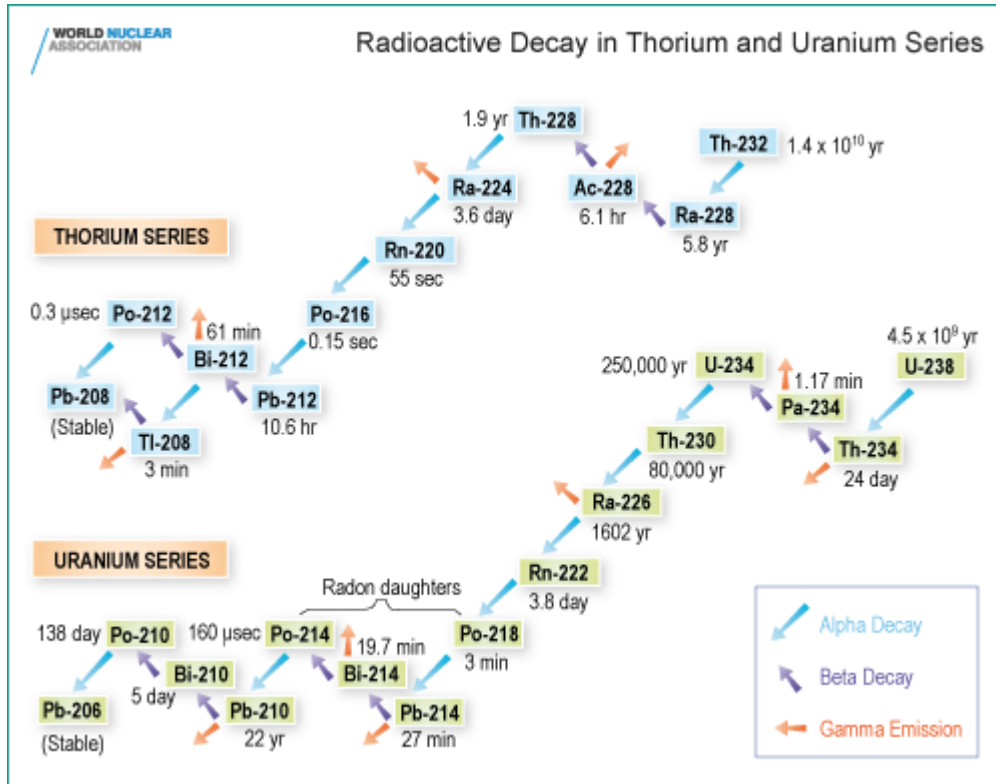


Figure 4.9: Figure from [35]. Radioactive decay chains contributing to the background in the alpha region.

Some alpha decay structures required additional considerations. The alpha peak in the M2 spectrum of ^{232}Th , shown in panel (b) of Figure 4.17, did not have enough statistics to determine its peak position, so the alpha peak in the M1 spectrum, shown in panel (a) of the same figure, was used instead. In the case of ^{238}U , we found that the relative amplitudes of the primary and secondary alpha peaks in the simulated M2 spectrum depended on the nuclear recoil quenching factor. Because its nuclear recoil energy is close to the 70 keV low-energy threshold, using too low a quenching factor would suppress M2 events in the primary alpha peak. An example of this effect is shown in Figure 4.14. In general, the different contamination simulations required different quenching factors. The quenching factors used in this analysis are listed in Table 4.5.

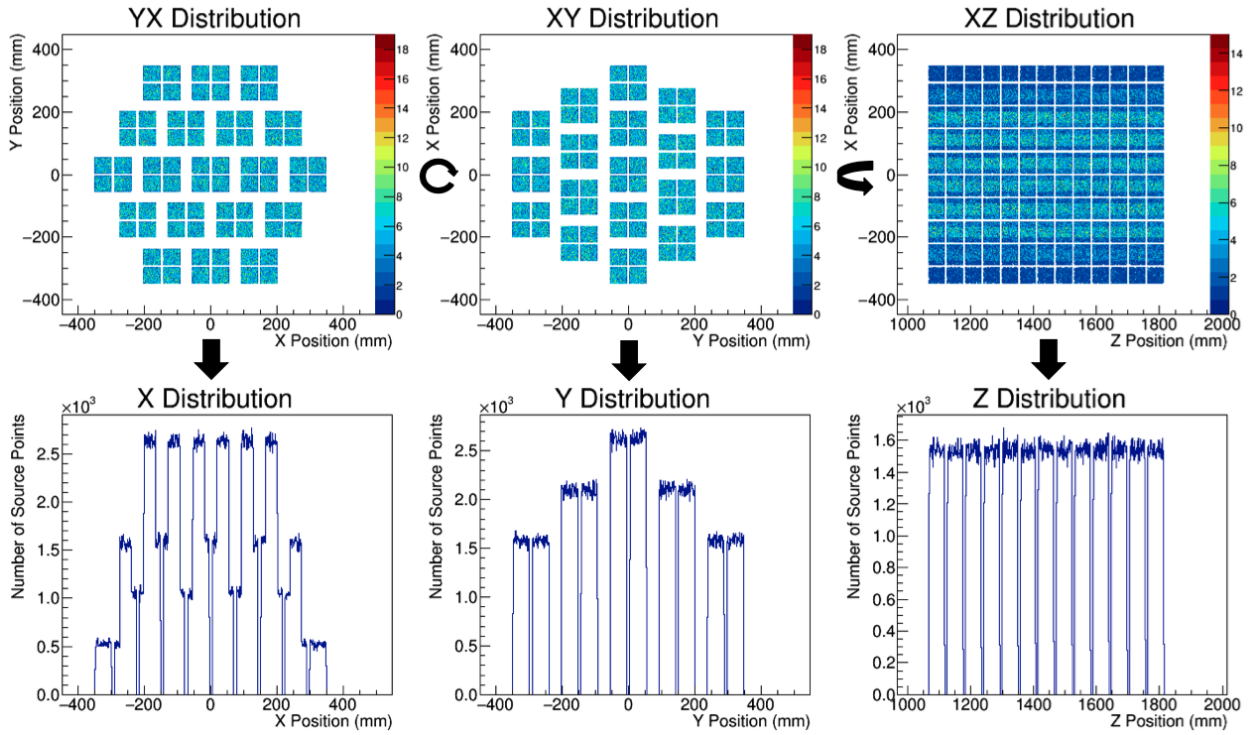


Figure 4.10: Simulated bulk contamination in the TeO_2 crystals. The top figures corresponds to the different 2D distributions of the source positions in the qshields coordinate system; their projections along their horizontal axes are shown directly below. For uniform source distributions, the number of source points generated are proportional to the material thickness.

4.3.2.2 Energy resolution

In order to simulate the detector energy resolution, `g4cuore` first applies the appropriate quenching factor to the energy from qshields, then smears the quenched energy with a Gaussian function. We chose to use a second-degree polynomial for the *resolution function*, which relates the full width half maximum (FWHM) of the Gaussian function to the energy deposition, to describe the data. In Figure 4.15, the data points come from fitting peaks in the background energy spectra to a Gaussian function. The quadratic fits of the data points in the figure represent the resolution functions we used in `g4cuore`. There are two resolution functions because we found that peaks corresponding to mainly bulk contamination generally had better energy resolution.

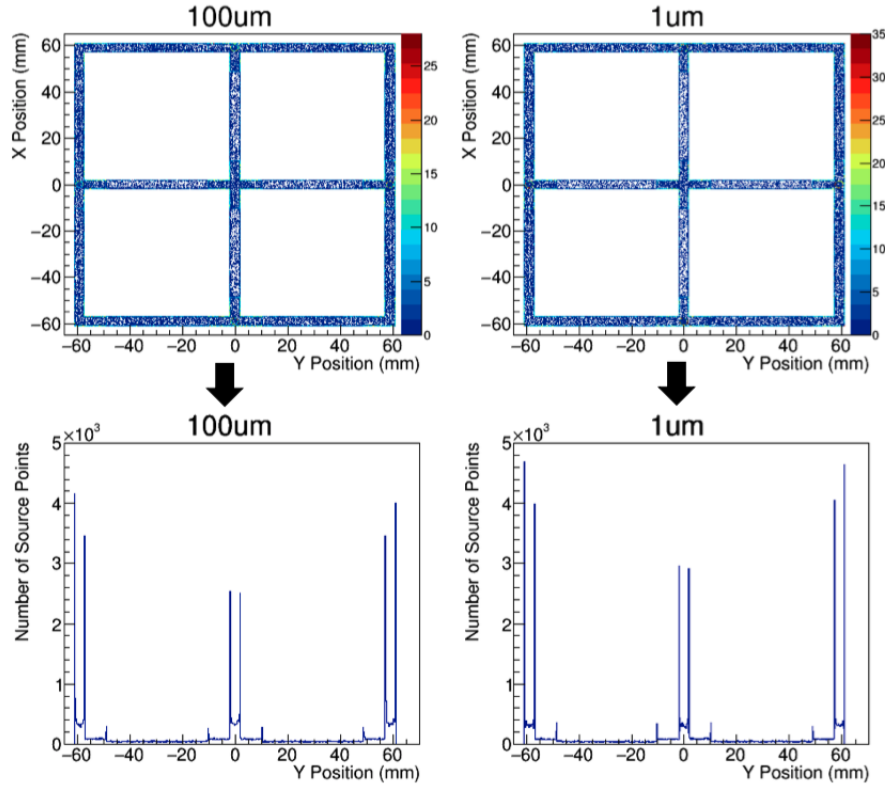


Figure 4.11: Simulated surface contaminations on the copper tower structure. The top figures corresponds to 2D distributions of the source positions in the qshields coordinate system; their projections along their horizontal axes are shown directly below. The figures on the left correspond to a characteristic depth of $100 \mu\text{m}$ and the figures on the right correspond to a characteristic depth of $1 \mu\text{m}$. For shallower characteristic depths, more source points are generated closer to the surface.

4.4 Bayesian model

As discussed in Section 4.3, we are able to simulate detected energy spectra of radioactive contaminations at various locations and depths in the CUORE detector. Our background model is a linear combination of the simulated energy spectra from the radioactive contaminations discussed in 4.4.1. This analysis uses the Bayesian Analysis Toolkit (BAT) software package to determine the contribution of each contamination. With respect to Bayes' theorem:

$$p(\boldsymbol{\theta}|\mathbf{X}^0) \propto \mathcal{L}(\mathbf{X}^0|\boldsymbol{\theta})p(\boldsymbol{\theta}) \quad (4.2)$$

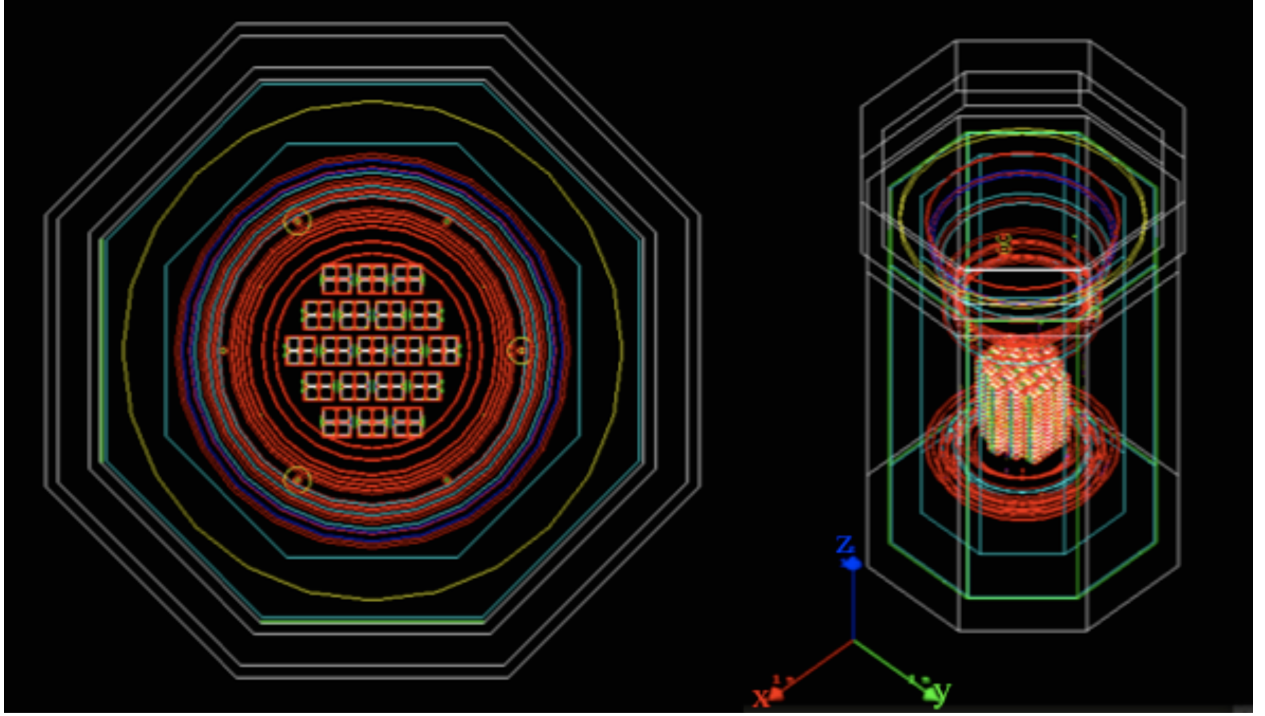


Figure 4.12: Left: Wire-frame, top-down view of qshields geometry. Right: Wire-frame, high-angle view of qshields geometry.

where $\boldsymbol{\theta}$ and \mathbf{X}^0 are vectors of the model parameter and observed data,

- $p(\boldsymbol{\theta}|\mathbf{X}^0)$ is the posterior probability density function (pdf) of the model parameters given the observed data;
- $\mathcal{L}(\mathbf{X}^0|\boldsymbol{\theta})$ is the likelihood function; and
- $p(\boldsymbol{\theta})$ is the prior pdf of the parameter vector;

our model parameters are the normalization factors of the binned simulated spectra and our observed data is the binned physics spectrum comprised of DS3606 – DS3615 discussed in Section 4.2. We define our likelihood as a product of Poisson distributions over bins and multiplicity spectra:

$$\mathcal{L} = \prod_{i=1}^{N_{\mathcal{M}}} \prod_{j=1}^{N_{bins}} \frac{\nu_{ij}^{n_{ij}}}{n_{ij}!} e^{-\nu_{ij}} , \quad (4.3)$$

Table 4.4: Mass, volume, and surface area of simulated volume elements near or comprising the detector.

Element	Volume (cm ³)	Surface (cm ²)	Mass (g)
10 mK Copper Shield	36691.1	67152.5	328752
(10 mK) Copper Tiles	1444.77	57820.4	12945
Copper Up Plate	664.28	13336.2	5952
Copper Bottom Plate	664.28	13336.2	5952
Internal Calibration Copper Tubes	119.39	2390.35	1070
TeO ₂ Crystals	123500	148200	741000
Copper Frames	5581.03	44322.8	50006
Copper Wire Trays	1285.33	27640.4	11517
Copper Wire Pads	5.85	1204.45	52.43
NTD Thermistors	8.60	288.50	45.75
PTFE Crystal Supports	1604.07	23121.1	3528.95

where $N_{\mathcal{M}}$ is the total number of multiplicity spectra used in the fit, N_{bins} is the total number of bins used in the fit, n_{ij} is the observed number of events in bin j of the multiplicity i spectrum, and ν_{ij} is the expectation value for bin j of the multiplicity i spectrum given by

$$\nu_{ij} = \sum_{k=1}^{N_{MC}} N_k \theta_{ijk} , \quad (4.4)$$

where N_{MC} is the total number of simulated contaminations used in the fit, N_k is a normalization factor related to the activity of the k^{th} MC spectrum and θ_{ijk} is the number of entries in bin j of the k^{th} MC multiplicity i spectrum. In BAT, we set uniform priors for each parameter, and chose the Metropolis-Hastings Markov Chain Monte Carlo (MCMC) algorithm to marginalize the posterior and the Minuit mode finder for optimization.

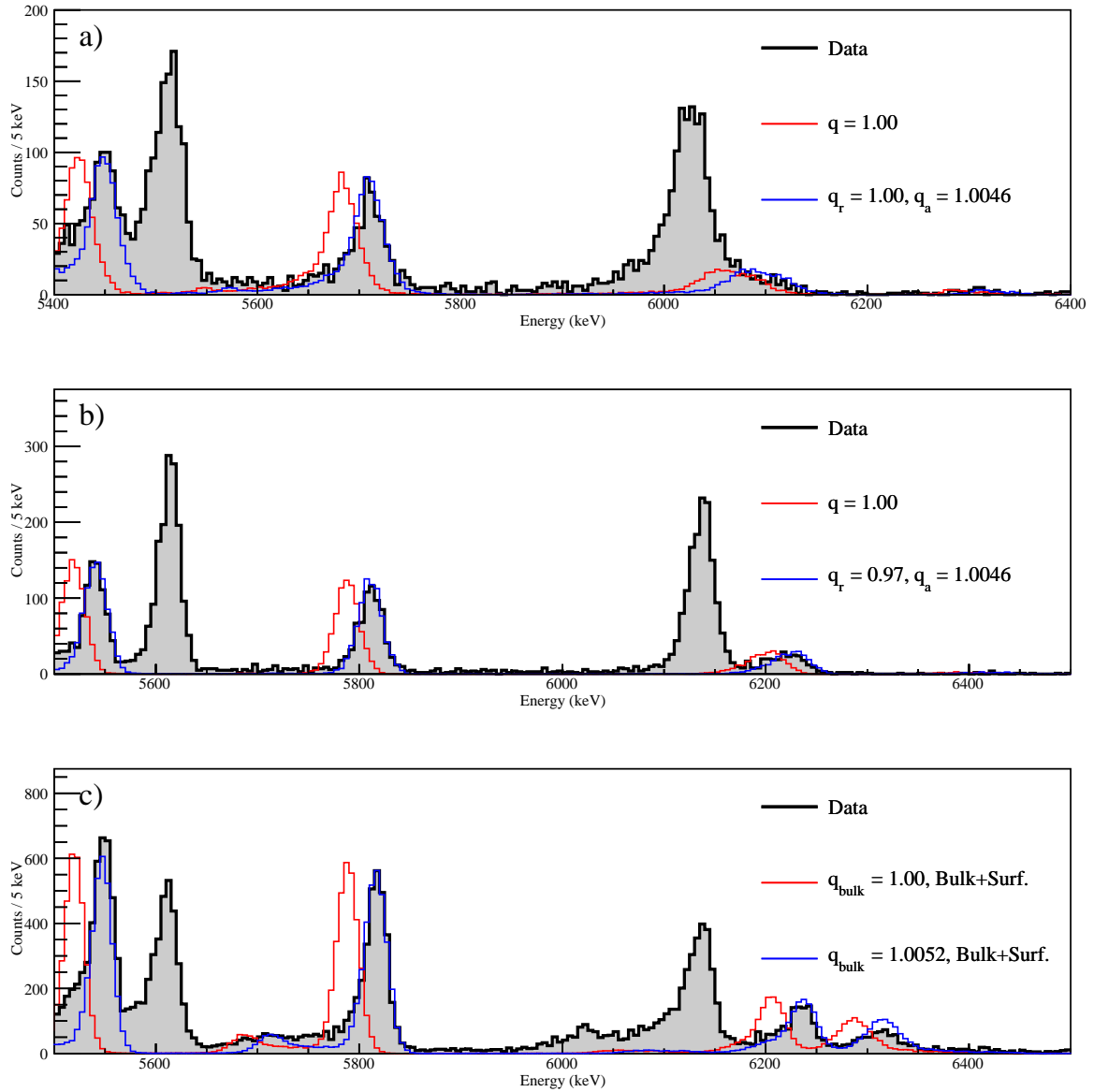


Figure 4.13: The effect of quenching on ^{228}Ra simulations. a) corresponds to the M2 spectrum, b) corresponds to the M2Sum spectrum, and c) corresponds to the M1 spectrum. The red spectrum corresponds to no applied quenching and the blue spectrum corresponds to the quenching applied in this analysis.

4.4.1 Determination of contamination depths

In the alpha energy region, the M1 spectrum contains events from contamination of the crystal surface and bulk, and surface contamination of the copper tower structures. With

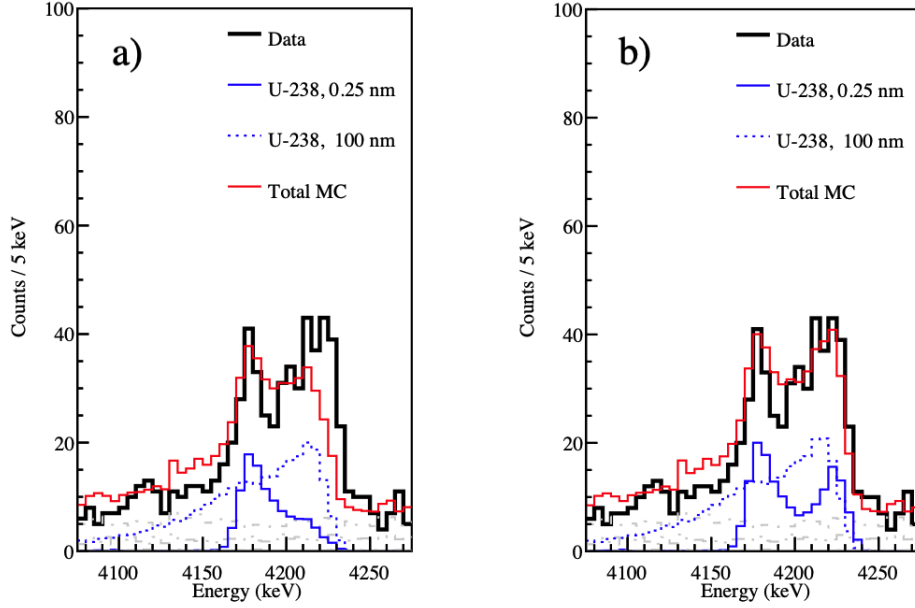


Figure 4.14: Comparison of ^{238}U simulations with different recoil quenching applied. a) M2 spectrum with recoil quenching value of 0.94. b) M2 spectrum with recoil quenching value of 0.97. The lower quenching value suppresses the contribution to the higher energy alpha peak because the quenched recoil energy is below the 70 keV energy threshold. The higher quenching value recovers M2 events in the high energy alpha peak.

respect to those three contamination locations, the M2 spectrum only contains events from crystal surface contamination, so it is used first to constrain the crystal surface contamination depth(s). The characteristic structures in the M2 spectrum are a Gaussian peak and its low-energy tail. The events in the peak are mostly due to shallow crystal surface contaminations (~ 1 nm), while the events in the tail are due to relatively deep crystal surface contamination(s). The slope of this tail is used to constrain the depth(s) of the deep crystal surface contamination(s). The shallow crystal surface contamination depth does not have an effect on the peak shape in the M2 spectrum, so the shape of the corresponding contribution in the M1 spectrum is used instead to constrain the depth of the shallow crystal surface contamination as described in Section 4.1.

After the crystal surface contaminations are found using the M2 spectrum, the corresponding contribution to the M1 spectrum can be used to constrain the remaining contribu-

Table 4.5: Implemented quenching factors.

MC Decay Chain	Depth	Recoil Quenching	Alpha Quenching
^{190}Pt Only	Bulk	1.0104	1.0104
^{232}Th Only	0.50 nm, 100 nm	0.88	1.0072
^{232}Th Only	Bulk	1.0070	1.0070
$^{228}\text{Ra} - ^{208}\text{Pb}$	0.50 nm, 100 nm	0.97	1.0046
$^{228}\text{Ra} - ^{208}\text{Pb}$	Bulk	1.0052	1.0052
$^{238}\text{U} - ^{230}\text{Th}$	0.25 nm, 100 nm	0.97	1.0066
^{230}Th Only	0.50 nm, 100 nm	0.89	1.0055
^{230}Th Only	Bulk	1.0054	1.0054
$^{226}\text{Ra} - ^{210}\text{Pb}$	0.5 nm, 100 nm	0.98	1.0040
$^{210}\text{Pb} - ^{206}\text{Pb}$	1 μm , 10 μm	0.92	1.0057

tion from contamination of the crystal bulk and tower structure surface. Considering the M1 spectrum, the crystal surface contaminations can contribute to both the alpha and Q-value peaks. We infer crystal bulk contamination from an excess of events at the Q-value peak that cannot be explained by the crystal surface contribution constrained by the M2 spectrum. We infer tower structure surface contamination from an alpha peak with a low-energy tail; we use the shape of this tail to constrain the contamination depth in the tower structure.

We compare the simulated spectra we selected to include in our model to the background spectra in Figure 4.16 – Figure 4.19. For each simulated spectrum, the normalization value used is the same across all multiplicities and figures. In each energy region, only significant crystal contaminations are highlighted, but the shown total MC spectrum includes all the selected simulated spectra.

In Figure 4.16, we show the energy regions corresponding to the ^{190}Pt peak. Panels (a), (b), and (c) correspond to the M1-, M2-, and M2Sum energy spectrum, respectively. Absence of peaks in the M2 and M2Sum spectra indicates no significant surface contamination from

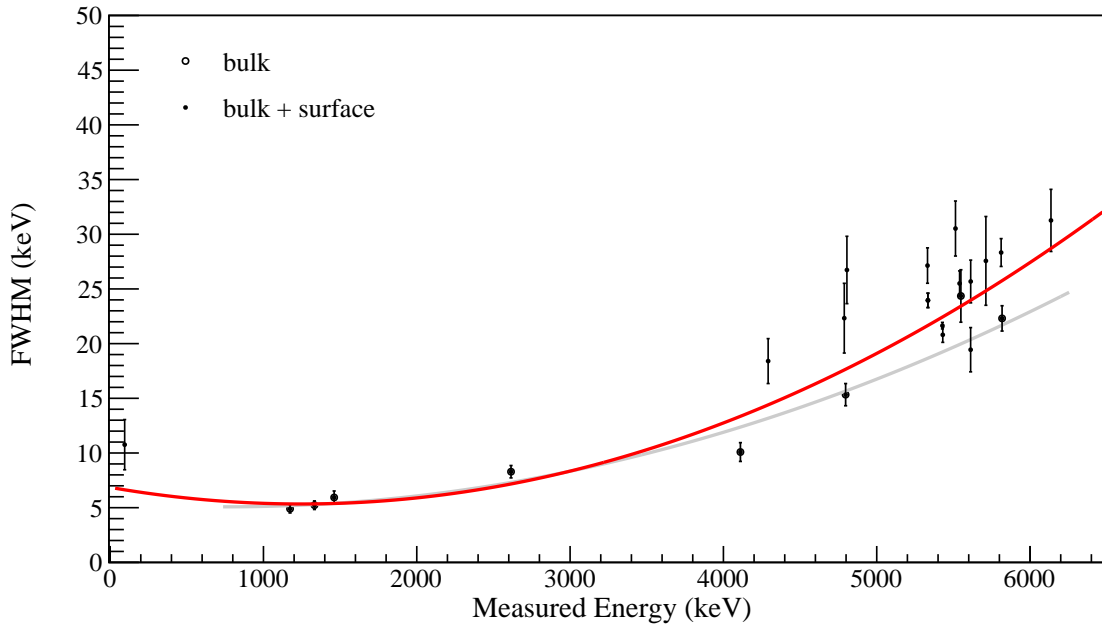


Figure 4.15: Resolution functions applied to surface and bulk contaminations in g4cuore. The data points come from fitting the peaks in the background energy spectra to a Gaussian function. Peaks corresponding to bulk contaminations generally have better energy resolution, so a different resolution function was applied to simulated bulk contamination events compared to surface events.

^{190}Pt , so only crystal bulk contamination of ^{190}Pt was selected for the background source. In the M1 spectrum, the high- and low-energy tails observed in the data peak are not reproduced by the simulation. The tails are likely caused by deformations in the pulse due to the origin of platinum in the crystals since aggressive PCA cuts have been shown to reduce the tails [37]. In the M2Sum spectrum, the peak in the data corresponds to the ^{208}Tl 583 keV and 2615 keV gamma lines in coincidence. In our model, a large bin is used for the ^{190}Pt peak since we cannot reproduce the detector response resulting in the tails in our simulations.

In Figure 4.17, we show the energy regions corresponding to the ^{232}Th peaks. Panels (a), (b), and (c) correspond to the M1-, M2-, and M2Sum energy spectrum, respectively. The peak in the M2Sum spectrum and the alpha peak in the M1 spectrum indicate at least one shallow surface contamination depth. In the M2 spectrum, the broad structure indicates an

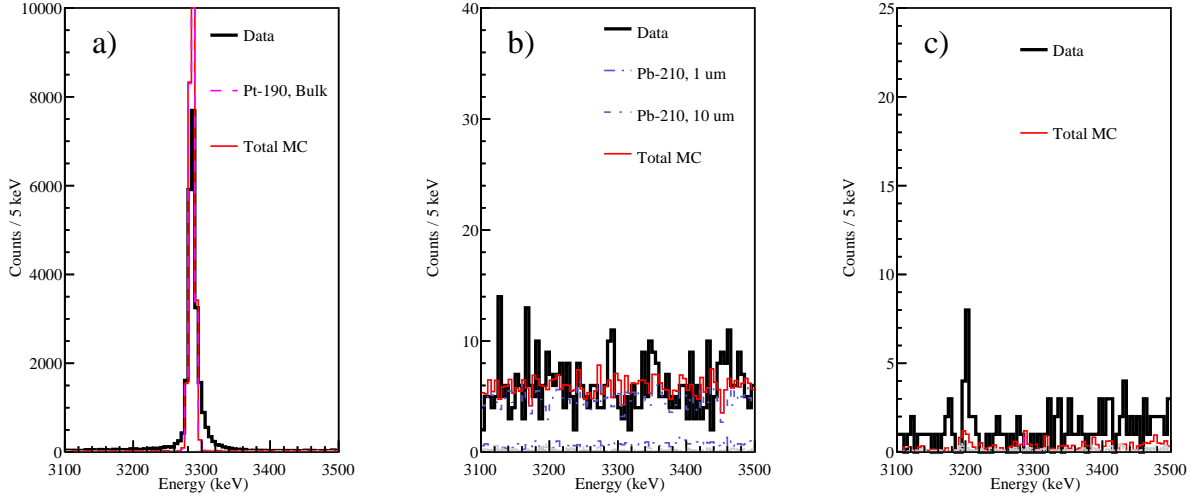


Figure 4.16: ^{190}Pt contamination. a) corresponds to the M1 spectrum, b) corresponds to the M2 spectrum, and c) corresponds to the M2Sum spectrum.

additional deeper crystal surface contamination depth. Due to low statistics, a characteristic depth of 100 nm was chosen for consistency with other simulated background sources. In the M1 spectrum, the amplitude of the Q-value peak indicates a bulk contamination. In the M2Sum spectrum, the low-energy shoulder is generally underestimated by the simulation; this will be discussed in Section 4.6.

In Figure 4.18, we show the energy regions corresponding to the ^{238}U peaks. Panels (a), (b), and (c) correspond to the M1-, M2-, and M2Sum energy spectrum, respectively. The peak and tail structures in the M2 spectrum indicate at least two crystal surface contaminations depths. In the M1 spectrum, the region between the alpha peak and Q-value peak is generally underestimated by the simulation; this will be discussed in Section 4.6.

In Figure 4.19, we show the alpha energy regions above the ^{210}Po peaks. Panels (a), (b), and (c) correspond to the M1-, M2-, and M2Sum energy spectrum, respectively. The alpha peaks in the M1 spectrum and the peaks in the M2 and M2Sum spectra indicate a shallow crystal surface contamination of the $^{228}\text{Ra} - ^{208}\text{Pb}$ and $^{226}\text{Ra} - ^{210}\text{Pb}$ sub-decay chains. The low-energy tails in the M2 spectrum indicate deep crystal surface contamination of both sub-decay chains. Low-energy alpha tails in the M1 spectrum indicate surface contamination on

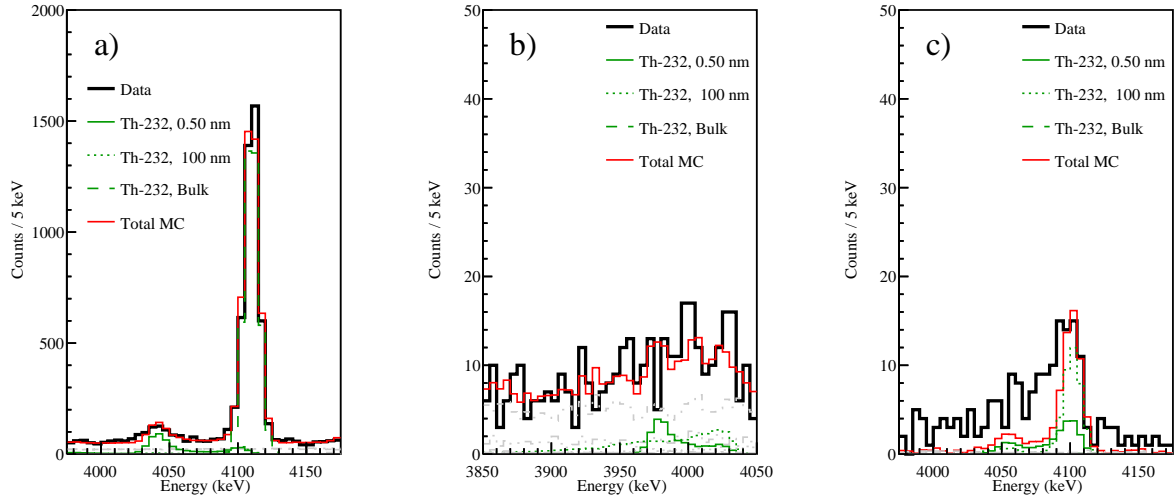


Figure 4.17: ^{232}Th contaminations. a) corresponds to the M1 spectrum, b) corresponds to the M2 spectrum, and c) corresponds to the M2Sum spectrum.

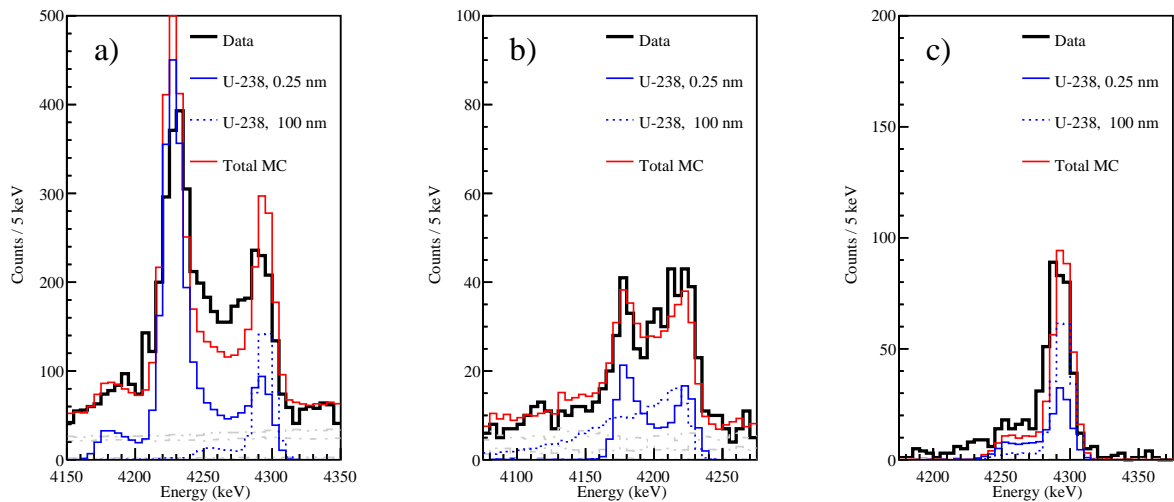


Figure 4.18: ^{238}U contaminations. a) corresponds to the M1 spectrum, b) corresponds to the M2 spectrum, and c) corresponds to the M2Sum spectrum.

the copper tower structures of both decay chains; a characteristic depth of 100 nm was selected for both. In the M1 spectrum, only the amplitudes of the Q-value peaks from the $^{228}\text{Ra} - ^{208}\text{Pb}$ sub-decay chain indicate bulk contamination.

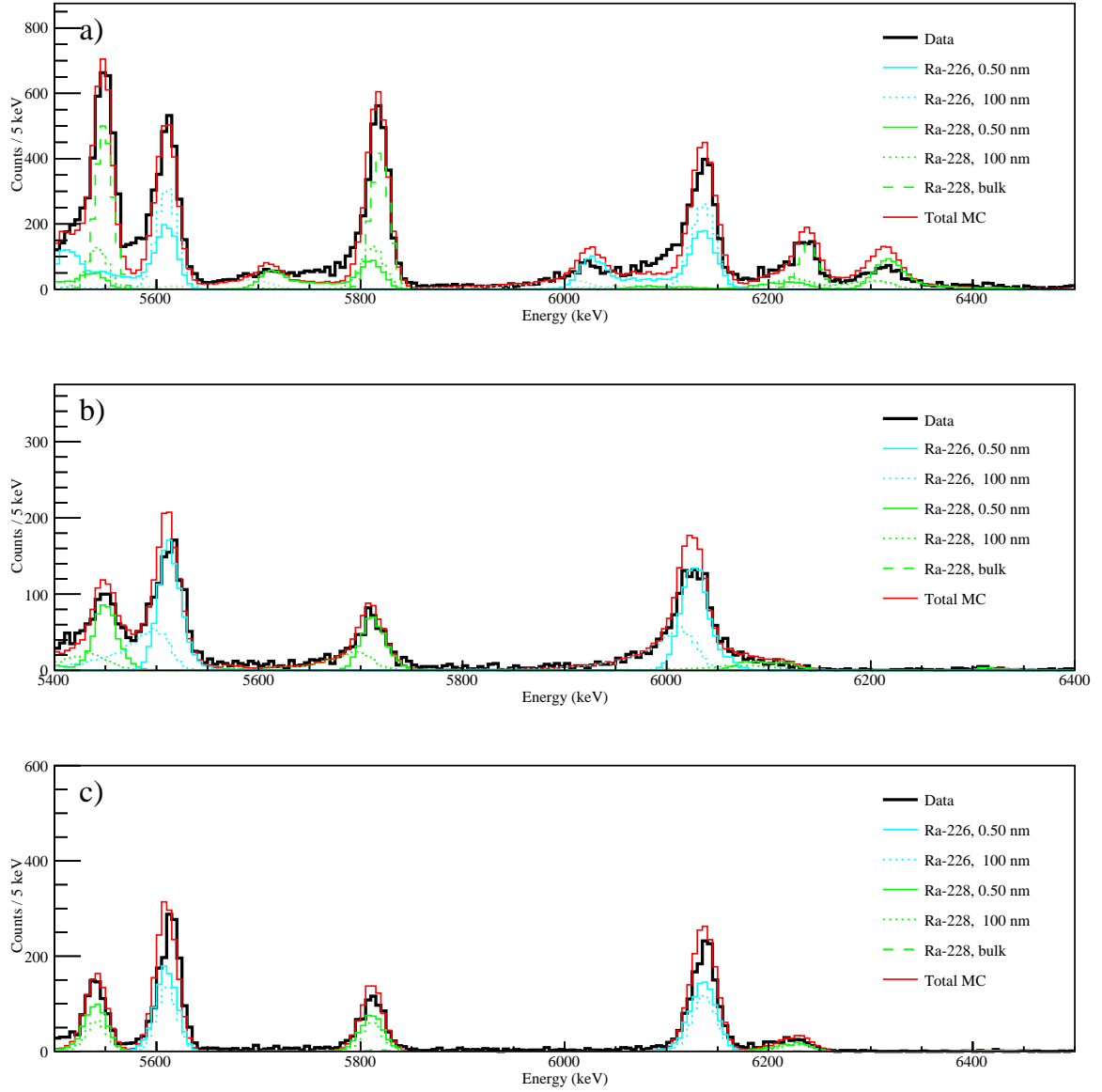


Figure 4.19: ^{228}Ra and ^{226}Ra contaminations. a) corresponds to the M1 spectrum, b) corresponds to the M2 spectrum, and c) corresponds to the M2Sum spectrum.

In Figure 4.20, we show the energy regions between the ^{238}U peaks and the ^{210}Po peaks. Panels (a), (b), and (c) correspond to the M1-, M2-, and M2Sum energy spectrum, respectively. The ^{234}U contamination was constrained by ^{238}U in the $^{238}\text{U} - ^{230}\text{Th}$ sub-decay chain and the ^{226}Ra contamination was constrained by other peaks in the $^{226}\text{Ra} - ^{210}\text{Pb}$ sub-decay chain. The remaining structures corresponds to ^{230}Th and ^{210}Pb contaminations.

The remaining alpha peaks in the M1 and M2 spectra and remaining peak in the M2Sum indicate ^{230}Th shallow crystal surface contamination. A corresponding deep crystal surface contamination with a characteristic depth of 100 nm was selected to be consistent with other simulations, but could not be verified by independent structures in the M2 spectrum. In the M1 spectrum, the amplitude of ^{230}Th Q-value peak indicates a bulk crystal contamination. Only deep ^{210}Pb surface contaminations in the crystals (1 μm and 10 μm) can describe the overall slope in the M2 spectrum and only deep ^{210}Pb surface contaminations (100 nm, 1 μm , and 10 μm) in the copper tower structures can describe the overall slope in the M1 spectrum.

The simulated peak positions and resolutions are generally representative the data. In most cases, there is a discrepancy between the data and simulation in the region between the alpha peak and Q-value peak in the M1 spectrum and in the low-energy tail structure in the M2Sum spectrum. Regarding ^{210}Po , its peak regions are mostly excluded from this analysis since the data exhibits more M2 events compared to M1 events than possible with the available simulations. These discrepancies will be discussed in Section 4.6. Table 4.6 and Table 4.7 include a list of the surface contaminations and bulk contaminations selected to include in the model, respectively.

4.5 Background fit of the alpha energy region

Using BAT, we performed a simultaneous binned fit of the M1 and M2 energy spectra in the alpha energy region, excluding the ^{210}Po peak regions. We excluded the ^{210}Po peak regions because the relative number of M1 and M2 peak events in the data could not be reproduced by our model. This omission is discussed further in Section 4.6. We also excluded the energy region above ~ 6 MeV since there are typically fewer events associated with these energies, making our pulse shape analysis less effective.

We fit the data spectra corresponding to background events from DS3606 – DS3615. Only events that passed the base cuts, coincidence, and PCA cuts discussed in Chapter 3 are included. For the coincidence cut, we required M2 events occur within 30 ms of each other, have energies greater than 70 keV, and occur within 150 mm from each other, based

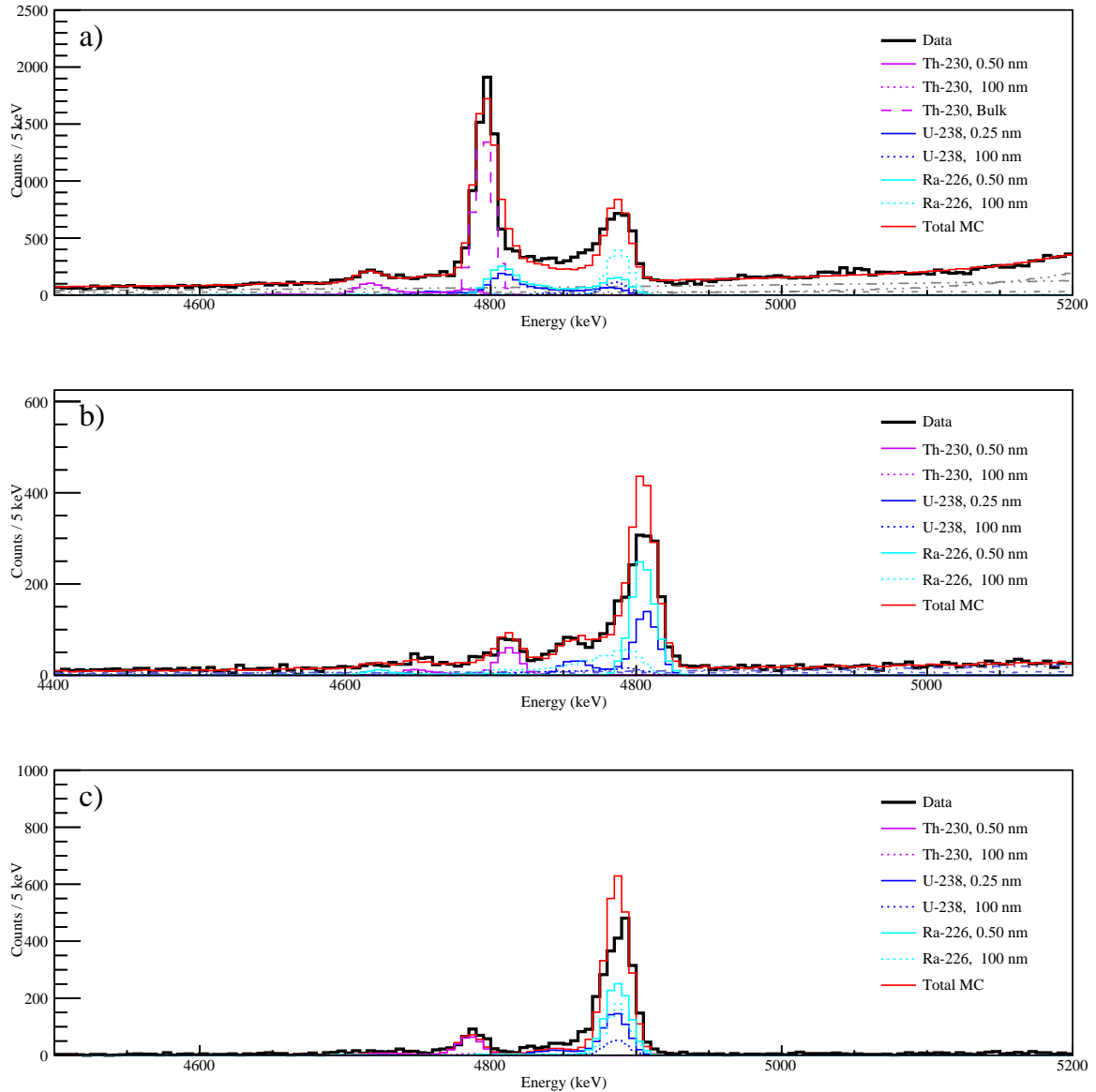


Figure 4.20: ^{230}Th and ^{210}Pb contaminations. a) corresponds to the M1 spectrum, b) corresponds to the M2 spectrum, and c) corresponds to the M2Sum spectrum.

on the center coordinates of each crystal.

Corresponding cuts are applied in the simulations used in the model. In *g4cuore*, one of the dataset numbers is assigned to each simulated event. The events are distributed among the datasets such that the relative number of events corresponds to the relative exposures of the datasets. This assignment is used to implement and reflect any dataset-dependent cuts.

In order to simulate the pulse shape analysis, `g4cuore` assigns a boolean flag based on the dataset-dependent PCA efficiency, then removes events with false flags to represent the PCA cut. Since the base cut removes any event with multiple pulses in their 10-s time window, we implemented a 3-s pretrigger and 7-s post-trigger pile up cut in `g4cuore` to represent the same effect on the simulated events. For simulated coincidence events, we implemented the same energy threshold, coincidence time window, and distance cut as in the data.

For both the data and the simulations, we excluded events from dataset-channels that did not pass any of the analysis sequences. We also used a cut on the crystal geometry that requires M1 events to correspond to energies deposited in the inner crystals. For M2 events, only the first chronological event in the pair is required to correspond to energy deposited in the inner crystals.

4.5.1 Fit results

In our fit, we modeled the data as a linear combination of the simulated energy spectra discussed in Section 4.4.1 using their normalization factors as our fit parameters. The fit result for the M1 and M2 energy spectra are shown in Figure 4.21 and Figure 4.22, respectively. The lower plot in each figure shows the ratio of events in data to reconstructed events from the fit. Data points outside the colored bands indicate which energy regions are poorly reconstructed. The poor reconstructions in these regions are discussed in Section 4.6.

4.5.2 Activities

The activity is given by the ratio of the background contamination's count rate and its detection efficiency. We used the fit to determine the contribution of each background contamination and obtained their activities with

$$A_i = \frac{N_i^{fit} N_i^{MC}}{T}, \quad (4.5)$$

where i is used to index the background contamination, N_i^{fit} is the normalization factor from the fit, which also accounts for the efficiency, N_i^{MC} is the number of simulated decay chains,

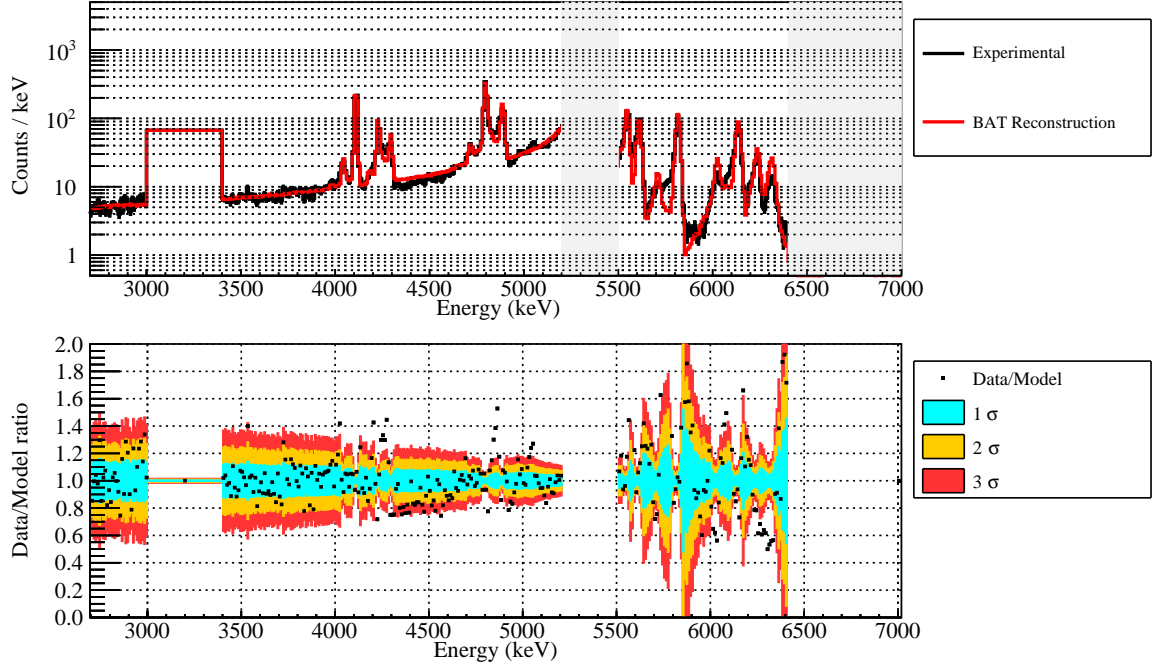


Figure 4.21: Top: M1 reconstruction compared with data. Bottom: Ratio of data events and reconstructed events by bin. Gaps in data points correspond to energy regions omitted from the fit.

and T is the livetime corresponding to the experimental data used in the fit. Table 4.6 and Table 4.7 list the activities per unit surface area and mass, respectively; the surface areas and masses of the source locations are listed in Table 4.4.

In order to check the stability of the fit result, we performed alternative fits on the data while varying individual model parameters. We evaluated the systematic uncertainties on the activities using the differences between the fit results. We investigated the systematic uncertainties related to the choice of datasets, crystal geometry, and energy binning. Individual datasets did not provide adequate statistics for the fit, so the datasets were split based on dataset number, between even/odd and first/second half. We also performed the fit on the excluded datasets (DS3601 – DS3605). For the crystal geometry, only the inner crystals were considered. We split the geometry based on channel number (even/odd and last digit), floor number (even/odd and first/second half), and tower number (even/odd and first/second half). For the binning, we used 15 keV, 20 keV, and 25 keV bins in the alter-

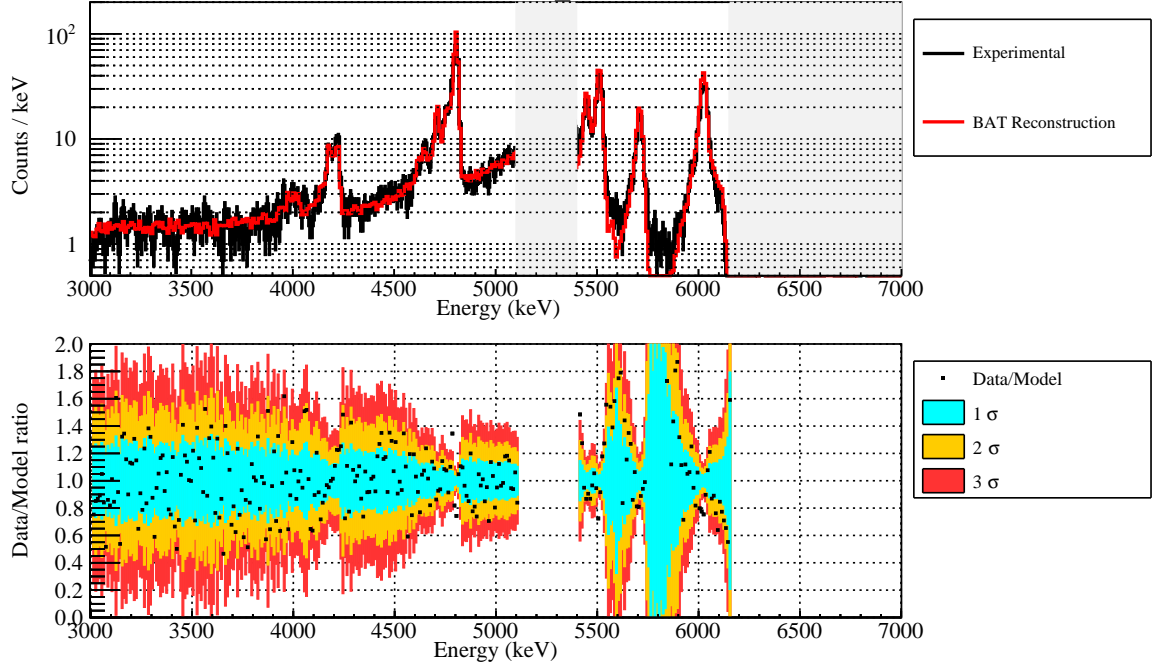


Figure 4.22: Top: M2 reconstruction compared with data. Bottom: Ratio of data events and reconstructed events by bin. Gaps in data points correspond to energy regions omitted from the fit.

native fits, but did not change the binning for the platinum peak. The resulting systematic uncertainties are listed in the last column of Table 4.6 and Table 4.7.

4.5.3 Comparison with the CUORE-0 background model

The CUORE-0 experiment was a prototype for CUORE that searched for $0\nu\beta\beta$ decay in ^{130}Te from March 2013 to March 2015. While the CUORE infrastructure was still in progress, the CUORE-0 detector, the first CUORE-like tower assembled, operated in the cryostat of CUORE's predecessor experiment, Cuoricino, at LNGS. Although this detector environment introduced different background contaminations compared to CUORE, a rigorous background model was developed to disentangle and measure the contaminations of its various components. Because the CUORE-0 tower is identical to the 19 CUORE towers, we expect our background model to be compatible with the CUORE-0 background model. The results of the CUORE-0 background model for the surface and bulk contaminations in the

Table 4.6: Surface source activities.

Location	MC Decay Chain	Depth	Activity (Bq/cm ²)	Systematics (Bq/cm ²)
TeO ₂	²³² Th Only	0.50 nm	$(3.01 \pm 0.25) \times 10^{-10}$	$\pm 4.39 \times 10^{-11}$
	²³² Th Only	100 nm	$(1.15 \pm 0.32) \times 10^{-10}$	$\pm 1.05 \times 10^{-10}$
	²²⁸ Ra – ²⁰⁸ Pb	0.50 nm	$(1.07 \pm 0.03) \times 10^{-9}$	$\pm 6.51 \times 10^{-11}$
	²²⁸ Ra – ²⁰⁸ Pb	100 nm	$(7.47 \pm 0.33) \times 10^{-10}$	$\pm 1.96 \times 10^{-10}$
	²³⁸ U – ²³⁰ Th	0.25 nm	$(1.53 \pm 0.04) \times 10^{-9}$	$\pm 1.48 \times 10^{-10}$
	²³⁸ U – ²³⁰ Th	100 nm	$(4.90 \pm 0.29) \times 10^{-10}$	$\pm 7.09 \times 10^{-11}$
	²³⁰ Th Only	0.50 nm	$(7.12 \pm 0.44) \times 10^{-10}$	$\pm 1.29 \times 10^{-10}$
	²³⁰ Th Only	100 nm	$< 4.0 \times 10^{-10}$	$< 2.0 \times 10^{-10}$
	²²⁶ Ra – ²¹⁰ Pb	0.5 nm	$(2.24 \pm 0.04) \times 10^{-9}$	$\pm 1.59 \times 10^{-10}$
	²²⁶ Ra – ²¹⁰ Pb	100 nm	$(1.37 \pm 0.03) \times 10^{-9}$	$\pm 7.07 \times 10^{-11}$
	²¹⁰ Pb – ²⁰⁶ Pb	1 μ m	$(6.47 \pm 0.27) \times 10^{-9}$	$\pm 1.21 \times 10^{-9}$
	²¹⁰ Pb – ²⁰⁶ Pb	10 μ m	$(9.54 \pm 0.32) \times 10^{-9}$	$\pm 5.67 \times 10^{-10}$
Cu tower	²²⁸ Ra – ²⁰⁸ Pb	100 nm	$(2.76 \pm 0.15) \times 10^{-9}$	$\pm 5.02 \times 10^{-10}$
	²²⁶ Ra – ²¹⁰ Pb	100 nm	$(2.48 \pm 0.15) \times 10^{-9}$	$\pm 5.39 \times 10^{-10}$
	²¹⁰ Pb – ²⁰⁶ Pb	100 nm	$(4.07 \pm 0.17) \times 10^{-7}$	$\pm 8.41 \times 10^{-8}$
	²¹⁰ Pb – ²⁰⁶ Pb	1 μ m	$(3.46 \pm 0.11) \times 10^{-7}$	$\pm 1.01 \times 10^{-7}$
	²¹⁰ Pb – ²⁰⁶ Pb	10 μ m	$(3.66 \pm 0.14) \times 10^{-7}$	$\pm 7.92 \times 10^{-8}$

tower components are summarized in Table 4.8 and Table 4.9, respectively.

4.5.4 Background index

The $0\nu\beta\beta$ decay region of interest (ROI) for CUORE corresponds to the 2490 keV – 2575 keV range in the M1 energy spectrum. This energy range contains $Q_{\beta\beta}$ for ¹³⁰Te and its surrounding energy region, which allows us to estimate the background. The ⁶⁰Co sum peak is also included in the ROI only because of its proximity to $Q_{\beta\beta}$. Although we do not fit the ROI

Table 4.7: Bulk source activities.

Location	Source	Activity (Bq/kg)	Systematics (Bq/kg)
TeO ₂	¹⁹⁰ Pt Only	$(1.99 \pm 0.01) \times 10^{-6}$	$\pm 8.42 \times 10^{-8}$
	²³² Th Only	$(3.33 \pm 0.06) \times 10^{-7}$	$\pm 7.15 \times 10^{-8}$
	²²⁸ Ra – ²⁰⁸ Pb	$(1.65 \pm 0.04) \times 10^{-7}$	$\pm 4.21 \times 10^{-8}$
	²³⁰ Th Only	$(3.80 \pm 0.08) \times 10^{-7}$	$\pm 9.44 \times 10^{-8}$

Table 4.8: Surface contaminations in the TeO₂ crystals and Cu support structure based on CUORE-0 background model [38].

Location	Source	Depth (μm)	Activity (Bq/cm ²)	Systematics (Bq/cm ²)
TeO ₂	²³² Th only	0.01	$(3.0 \pm 1.0) \times 10^{-10}$	
	²²⁸ Ra – ²⁰⁸ Pb	0.01	$(2.32 \pm 0.12) \times 10^{-9}$	$2.1 \times 10^{-9} - 2.7 \times 10^{-9}$
	²³⁸ U – ²³⁰ Th	0.01	$(2.07 \pm 0.11) \times 10^{-9}$	$1.8 \times 10^{-9} - 2.2 \times 10^{-9}$
	²³⁰ Th only	0.01	$(1.15 \pm 0.14) \times 10^{-9}$	
	²²⁶ Ra – ²¹⁰ Pb	0.01	$(3.14 \pm 0.10) \times 10^{-9}$	$2.9 \times 10^{-9} - 3.5 \times 10^{-9}$
	²¹⁰ Pb	0.001	$(6.02 \pm 0.08) \times 10^{-8}$	$4.8 \times 10^{-8} - 7.2 \times 10^{-8}$
	²¹⁰ Pb	1	$(8.6 \pm 0.8) \times 10^{-9}$	$7.2 \times 10^{-9} - 1.1 \times 10^{-8}$
	²¹⁰ Pb	10	$< 2.7 \times 10^{-9}$	$< 4.9 \times 10^{-9}$
	²³² Th	10	$(7.8 \pm 1.4) \times 10^{-10}$	
	²³⁸ U	10	$< 3.3 \times 10^{-11}$	$< 1.2 \times 10^{-10}$
Cu tower	²¹⁰ Pb	0.01	$(2.9 \pm 0.4) \times 10^{-8}$	$2.1 \times 10^{-8} - 4.3 \times 10^{-8}$
	²¹⁰ Pb	0.1	$(4.3 \pm 0.5) \times 10^{-8}$	$3.1 \times 10^{-8} - 5.1 \times 10^{-8}$
	²¹⁰ Pb	10	$< 1.9 \times 10^{-8}$	$< 3.9 \times 10^{-8}$
	²³² Th	10	$(5.0 \pm 1.7) \times 10^{-9}$	$< 1.0 \times 10^{-8}$
	²³⁸ U	10	$(1.39 \pm 0.16) \times 10^{-8}$	$8.4 \times 10^{-9} - 1.6 \times 10^{-8}$

Table 4.9: Bulk contaminations in the TeO₂ crystals based on CUORE-0 background model [38].

Location	Source	Activity (Bq/kg)	Systematics (Bq/kg)
TeO ₂	¹⁹⁰ Pt	$(2.00 \pm 0.05) \times 10^{-6}$	$1.6 \times 10^{-6} - 2.3 \times 10^{-6}$
	²¹⁰ Po	$(2.39 \pm 0.11) \times 10^{-6}$	
	²¹⁰ Pb	$(1.37 \pm 0.19) \times 10^{-6}$	$5.4 \times 10^{-7} - 2.2 \times 10^{-6}$
	²³² Th only	$(7 \pm 3) \times 10^{-8}$	$< 1.2 \times 10^{-7}$
	²²⁸ Ra – ²⁰⁸ Pb	$< 3.5 \times 10^{-8}$	$< 7.5 \times 10^{-8}$
	²³⁸ U – ²³⁰ Th	$< 7.5 \times 10^{-9}$	$< 3.6 \times 10^{-8}$
	²³⁰ Th only	$(2.8 \pm 0.3) \times 10^{-7}$	
	²²⁶ Ra – ²¹⁰ Pb	$< 7.0 \times 10^{-9}$	$< 2.2 \times 10^{-8}$

in this analysis, we compare our reconstruction of the alpha background in the ROI to the data in Figure 4.23. This comparison confirms that the main contribution to the background in the ROI is from surface contamination of the copper support structure, specifically deep ²¹⁰Pb contamination. Figure 4.24 shows the background in the CUPID ROI is dominated by the same contaminations. Although these alpha backgrounds will be removed through particle identification in CUPID, associated betas and gammas from the decay chain will continue to contribute to the background. By reviewing the cleaning procedures and handling, including packaging and storage, of the copper parts near the detector, the background index in CUPID may further be reduced.

4.6 Discussion

While developing our background model, we found that we could not use the same detector response across all simulations. Between surface and bulk contamination simulations, different energy resolution functions and quenching factors were required to reproduce the peak widths and positions observed in the data. We also found that different quenching

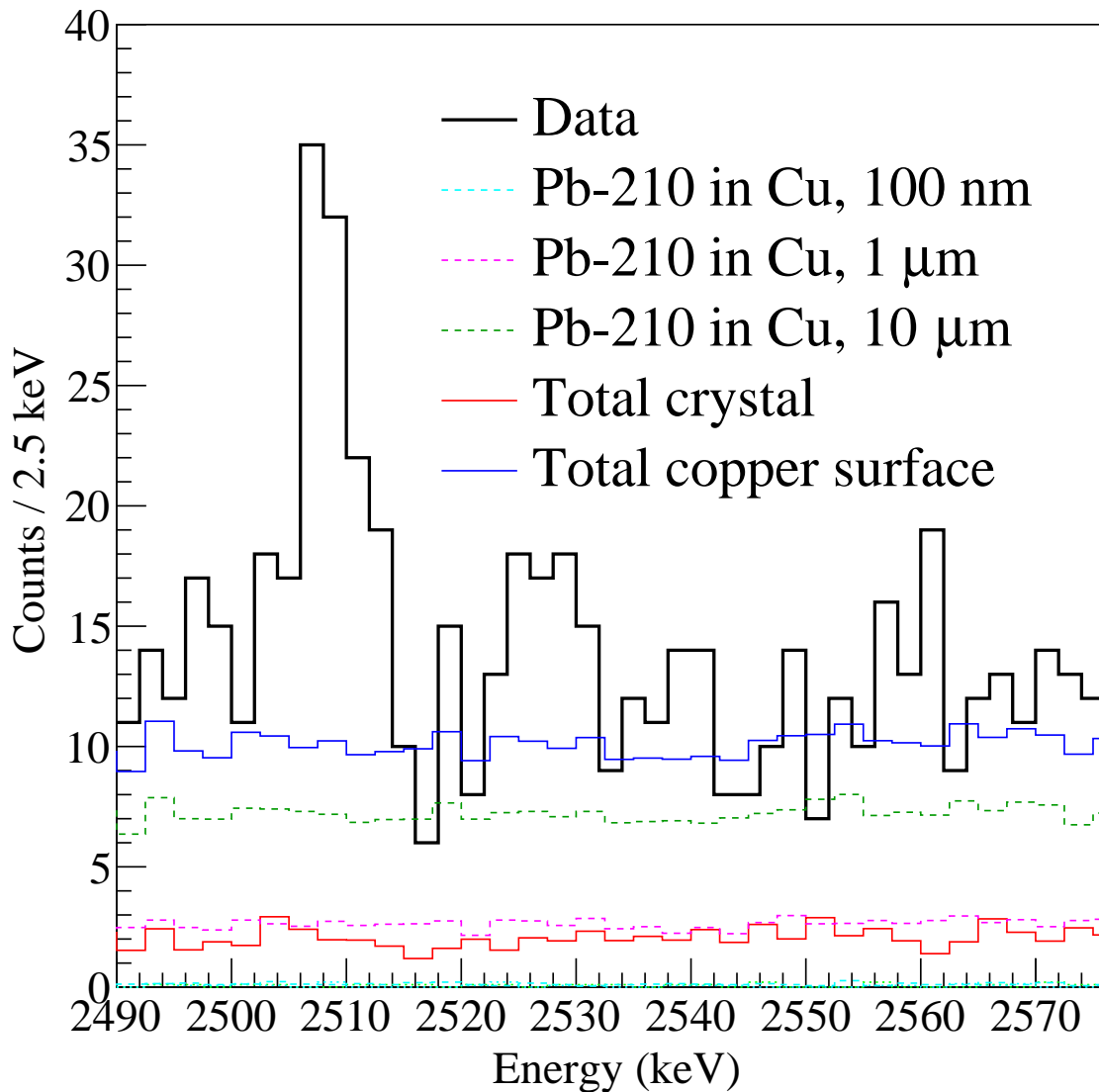


Figure 4.23: Background contribution from all simulated alpha contaminations in the ROI. Only prominent sources are listed in the legend.

factors were required for different particle types and background sources. Experimental measurements should be performed to understand and confirm the detector energy response dependence on the surface contamination depth. Measurements of the alpha particle quenching in TeO_2 bolometers already exist, but introduce the alpha particle dopants during crystal growth [39]. As a first step, we propose measuring the TeO_2 bolometer energy response to a

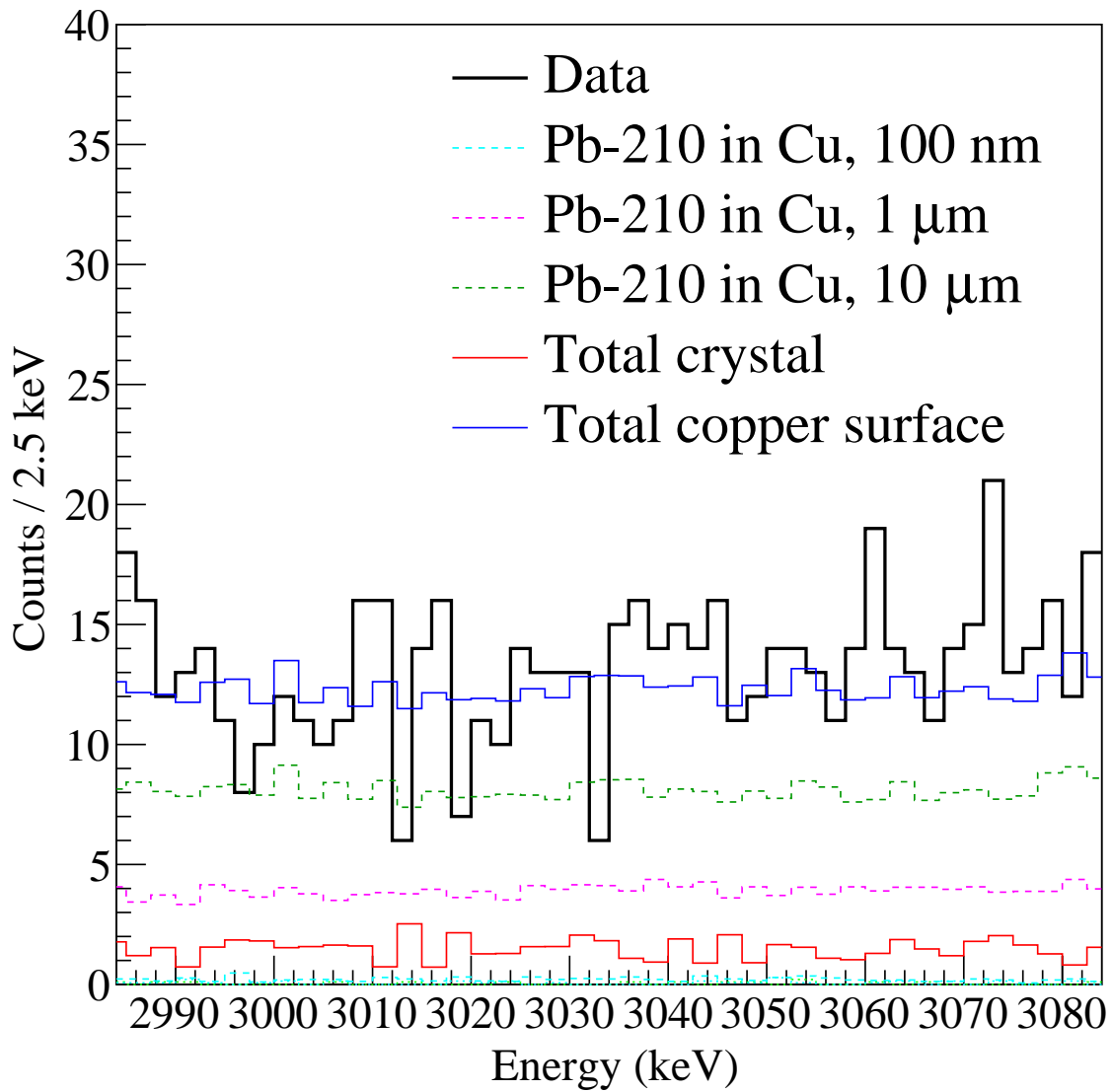


Figure 4.24: Background contribution from all simulated alpha contaminations in the CUPID ROI. Only prominent sources are listed in the legend.

thin layer of alpha particle emitter applied to its surface to study the surface effects of the detector.

Our fit results highlight the structures we are not yet able to reproduce with our simulations. In our simulated M1 spectrum, the valley regions between the alpha and Q-value peaks are consistently underestimated and in our simulated M2Sum spectrum, the low-energy tails

of the M2Sum peaks are also consistently underestimated. Both structures indicate shallow crystal surface contamination where most of the energy of the decay is detected in one or two crystals. The nature of the contamination indicates these discrepancies may be related to the contamination depth dependence of the detector energy response. Running additional coincidence analysis sequences with different low-energy thresholds and studying how the shape of the structures change may help probe the surface effects of the detector.

Regarding our exclusion of the ^{210}Po peak regions, ^{222}Rn is a progenitor of ^{210}Po , so a possible contamination to consider including in our simulations in the future is ^{222}Rn in the vacuum. Currently, since our simulations do not include ^{210}Pb shallow crystal surface contaminations to help constrain the ^{210}Pb copper surface contaminations, the unidentified structures around 5 MeV have caused the low-energy tail of the ^{210}Po alpha peak in the M1 spectrum to be overestimated ~ 4.5 MeV.

CHAPTER 5

Conclusions

We studied the M1 and M2 background spectra of CUORE in the energy region above 2.7 MeV to investigate the alpha background sources in our detector. We have identified ^{238}U , ^{232}Th , and ^{190}Pt as background sources contributing to this alpha energy region using their characteristic decay signatures. Multiplicity information, based on the number of CUORE crystals that detect energy depositions within a given space-time window, was used to distinguish surface and bulk alpha source contaminations. We used a Geant4 model of CUORE to simulate the energy spectra of the identified background sources at various characteristic depths in the crystal and tower support structure. The shapes of the simulated energy spectra were compared to the structures in the data to constrain the contamination depths we selected to include in our background model. Extrapolating our reconstruction of the alpha energy region to the ROI indicate that degraded alpha particles from copper surface contamination of ^{210}Pb are driving the background index. Initial material purity, cleaning, packaging, handling, and storage procedures of the copper parts are important to control contamination with ^{210}Pb or ^{222}Rn . Optimizing these procedures respect to CUPID will be important to avoid beta and gamma backgrounds associated with these contaminations.

Appendix A

Tables

Table A.1: Dataset exposures after analysis cuts.

Dataset(s)	Inner Crystals (kg·yr)	Lateral Crystals (kg·yr)	Top Crystals (kg·yr)	Bottom Crystals (kg·yr)	All Crystals (kg·yr)
3601	21.19	11.26	1.32	1.81	37.17
3602	26.47	15.46	2.22	2.32	48.77
3603	39.85	23.09	3.18	3.42	73.11
3604	37.58	21.68	3.00	3.44	68.86
3605	10.56	5.91	0.86	0.96	19.12
3606	31.43	17.67	2.62	2.93	57.21
3607	38.55	21.69	3.31	3.53	70.30
3608	42.26	24.56	3.56	3.89	77.96
3609	41.24	23.35	3.45	3.85	75.50
3610	45.67	25.58	3.74	4.10	82.64
3611	46.36	25.95	3.54	4.16	83.64
3612	45.65	26.76	3.55	4.18	83.95
3613	48.88	28.17	3.93	4.51	89.61
3614	40.64	23.21	3.30	3.77	74.53
3615	52.69	29.71	4.29	4.90	96.08
3601 – 3615	569.02	324.07	45.87	51.76	1038.43
3606 – 3615	433.37	246.66	35.28	39.82	791.41

ACRONYMS

AC Anti-coincidence.

BAT Bayesian Analysis Toolkit.

CUORE Cryogenic Underground Observatory for Rare Events.

CUPID CUORE Upgrade with Particle IDentification.

DAQ Data Acquisition.

DCS Detector Calibration System.

DT Derivative Trigger.

DU Dilution Unit.

EDCS External Detector Calibration System.

ETP Electrolytic Tough Pitch.

FCS Fast cooling system.

FWHM Full Width Half Maximum.

IVC Inner Vacuum Chamber.

LNGS Gran Sasso National Laboratory.

LPS Linear Power Supply.

MC Monte Carlo.

MCMC Markov Chain Monte Carlo.

NTD Ge Neutron Transmutation Doped Germanium.

OF Optimum filter.

OT Optimum Trigger.

OVC Outer Vacuum Chamber.

PDF Probability Density Function.

PE Polyethylene.

PT Pulse Tube.

PTFE Polytetrafluoroethylene.

TECM Tumbling, Electropolishing, Chemical etching, and Magnetron-plasma etching.

REFERENCES

- [1] PDG. *14. Neutrino Masses, Mixing, and Oscillations* <https://pdg.lbl.gov/2020/reviews/rpp2020-rev-neutrino-mixing.pdf>.
- [2] Aghanim, N. *et al.* Planck 2018 results - VI. Cosmological parameters. *Astronomy Astrophysics* **641**, 67 (2020).
- [3] King, S. *et al.* Neutrino Mass and Mixing with Discrete Symmetry. *Rept. Prog. Phys.* **76**, 056201 (2013).
- [4] Goeppert-Mayer, M. Double Beta-Disintegration. *Phys. Rev.* **48**, 512–516 (1935).
- [5] PDG. *Double- β Decay* <https://pdg.lbl.gov/2018/listings/rpp2018-list-double-beta-decay.pdf>.
- [6] Furry, W. H. On Transition Probabilities in Double Beta-Disintegration. *Physical Review*. **56**, 1184–1193 (1939).
- [7] Gando, A. *et al.* Search for Majorana Neutrinos Near the Inverted Mass Hierarchy Region with KamLAND-Zen. *Phys. Rev. Lett.* **117**, 082503 (2016).
- [8] Agostini, M. *et al.* Final Results of GERDA on the Search for Neutrinoless Double- β Decay. *Phys. Rev. Lett.* **125**, 252502 (2020).
- [9] Redshaw, M. *et al.* Masses of ^{130}Te and ^{130}Xe and *Double- β -Decay Q Value of ^{130}Te* . *Phys. Rev. Lett.* **102**, 212502 (2009).
- [10] Fehr, M. *et al.* Application of MC-ICPMS to the precise determination of tellurium isotope compositions in chondrites, iron meteorites and sulfides. *International Journal of Mass Spectrometry* **232**, 83–94 (2004).
- [11] Adams, D. *et al.* High sensitivity neutrinoless double-beta decay search with one tonne-year of CUORE data. (2021).
- [12] Alduino, C. *et al.* CUORE-0 detector: design, construction and operation. *Journal of Instrumentation* **11**, P07009 (2016).

- [13] Ambrosio, M. *et al.* Vertical muon intensity measured with MACRO at the Gran Sasso laboratory. *Phys. Rev. D* **52**, 3793 (1995).
- [14] Arneodo, F. *et al.* Neutron background measurements in the Hall C of the Gran Sasso Laboratory. *Nuovo Cimento A* **112**, 819 (1999).
- [15] Kittel, C. *Introduction to Solid State Physics*. (John Wiley and Sons, 2005).
- [16] Cryomech. *Gifford-McMahon (AL600) Cryocooler* <https://www.cryomech.com/products/al600/>.
- [17] Cryomech. *Pulse Tube (PT415) Cryocooler* <https://www.cryomech.com/products/pt415/>.
- [18] Cryogenics, L. *Cryogen-free* <https://leiden-cryogenics.com/products/cryogen-free>.
- [19] Alduino, C. *et al.* The CUORE cryostat: An infrastructure for rare event searches at millikelvin temperatures. *Cryogenics* **102**, 9–21 (2019).
- [20] Capelli, S. Background analysis of the experiments MiDBD, CUORICINO and CUORE. *PhD thesis*, Università degli Studi di Milano (2005).
- [21] Arnaboldi, C. *et al.* Production of high purity TeO₂ single crystals for the study of neutrinoless double beta decay. *J. Cryst. Growth* **312**, 2999–3008 (2010).
- [22] Aurubis. *Aurubis SHAPES* <https://www.aurubis.com/products/page-shapes>.
- [23] Alduino, C. *et al.* The projected background for the CUORE experiment. *Journal of Instrumentation* **77**, 543 (2017).
- [24] Alessandria, F. *et al.* Validation of techniques to mitigate copper surface contamination in CUORE. *Astroparticle Physics*. **45**, 13–22 (2013).
- [25] Alessandrello, A. *et al.* Measurements of internal radioactive contamination in samples of Roman lead to be used in experiments on rare events. *Nuclear Instruments and Methods in Physics Research B* **142**, 163–172 (1998).
- [26] Alfonso, K. *et al.* An automated system to define the optimal operating settings of cryogenic calorimeters. *Nucl. Instrum. Methods Phys. Res. A*. **1008**, 165451 (2021).

- [27] Domizio, S. D. *et al.* A data acquisition and control system for large mass bolometer arrays. *Journal of Instrumentation* **13**, P12003 (2018).
- [28] Domizio, S. D. *et al.* Lowering the energy threshold of large mass bolometric detectors. *Journal of Instrumentation* **6**, P02007 (2011).
- [29] Gatti, E. & Manfredi, P. Processing the Signals from Solid-State Detectors in Elementary-Particle Physics. *La Rivista del Nuovo Cimento* **9**, 1 (1986).
- [30] Martinez, M. Stabilization without heater. CUORE Document ID: cuore-doc-26-v1. (2014).
- [31] Jolliffe, I. T. *et al.* Principal component analysis: a review and recent developments. *Phil. Trans. R. Soc. A* **76**, 056201 (2016).
- [32] Huang, R. Searching for $0\nu\beta\beta$ Decay with CUORE and CUPID. *PhD thesis*, University of California, Berkeley (2021).
- [33] Cushman, J. *et al.* The detector calibration system for the CUORE cryogenic bolometer array. *Nuclear Instruments and Methods A* **844**, 32–44 (2017).
- [34] Center, N. N. D. *NuDat 3.0*. <https://www.nndc.bnl.gov/nudat3/>.
- [35] Association, W. N. *Naturally-Occurring Radioactive Materials (NORM)*. <https://world-nuclear.org/information-library/safety-and-security/radiation-and-health/naturally-occurring-radioactive-materials-norm.aspx>.
- [36] Agostinelli, S. *et al.* GEANT4: A Simulation toolkit. *Nucl. Instrum. Meth. A* **506**, 250–303 (2003).
- [37] Biassoni, M. *et al.* CUORE Internal Note 114D: CUORE-0 Background Reconstruction. (2016).
- [38] Alduino, C. *et al.* Measurement of the Two-Neutrino Double Beta Decay Half-life of Te-130 with the CUORE-0 Experiment. *European Physical Journal C*. **77**, 13 (2017).
- [39] Bellini, F. *et al.* Response of a TeO₂ bolometer to α particles. *Journal of Instrumentation* **11**, P12005 (2020).